Detection and analysis of oceanic motion using Pressure Inverted Echo Sounders (PIES)

Von der Fakultät für Mathematik und Naturwissenschaften der Carl von Ossietzky Universität Oldenburg zur Erlangung des Grades und Titels einer

Doktorin der Naturwissenschaften (Dr. rer. nat.)

angenommene Dissertation.

Madlen Gebler

geboren am 10.08.1985 in Gera

Declaration of Authorship

I certify that the work presented here is, to the best of my knowledge and belief, original and the result of my own investigations, except as acknowledged, and has not been submitted, either in part or whole, for a degree at this or any other University.

Madler Gebler

Bremen, November 2012

Contents

Abstract

Since their development in the 1970s Pressure Inverted Echo Sounders (PIES) have been used to address numerous oceanographic questions. PIES measure ocean bottom pressure and acoustic round trip travel time which is a vertically integrated function of density. Since 2003 the Alfred Wegener Institute (AWI) operates an array of six PIES along the Good Hope line south of Africa. The Good Hope line is a ground track of satellite altimeter Jason 1 and 2 across the Antarctic Circumpolar Current (ACC) and the PIES were deployed at cross over points of the ascending and descending track.

The first part of this thesis uses the Gravest Empirical Mode (GEM) method to derive Sea Surface Height (SSH) anomalies and baroclinic ACC transport. The derived total SSH anomalies were compared to two different satellite altimetry product. The AVISO product is a smoothed and gridded combination of data from different satellites while the openADB database provides the along track measured data without any smoothing or gridding. The correlation of the total (broclinic+barotropic) SSH anomaly with satellite altimetry results higher correlation coefficients for the gridded AVISO product (0.33-0.92) compared to the along track openADB (0.24-0.92) product. Dividing the total SSH anomaly into baroclinic and barotropic part results a contribution of the barotropic component in the order of 30-60%. The highest barotropic components are found inbetween the fronts.

Calculating the baroclinic ACC transports results a mean of 147±2.4 Sv for the deployment period 2007-2008 and 142±1.9 Sv respectively for the period 2008-2010. Both the mean and standard deviation compare well with previous observations and model results. In conclusion the PIES derived SSH anomaly showed a significant contribution of the barotropic component to the total variability and a better correlation with the (smoother) gridded satellite altimetry product. The derived baroclinic ACC transport is in close agreement with previous measurements. It can be derived with higher temporal resolution than in previous studies.

The second part of this thesis investigates how insitu ocean bottom pressure (OBP) can improve a least square inversion of GPS (Global Positioning System) data, GRACE (Gravity Recovery and Climate Experiment) data and modeled OBP used to derive global ocean mass changes. The inversion combines the information provided the different datasets and fits a mathematical model through it. The difference between the model and the data is minimized in a least square sense. The inversion with in-situ OBP locally improves the correlation with the Bottom Pressure recorders (BPRs) but does only slightly influence global parameters like the global mean ocean mass or the geocenter motion. In conclusion there are to less BPRs which are furthermore irregular distributed in time and space to significantly improve the inversion.

Zusammenfassung

Seit ihrer Entwicklung in den 70er Jahren wurden Pressure Inverted Echo Sounder (PIES) genutzt, um zahlreiche ozeanographische Fragestellungen zu bearbeiten. PIES messen den Ozeanbodendruck (OBP) und die Schalllaufzeit. Die Schalllaufzeit ist eine von der Dichte abhängige, über die gesamte Wassersäule integrierte Größe. Seit 2003 unterhält das Alfred Wegener Institut ein Array von sechs PIES entlang der Good Hope Linie südlich von Afrika. Die Good Hope Linie entspricht einer quere über den Antarktischen Zirkumpolarstrom (ACC) verlaufenden Bodenspur der Satelliten-Altimeter Jason 1 und 2. Die PIES wurden ausserdem an Kreuzungspunkten der aufsteigenden und absteigenden Bodenspuren ausgelegt.

Der erste Teil der vorliegenden Dissertation verwendet die Gravest Empirical Mode (GEM) Methode um Anomalien der Meereshöhe (SSH) und die baroklinen ACC Transporte zu bestimmen. Die Anomalien der Meereshöhe wurden mit zwei unterschiedliche Satelliten-Altimetrie-Produkten verglichen. Das AVISO-Produkt ist eine Kombination aus Daten verschieden Satellitenmissionen, die geglättet und auf ein regelmäßiges Gitter interpoliert wurden, während das openADB Produkt, die entlang der Bodenspur gemessen Daten, ohne irgendwelche Glättung oder Interpolation enthält. Die Korrelation der SSH Anomalie mit Satelliten Produkten zeigt höhere Korrelationskoeffizienten unter Verwendung des AVISO Produkts (0.33-0.92) als unter Verwendung der openADB Daten (0.24-0.92). Die Variabilität des SSH ist zwischen 30 und 60% barotroper Natur. Die höchsten brotropen Signale finden sich zwischen den Fronten.

Die Berechnung des baroklinen ACC Transportes ergibt im Mittel 147±2.4 Sv für die Auslegungsperiode 2007-2008 beziehungsweise 142±1.9 Sv für die Auslegungsperiode 2008-2010. Sowohl der mittlere barokline ACC Transport als auch dessen Standardabweichung sind mit anderen Messungen vergleichbar. Zusammenfassend ließ sich mit Hilfe der PIES ein signifikanter barotroper SSH Anteil zwischen den Fronten und eine bessere Korrelation mit dem AVISO Satelliten-Altimetrie-Produkt nach-

weisen. Der berechnete barokline ACC Transport und dessen Variabilität stimmen mit früheren Beobachtungen überein. Durch die PIES wurde die zeitliche Auflösung der Transportzeitserie erheblich verbessert.

Im zweiten Teil wurde untersucht, wie gemessener Ozeanbodendruck (OBP) dazu beitragen könnte ein Kombination aus GPS (Global Positioning System) Daten, GRACE (Gravity Recovery and Climate Experiment) Daten und modelliertem OBP zur Bestimmung von globalen Ozeanmassenvariationen, global und lokal zu verbessern. Die Kombination der verschiedenen Datensätze erfolgt mit Hilfe einer gemeinsamen Inversion nach dem Prinzip der kleinsten Quadrate. Die Inversion passt ein mathematisches Modell an die Datensätze an wobei die Abweichung des Modells von den Daten im Sinne der kleinsten Quadrate minimiert wird. Die Einführung der gemessenen OBP-Daten in die Inversion führt lediglich zu einer lokalen Verbesserung der Korrelation mit den Bodendruckrecordern (BPRs). Sie hat keinen großen Einfluss auf globale Größen wie die mittlere globale Ozeanmasse oder die Geozentrums Bewegungen. Dies legt den Schluss nahe, dass auf Grund der geringen Anzahl und unregelmäßigen zeitlichen und räumlichen Verteilung eine signifikante Veränderung der Inversion nicht möglich war.

1 General Introduction

In the year 1969 Tom Rossby was the first who suggested that acoustic travel times can be used to determine changes in the thermocline (Rossby, 1969). The principle behind this is that the speed of sound in water depends on temperature, pressure and salinity. Hence the travel time of a signal transmitted from the sea floor to the surface and reflected back correlates with the ratio of cold to warm water which defines the thermocline depth.
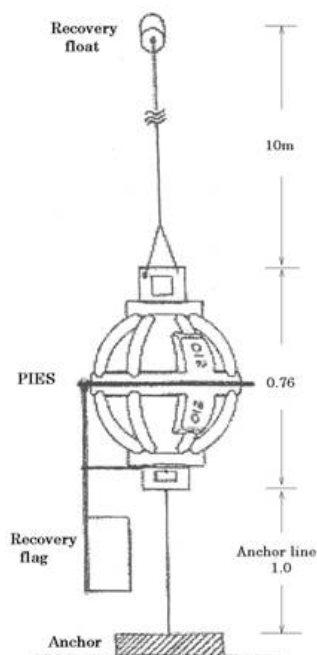
Figure 1.1: Scheme of a Pressure Inverted Echo Sounder [1]

Four years after Rossbys publication the first Inverted Echo Sounder (IES) were deployed during the Mid-Ocean Dynamics Experiment (MODE I) in the western

---

[1]http://www.jamstec.go.jp/iorgc/ocorp/ktsfg/data/02/kop0204/report/piesfig.htm

Sargasso Sea between Bermuda and Florida. A 10 kHz Impulse was used to measure the acoustic round trip travel time. The batteries of the first IES had a life time of 2 months. The aim of this survey was to monitor the changes in the thermocline depth.
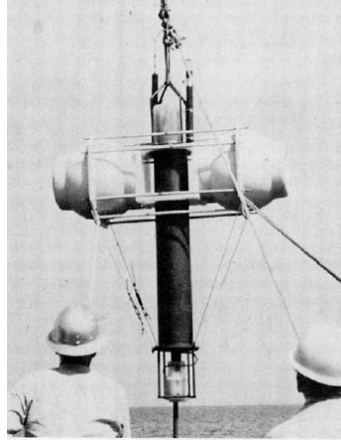
Figure 1.2: Deployment of an old Inverted Echo Sounder. (Watts and Rossby, 1977)

The first IES looked like tubes (Fig. 1.2) with a length of 1.5 m. During the mid-1970s IES were put in glass spheres which is the typical appearance until today (see Fig. 1.1 and Fig. 1.3). 1981 the first Pressure Inverted Echo Sounder (PIES), an IES with an additional bottom pressure sensor, was deployed.

IES respectively PIES were used to investigate the temporal variability of temperature fields and dynamic height in many different regions. Watts and Rossby (1977) rescaled the acoustic travel time into dynamic height and identified internal waves of different amplitudes. Furthermore the abyssal current and pressure field of the Gulf Stream was explored using PIES. Watts et al. (2000a) found steep stationary troughs in the Gulf Stream spinning up deep-level eddies, topographic Rossby waves and ring-stream interaction. Another area of intensive investigation using PIES is the Kuroshio Extension region. Book et al. (2001) analyzed a two year long time series of IES data and current meter moorings. They found small offshore meanders of the Kuroshio stream with a four month periodicity. Before the appearearance of a meander occurs observed low Kuroshio volume transport, followed by high transport after the meander has passed by. In the year 2004 43 CPIES (PIES with current meter) and 3 PIES were deployed as part of the Kuroshio Extension System Study
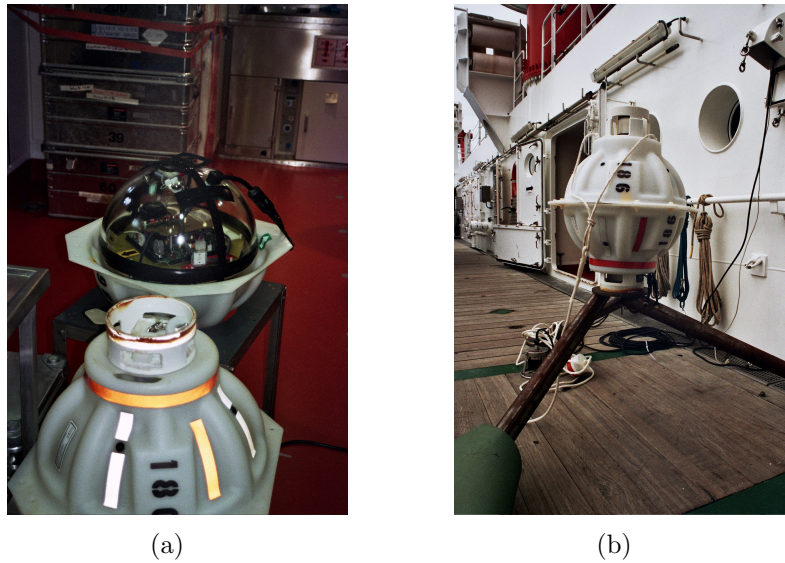
Figure 1.3: (a) Open PIES where the glass sphere with electronic can be seen. (b) PIES on deck of RV Maria S. Merian ready for deployment.

(KESS). KESS aimed to produce mesoscale-resolving four dimensional fields of the circulation, the temperature structure, the specific volume anomaly and the velocity.

Moreover IES were deployed south of Australia to investigate the Antarctic Circumpolar Current (ACC). To this end Watts et al. (2000b) developed a method called Gravest Empirical Mode (GEM) (detailed explanation see section 2.2.1) using a tight empirical relationship between the acoustic travel time and temperature and salinity profiles. In a depth range between 150-3000 dbar the GEM captures 96% of the temperature variability.

Chapter 2 of this thesis uses the GEM method from Watts et al. (2000b) to investigate the ACC south of Africa. Key aspects of the study are the creation of a GEM look up table for this region and it's validation. Furthermore the sea surface height (SSH) anomaly and its composition of baroclinic and barotropic parts is investigated. Another key aspect is the ACC transport and its variability. A possible teleconnection of the properties derived from PIES and the southern annular mode (SAM) is analyzed. Furthermore a model comparison is performed between the Southern Ocean State Estimate (SOSE) and the PIES.

Chapter 3 of this thesis represents part of the project **JIGOG** (Surface mass redistribution from **J**oint **I**nversion of **G**PS site displacements, **Ocean** bottom pressure (OBP) models, and **G**RACE global Gravity models) which is part of the priority program "Mass transport and Mass distribution in the system Earth" supported by the German Research Foundation (DFG). The aim of this project is the improvement of a joint inversion of GRACE, GPS and OBP by including in-situ OBP from a global data base.

2 Monitoring the ACC with Pressure Inverted Echo Soundern (PIES)

2.1 Introduction to the ACC PIES-array

Since December 2002 the Alfred Wegener Institute for Polar and Marine Research operates various PIES along the Good Hope Line (Swart et al., 2008) south of Africa (Figure 2.1). The positions of the individual PIES are listed in Table 2.1. The array was deployed to monitor the variability of the Antarctic Circumpolar Current. The northern end of the array is located in the path of Agulhas rings, while the center of the array is in the vicinity of the South Atlantic Drift (Strammma and Peterson, 1990). The southern end is placed in the Antarctic Circumpolar Current (ACC, see Figure 2.2).

Table 2.1: Position of the Pressure Inverted Echo Sounder (PIES)

PIES	Latitude	Longitude
ANT 3	-37.0980	12.7535
ANT 5	-41.1633	9.9215
ANT 7	-44.6618	7.0835
ANT 9	-47.6653	4.2515
ANT 11	-50.2577	1.4195
ANT 13	-52.5078	-1.4187
ANT 13_2	-53.5200	0.0133

Following Orsi et al. (1994) the ACC is confined between the Subtropic Front (STF) and the Southern ACC Front (SACCF). In the observation area the southern extent of the ACC is bounded by the Weddell Gyre. Klatt et al. (2005) observed
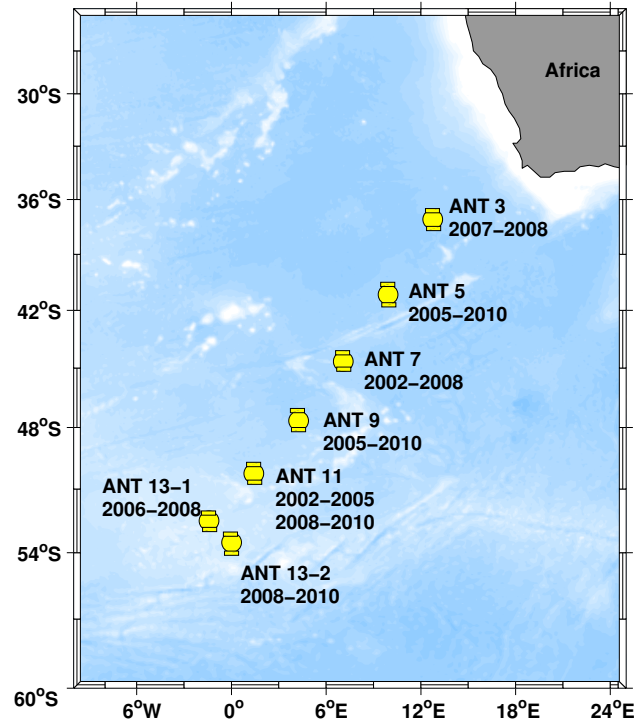
Figure 2.1: ACC array of PIES deployed by the AWI since 2002 with deployment
           years denoted next to the positions.

this boundary at approximately 56.3°S, about 170 km further south than the south-
ernmost PIES. The array covers most of the ACC including the Subantarctic Front
(SAF) and the Polar Front (PF). These two fronts are associated with the major
ACC transport (e.g. Peterson and Whitworth III, 1989; García et al., 2002). PIES
are deployed as free fall landers and measure ocean bottom pressure p_{bot} and acous-
tic travel time τ at intervals of 10 to 30 min. Acoustic travel time is the time an
acoustic signal needs to get to the sea surface and back to the bottom. The raw
data is processed with the PIES processing toolbox from the University of Rhode
Island/ Graduate School of Oceanography (URI/GSO Kennelly et al., 2007) to re-
move outliers. The bottom pressure signal is drift corrected by using either a linear
or an exponential fit. The tides are removed from the bottom pressure signal using
the empirical ocean tide model EOT08a (Savcenko and Bosch, 2008). Furthermore
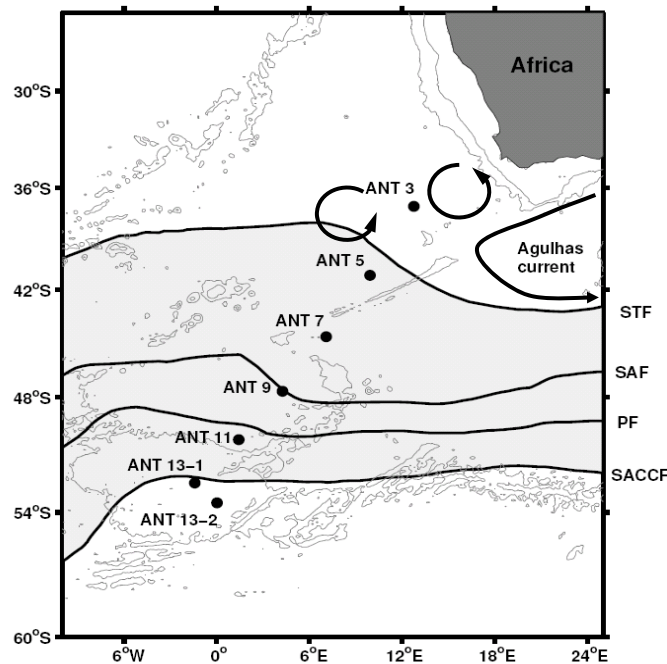
Figure 2.2: Schematic representation of the main current systems in the deployment area of the PIES. Deployment sites of the PIES are marked by black dots. Black lines indicate the major fronts: Subtropic Front (SAF), Subantarctic Front (SAF) and Polar Front (PF) and Southern ACC Front (SACCF) [Orsi et al., 1995]. The gray shaded area marks the area of the Antarctic Circumpolar Current (ACC) bounded by the STF and the SACCF. Indicated as gray lines are the 0 m, 1000 m and 3000 m isobaths.

hourly means are derived for acoustic travel time and bottom pressure. The bottom pressure data is additionally filtered with a 100 hour low pass filter to remove barotropic waves.

Figure 2.3 shows potential temperature against salinity from CTD-casts conducted during the 19 cruises of the RV Akademik Sergey Vavilov (ASV-19)[2]. Indicated by solid black lines are the three major fronts; STF, SAF and PF. The literature provides a lot of different criteria for the fronts, the criteria used in this work are listed in Table 2.2.

---

[2]Many thanks to Sabrina Speich who provided the data.
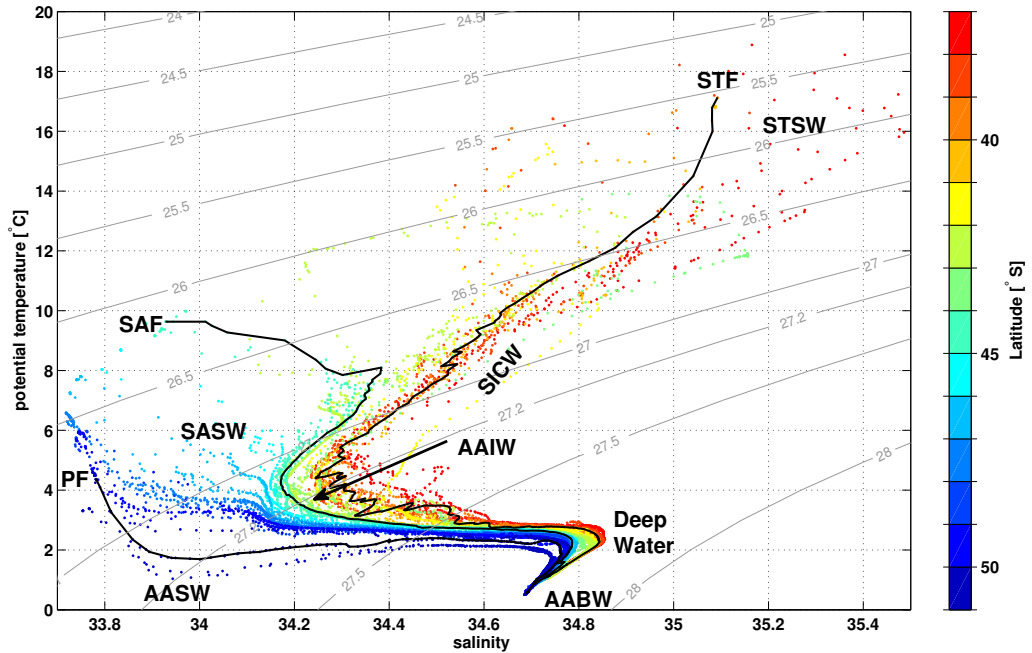
Figure 2.3: θ-S plot of a CTD-section along the Good Hope line, where the color represent the latitude. Indicated as gray contours are the σ_0 isopycnals [kg/m^3], the solid black lines are the Subtropic Front (STF), the Subantarctic Front (SAF), and the Polar Front (PF). Furthermore the following water masses are indicated by labels; Subtropical Surface Water (STSW), South Indian Central Water (SICW), Red Sea Water (RSW), Antarctic Surface Water, Antarctic Intemediate Water (AAIW), Deep Water including North Atlantic, North Indian, Upper and Lower Circumpolar Deep Water and Antarctic Bottom Water (AABW).

Furthermore the water masses are indicated by label. Three types of surface waters are observed in the region. The most northern surface water is the Subtropical Surface Water (STSW) with temperatures between 15°C and 25°C and salinities 34.6 to 35.5 (Darbyshire, 1966). Between the STF and the PF the surface water is dominated by Subantarctic Surface Water (SASW). Near the Subtropical Front the SASW reaches salinities of 34.3 to 34.4 and temperatures between 7 and 8°C. Farther south the salinity of SASW drops to 33.8 - 33.9 with temperatures of 3 - 4°C (Deacon, 1937). South of the Polar Front, Antarctic Surface Water (AASW) is observed with salinities ranging between 33.8 and 34.6 and temperatures of about

Table 2.2: Criteria for the three major fronts of the Good Hope line

front	criteria	source
STF	S_{100}=34.8	Orsi et al. (1995)
SAF	S_{100}=34.3	Park et al. (1993)
PF	T_{200}=2°C	Orsi et al. (1993)

1°C (Deacon, 1937). Below the STSW a core of South Indian Central Water (SICW) is located with salinities of 34.6 to 35.5 and temperatures of 8 to 15°C (Sverdrup et al., 1942). The clear salinity minimum beneath the surface is formed by Antarctic Intermediated Water (AAIW) centered at a density (σ_0) of 27.2 kg/m^3 (Read and Pollard, 1993). The Deep Water below the AAIW is a mixture of three major deep waters of the region: North Atlantic Deep Water (NADW), North Indian Deep Water (NIDW) and upper/lower Circumpolar Deep Water (CDW). Concerning temperature and salinity all three deep water masses have very similar properties, distinguishable only by their nutrient and dissolved oxygen content. The densest water mass found along the section is Antarctic Bottom Water (AABW) with salinities below 34.75 and temperatures below 0.5°C (Deacon, 1937). The color code in Figure 2.3 indicates the latitude of each profile. The water masses north of 42°S originate in the tropic and subtropic ocean while the water south of 42°S is formed in the Southern Ocean.

The PIES were deployed at cross-over points of the satellite altimeters Topex/Poseidon, Jason 1 and Jason 2. The advantage of cross- over points is that the satellite measures twice within a repeat cycle (e.g. 10 days for Jason 1 and 2) and hence the temporal coverage is better than elsewhere. The sea surface height anomaly (SSH) measured by the satellites is a combination of baroclinic and barotropic contributions, which can not be distinguished from the satellite measurements alone. The baroclinic part of SSH anomalies is generated by density gradients while the barotropic SSH part is generated by pressure gradients. PIES provide the possibility to investigate the contribution of each part. The baroclinic part is addressed via the acoustic travel time while the pressure to address the barotropic part is measured directly.

This chapter investigates the possibility to derive basic oceanographic properties like temperature, salinity, geostrophic transport, baroclinic and barotropic sea surface height anomalies from PIES deployed south of Africa.

2.2 Methods

2.2.1 Gravest Empirical Mode

Statistical tools like the empirical orthogonal function (EOF) analysis have been frequently used to reduce the complexity of hydrographic data sets. Fukumori and Wunsch (1991) showed that the first six EOF modes are able to explain 92% of the variance in the North Atlantic. The first dynamical or "gravest baroclinic" mode is commonly used as a representation of the vertical structure of a stratified ocean. Meinen and Watts (2000) developed a method to project hydrographic profiles into baroclinic stream function space called it Gravest Empirical Mode (GEM) method. The baroclinic stream function is a vertically integrated property. The method makes no assumption about the vertical structure, in fact simply fits hydrographic data empiricaly. The GEM method only works within regions where the water masses are well distinguished and hence the projection is unique. In this work temperature/salinity profiles are projected onto acoustic travel time. In the Southern Ocean, GEM is feasible as there is a monotonic north-south gradient in temperature, and hence in sound speed and acoustic travel time.

2.2.1.1 Sound velocity and acoustic travel time

The property commonly known as the sound velocity is the phase velocity of a sound wave following the d'Alembert-equation (Eq. 2.1).

$$\frac{\partial^2 p}{\partial t^2} = \frac{K}{\rho} \frac{\partial^2 p}{\partial x^2} \tag{2.1}$$

In Eq. 2.1 p denotes the pressure, K the bulk modulus, ρ the density and x the direction of the wave propagation. The phase velocity c of a wave following Eq. 2.1 is shown in Eq 2.2.

$$c = \sqrt{\frac{K}{\rho}} \tag{2.2}$$
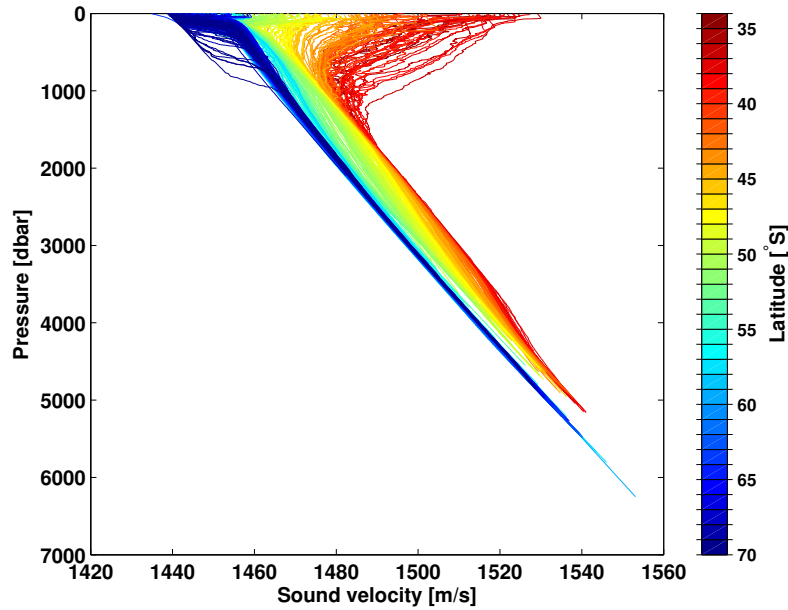
Figure 2.4: Sound velocity profiles along the Good Hope line, were the colors indicate
the latitude.

with the bulk modulus K being

$$K = -\frac{p}{\Delta V/V}$$

with p denoting the pressure and $\Delta V/V$ the relative volume change.

In sea water density is a function of temperature, salinity and pressure, hence
sound velocity also depends on temperature, salinity and pressure. For computing
the sound velocity the empirical formula of Fofonoff and Millard Jr. (1983) is used
to compute sound velocity.
Figure 2.4 shows the sound velocity profiles along the Good Hope line derived from
several CTD (Conductivity Temperature Depth) profiles. The latitude of the pro-
file is indicated by color from the northern end in red to the southern end in blue.
The upper 2000 dbar are dominated by the individual thermohaline structure while
below 2000 dbar the sound velocity is proportional to the pressure.

The acoustic travel time is twice the vertical integral over depth of the inverse

sound velocity (Eq. 2.3).

$$\tau = 2 \cdot \int_0^{z_b} \frac{dz}{c(T, S, z)} \tag{2.3}$$

The factor 2 is necessary because the PIES measure round trip travel time from the bottom to the surface and back. The PIES were deployed at different depths hence their mean travel times vary due to the deployment depth. To determine the differences between two PIES due to thermohaline effects a common reference level of 2000 dbar was chosen. The sound velocity below 2000 dbar is approximately a linear function of depth. Therefore a linear function (Eq. 2.4) representing the relation between sound velocity and depth was determined for each latitude using CTD profiles. To derive the acoustic travel time needed from the bottom to 2000 dbar and back Eq. 2.5 is used.

$$c_z = a(Lat) \cdot z + b(Lat) \tag{2.4}$$

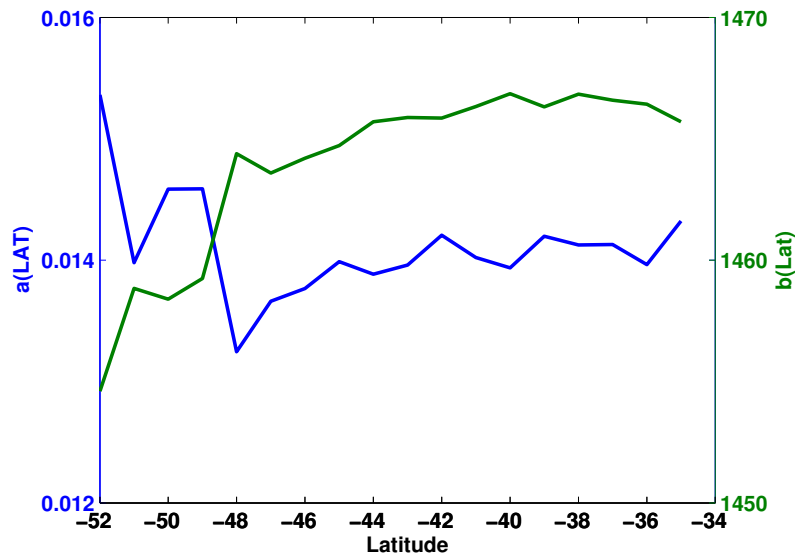$$\tau_{2000\ dbar-bottom} = 2 \cdot \int_{z(p_b)}^{z(2000dbar)} \frac{dz}{c_z(Lat)} \tag{2.5}$$

Figure 2.5: Coefficients a and b of the linear function (Eq 2.4) used to derive sound speed below 2000 dbar according to latitude.

Figure 2.5 shows the coefficients a (blue curve) and b (green curve) of the linear functions (Eq 2.4) for each latitude. Table 2.3 lists the coefficients for the PIES along the Good Hope line.

Table 2.3: Linear coefficients a and b at the PIES positions used to determine the travel time below 2000 dbar

PIES	a [1/s]	b [m/s]
ANT 3	0.0141	1466.6
ANT 5	0.0140	1466.3
ANT 7	0.0140	1464.7
ANT 9	0.0132	1464.4
ANT 11	0.0146	1458.4
ANT 13	0.0160	1452.1
ANT 13-2	0.0160	1451.6

Using Eq. 2.5 and the linear coefficients of Table 2.3, acoustic travel times relative to 2000 dbar were calculated for each PIES. Therefore the travel time between 2000 dbar and the measured bottom pressure was derived and subtracted from the measured travel times. Because this method is highly dependent on the absolute bottom pressure which is very uncertain the acoustic travel times relative to 2000 dbar were compared with CTD profile derived from 2000 dbar travel times. It was not possible to associate a CTD profile to the time series ANT 7-1, ANT 5-1 and ANT 11-1. For ANT 7-1 the correction was made such that the end of ANT 7-1 aligns with the beginning of the ANT 7-2. The mean of ANT 5-1 was corrected to the mean of ANT 5-2. For the time series of ANT 11-1 no off-set correction could be made due to a lack of data. Hence this data is not used for further investigations. Table 2.4 lists the off-set values for each time series.

Table 2.4: Off-set values for each time series.

PIES	off-set [s]
ANT 3-1	0.0069
ANT 5-1	0.0067
ANT 5-2	0.0089
ANT 7-1	0.0043
ANT 7-2	0.0107
ANT 9-1	0.0088
ANT 11-2	0.0091
ANT 13-1	0.0042
ANT 13-2	0.0095

2.2.1.2 Lookup Table

The key idea behind the GEM method is to assign a unique temperature/salinity profile to each acoustic travel time measurement. To this end a lookup table is created for temperature and salinity (Fig. 2.6). A data set of 56 CTD-casts conducted between 1990 and 2008 (listed in Table 2.5) and 126 ARGO float profiles (http://www.argo.ucsd.edu/index.html) was used for its creation. The data was interpolated onto pressure intervals of 25 dbar between the surface and 2000 dbar. A smoothing spline (Reinsch, 1967) was applied along each pressure level to derive a unique function between travel time and temperature/salinity. Figure 2.6 show the final lookup tables for temperature and salinity. The three major fronts in this domain are also indicated in Figure 2.6. From north to south these are the Subtropical Front (STF, salinity at 100 m equals 34.8 (Orsi et al., 1995)), the Subantarctic Front (SAF, salinity at 100 m equals 34.3 (Park et al., 1993)) and the Polar Front (PF, temperature at 200 m equals 2°C Orsi et al. (1993)).

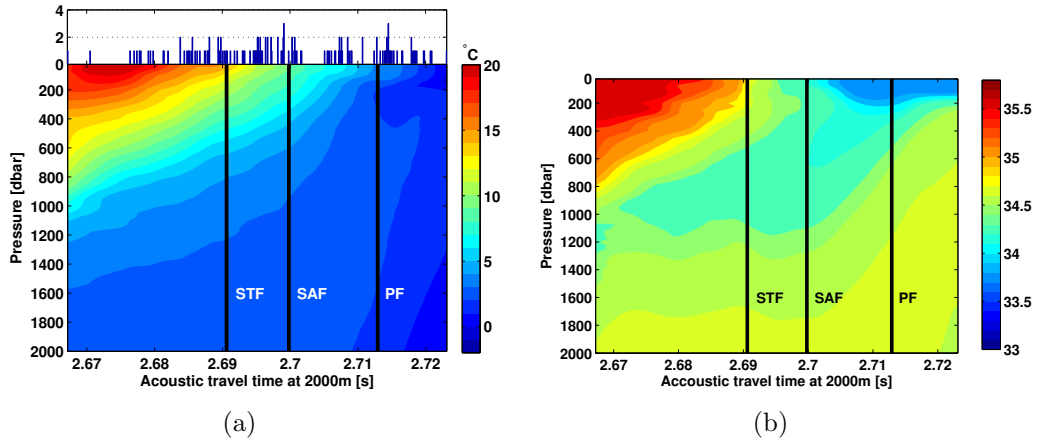(a)   (b)

Figure 2.6: Lookup tables for (a) temperature and (b) salinity. On top of the lookup
           table for temperature a histogram of the available profiles for each travel
           time is plotted.

Table 2.5: From the cruises below profiles deeper than 2000 dbar along the Good
          Hope line are used to create the lookup table and the coefficients of the
          linear sound velocity function below 2000 dbar (Eq. 2.4). The cruises
          were conducted during austral spring, summer and autumn.

ship	cruise	year	source
Meteor	M11/5	1990	WOCE Hydrographic Programme (2002)
Polarstern	ANT-X/4	1992	WOCE Hydrographic Programme (2002a)
Polarstern	ANT-XI/2	1993/94	Fahrbach (2010)
Polarstern	ANT-XV/4	1998	Fahrbach and Rohardt (2007a)
Polarstern	ANT-XVI/2	1998/99	Fahrbach and Rohardt (2007b)
Polarstern	ANT-XVIII/3	2000/01	Fütterer and Rohardt (2007)
Polarstern	ANT-XX/2	2002/03	Fütterer and Rohardt (2007a)
Polarstern	ANT-XXI/3	2004	Arntz and Rohardt (2007)
Polarstern	ANT-XXII/2	2004/05	Spindler and Rohardt (2007)
Polarstern	ANT-XXIII/7	2006	Rohardt (2009)
Polarstern	ANT-XXIV/3	2008	Rohardt (2009a)

In Figure 2.6(a) a histogram is plotted on top to illustrate the distribution of the
profiles used to create the lookup table. The histogram shows some gaps mainly
located at short travel times which correspond to the northern end of the Good
Hope line. The gaps might be caused by the presence of Agulhas rings, which carry

anomalous warm and salty water corresponding to short acoustic travel times. The two profiles with acoustic travel time below 2.675 s hence were most likely sampled within Agulhas rings. Furthermore the station spacing at the northern end of the Good Hope line is much coarser compared to the southern end.

(a)   (b)
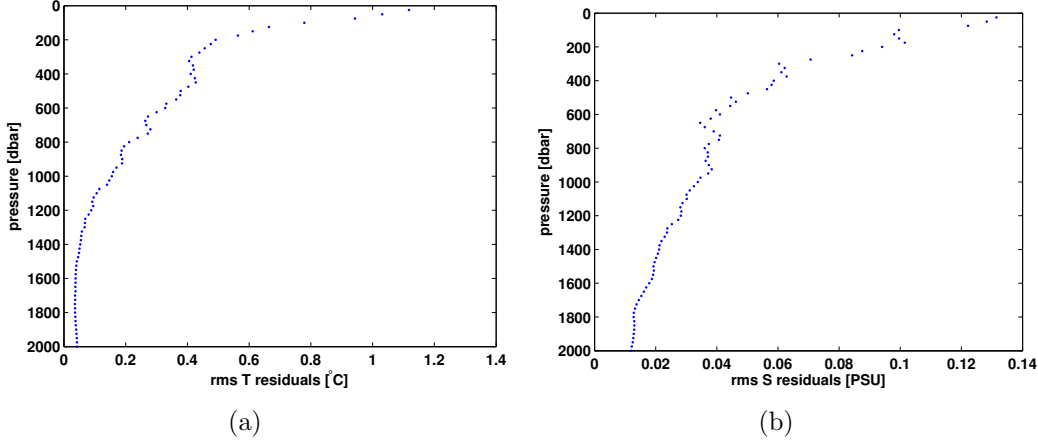
Figure 2.7: Root Mean Square error derived from the difference between the measured profiles and the lookup table.

To give an estimate of the accuracy of the lookup tables the Root Mean Square (RMS) error was calculated between the lookup tables and the measured profiles used to create them (Figure 2.7). The RMS errors shown in Figure 2.7 decrease with depth but are somewhat higher than Watts et al. (2000b) found south of Australia. Watts et al. (2000b) deployed their IES only between 48°S and 52°S. Hence their lookup table covers a smaller band of travel times with less variability, which might be an explanation for the smaller salinity RMS errors.

Due to the smoothing process, a lookup table only represents the gross features of the variability in a particular region. Figure 2.8 shows the percent variance γ (Eq. 2.6) captured by the lookup table.

$$\gamma = 1 - \frac{\sigma_{res}^2}{\sigma_{obs}^2} \tag{2.6}$$

Where σ_{res} is the standard deviation of the measurements minus the lookup table data and σ_{obs} is the standard deviation of the measurements. The lookup table for

Figure 2.8: Percent variance covered by the lookup table. The blue dots denote the
variance covered by the temperature lookup table and red dots represent
the covered variance by salinity.

temperature captures at least 95% of the variance throughout the upper 2000 dbar.
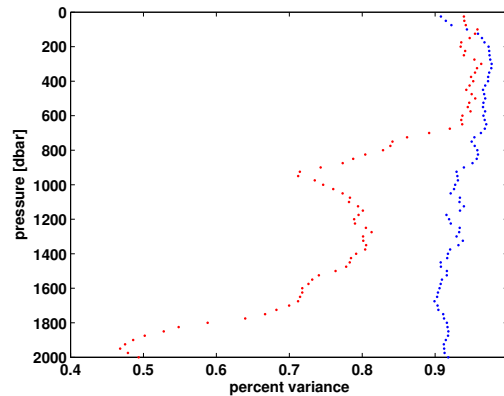The salinity lookup table catures between 97% and 94% in the upper 650 dbar.
Below 650 dbar γ drops down to a first minimum of 71% at 950 dbar after recovering
to 80% between 1200 and 1400 dbar γ drops down to of 47% at 1950 dbar. A similar
behavior was found by Watts et al. (2000b) while their γ minimum was only 85%.
This drop in captured variance may be due to regional differences between profiles
of similar acoustic travel time, containing either more saline North Atlantic Deep
Water (NADW) or less saline Antarctic Intermediate Water (AAIW) (e.g. Lynn and
Reid, 1968). As salinity has only a minor influence on sound speed (in contrast to
temperature), salinity signals independent from temperature changes (NADW and
AAIW being both near 2°) can not be captured by the GEM look up table. The
captured variance starts to recover after 1950 dbar and reaches 50% at the maximum
depth (2000 dbar) of the lookup table.

To investigate the robustness of the lookup tables they were tested against an
independent data set of CTD profiles kindly provided by Sabrina Speich. Therefore
the acoustic travel times relative to 2000 dbar were calculated from the CTD profiles
and the measured profiles were subtracted from the corresponding ones in the lookup
table (Figure 2.9). The colors in Figure 2.9 indicate the latitude of the profile. The
highest temperature differences occur in the upper 400 m and in the northern part
of the section. One profile at about 42°S with extreme high temperature differences
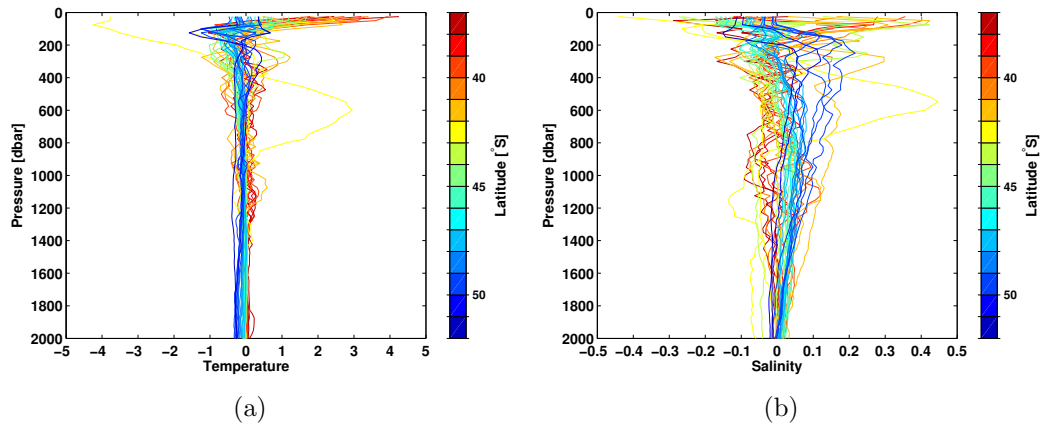
Figure 2.9: Differences between independently measured (a) temperature and (b) salinity profiles and the lookup table, with colors indicating the latitude.

is due to the presence of an Agulhas ring (Gladyshev et al., 2008). The same holds true for the salinity differences but the decrease with depth is not as large as for temperature.
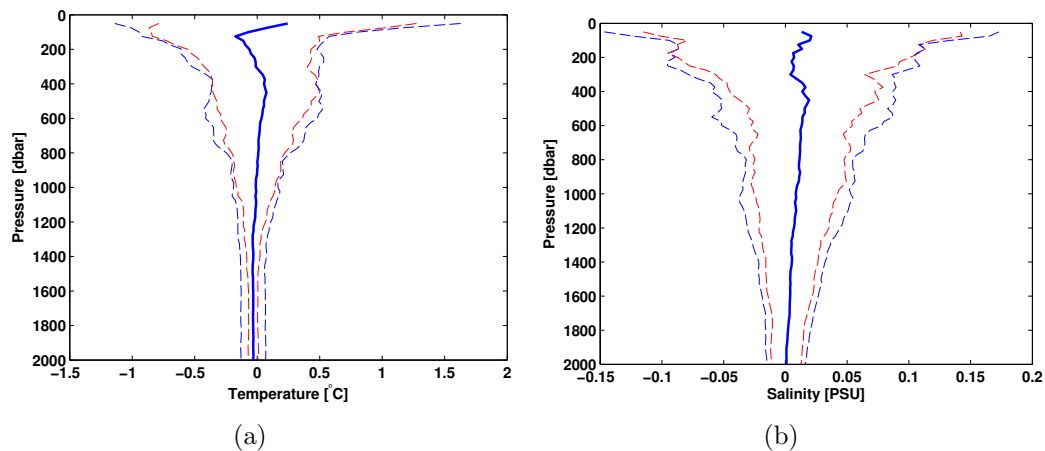

Figure 2.10: Mean difference (solid blue line) between measured (a) temperature and (b) salinity profile and the lookup table with standard deviation (dashed blue lines) and RMS error of the lookup table (dashed red lines).

Figure 2.10 shows the mean and standard deviation of the temperature and salinity differences derived to test the lookup table in blue and the RMS error of the

lookup table in red. The standard deviation is slightly higher than the RMS error. The test with an independent data set hence shows that the lookup tables created produce reliable temperature and salinity profiles. Furthmore the RMS error of the lookup table is used to estimate the error of the transport calculation through an error propagation.

2.2.2 Sea surface height (SSH) anomaly

The sea surface height (SSH) anomaly or sea level anomaly (SLA) consists of a baroclinic (steric) part η_{bc} and a barotropic (eustatic) part η_{bt}. The baroclinic part η_{bc} is caused by density changes in the water column compared to the surrounding waters while variable mass loading leads to the barotropic (eustatic) part η_{bt}. Equations to derive both parts are deduced from the integration of the hydrostatic relation (Eq.2.7)

$$\int_{-H}^{\eta'} dz = -\int_{p_{bot}}^{p_a} \frac{1}{\rho g} dp \tag{2.7}$$

With η' being the sea surface height anomaly, H the mean ocean depth, p_a the atmospheric pressure, p_{bot} the ocean bottom pressure, ρ the density of the water column and g the gravitational acceleration. The atmospheric pressure is separated into a time mean $\bar{p}_a$ and a time varying part p'_a.

$$p_a = \bar{p}_a + p'_a$$

Solving the left hand side and using the separation of the atmospheric pressure into a time mean and time varying part Eq. 2.7 becomes:

$$
\begin{aligned}
\eta' + H &= \int_{\bar{p}_a}^{p_{bot}} \frac{1}{\rho g} dp + \int_{p_a}^{\bar{p}_a} \frac{1}{\rho g} dp \\
&= \int_{\bar{p}_a}^{p_{bot}} \frac{1}{\rho g} dp + \underbrace{\frac{\bar{p}_a - p_a}{\rho_s g}}_{\eta_{IB}}
\end{aligned}
\tag{2.8}
$$

With ρ_s denoting the density at the surface and η_{IB} the isostatic oceanic response to atmospheric loading commonly known as inverse barometer (IB) effect. Sea

surface height products such as AVISO (http://www.aviso.oceanobs.com/duacs/) have been corrected for this effect hence η_{IB} in Eq. 2.8 moves to the left hand side. Furthermore using the same separation into a time mean $\bar{p}$ and a time varying part p' for ocean bottom pressure as used for the atmospheric pressure Eq. 2.8 becomes Eq. 2.9:

$$
\begin{aligned}
\eta' - \eta_{IB} + H &= \int_{\bar{p_a}}^{p_{bot}} \frac{1}{\rho g} dp \\
&= \int_{\bar{p_a}}^{\bar{p}} \frac{1}{\rho g} dp + \int_{\bar{p}}^{p_{bot}} \frac{1}{\rho g} dp \\
&= \frac{1}{g} \int_{\bar{p_a}}^{\bar{p}} [\alpha(35, 0, p) + \delta] dp + \frac{p_{bot} - \bar{p}}{\rho_b g} \\
&= \underbrace{\frac{1}{g} \int_{\bar{p_a}}^{\bar{p}} \alpha(35, 0, p) dp}_{} + \underbrace{\frac{1}{g} \int_{\bar{p_a}}^{\bar{p}} \delta dp}_{} + \frac{p_{bot} - \bar{p}}{\rho_b g} \\
&= \qquad H_{SO} \qquad + \qquad \frac{\Phi_{\bar{p}}}{g} \quad + \frac{p_{bot} - \bar{p}}{\rho_b g} \qquad (2.9)
\end{aligned}
$$

The first term of the right side of Eq. 2.9 is the height of the Standard ocean (H_{SO}) resulting from the separation of the specific volume ($\alpha = 1/\rho$) into the specific volume of sea water with a salinity of 35 PSU, a temperature of 0°C, the pressure p and the specific volume anomaly δ.

$$
\alpha(S, T, p) = \alpha(35, 0, p) + \delta
$$

While the second term denotes the change in sea surface height due to density changes commonly know as the baroclinic or steric part (η_{bc}) of sea surface height. With $\Phi_{\bar{p}}$ being the geopotential height anomaly relative to $\bar{p}$. The third term denotes the time varying changes due to variable mass loading known as barotropic or eustatic part (η'_{bt}) of sea surface height. With ρ_b being the density at the bottom relative to a common reference level. In this work the geopotential height anomaly can only be calculated relative to 2000 dbar because of the limitation of the look up table and hence the limitation of density profiles. But the density changes below 2000 dbar are negligible and therefore the time varying geopotential height anomaly relative to 2000 dbar is approximately the same as relative to the mean pressure $\bar{p}$.

The baroclinic part of the sea surface height is separated into a time mean and a time varying part.

$$\eta_{bc} = \bar{\eta}_{bc} + \eta'_{bc}$$
$$= \frac{\bar{\Phi}_{\bar{p}}}{g} + \frac{\Phi'_{\bar{p}}}{g}$$
$$\approx \frac{\bar{\Phi}_{\bar{p}}}{g} + \frac{\Phi'_{2000}}{g} \tag{2.10}$$

The sea surface height anomaly η' is the sum of the baroclinic component η'_{bc} and the barotropic component η'_{bt} (Eq. 2.11) because all other parts of Eq. 2.9 aside the inverse barometer effect (η_{IB}) are constant in time. The inverse barometer effect is a purely atmospheric feature and will be separately corrected in every measurement using atmospheric models.

$$\eta' = \eta'_{bc} + \eta'_{bt}$$
$$= \frac{\Phi'_{\bar{p}}}{g} + \frac{p_{bot} - \bar{p}}{\rho_b g}$$
$$\approx \frac{\Phi'_{2000}}{g} + \frac{p_{bot} - \bar{p}}{\rho_b g} \tag{2.11}$$

The density ρ_b in Eq. 2.11 is the typical potential density ($\sigma_2 = 1037 \ kg/m^3$) relative to 2000 dbar of deep water in this region. Eq. 2.11 consists of properties, which are directly measured or derived from PIES. Hence the sea surface height anomalies are derived from PIES and separated into their baroclinic and barotropic component. The total SSH anomalies η derived from PIES are compared with measurements from satellite altimeters such as TOPEX/Poseidon or Jason 1 and gridded products such as AVISO.

The variance of the total SSH anomaly $\sigma^2(\eta')$ is the sum of the variances of the baroclinic $\sigma^2(\eta'_{bc})$ and barotropic $\sigma^2(\eta'_{bt})$ part plus two times the covariance of the two parts (Eq. 2.12). Eq. 2.13 is used to calculate the percentage of variance captured by either the baroclinic (Bc) or the barotropic (Bt) part.

$$\sigma^2(\eta') = \sigma^2(\eta'_{bc}) + \sigma^2(\eta'_{bt}) + 2 \cdot cov(\eta'_{bc}, \eta'_{bt}) \tag{2.12}$$

$$Bc = \frac{\sigma^2(\eta'_{bc})}{\sigma^2(\eta') - 2 \cdot cov(\eta'_{bc}, \eta'_{bt})} \qquad Bt = \frac{\sigma^2(\eta'_{bt})}{\sigma^2(\eta') - 2 \cdot cov(\eta'_{bc}, \eta'_{bt})} \qquad (2.13)$$

2.2.3 Geostrophic velocities

The momentum equation (Eq. 2.14) derived from Newton's second law relates the forces acting on a water parcel in the ocean to the change of velocity v.

$$\frac{D\vec{v}}{Dt} = \frac{\vec{F}}{m}$$
$$= \underbrace{-\alpha \nabla \vec{p}}_{\substack{\text{pressure} \\ \text{gradient}}} \quad \underbrace{-2\vec{\Omega} \times \vec{v}}_{\substack{\text{Coriolis} \\ \text{acceleration}}} + \underbrace{\vec{g}}_{\substack{\text{gravity} \\ \text{acceleration}}} + \underbrace{\vec{F}_r}_{\text{friction}} \qquad (2.14)$$

With $\alpha = 1/\rho$ and Ω being the angular velocity vector of the Earth.

In the ocean's interior away from coasts and below the Ekman layer the pressures gradient force nearly balances the Coriolis force, which is called geostrophic balance. The geostrophic flow is assumed to be steady with horizontal velocities much larger than vertical velocities and friction being negligible. Eq. 2.14 hence simplifies to:

$$\frac{1}{\rho}\frac{\delta p}{\delta x} = fv$$
$$\frac{1}{\rho}\frac{\delta p}{\delta y} = -fu$$
$$\frac{1}{\rho}\frac{\delta p}{\delta z} = -g \qquad (2.15)$$

The geostrophic balance only holds true if the horizontal distances exceed about 50 km and the times exceed a couple of days. Using the hydrostatic relation for pressure:

$$p = g \int_{-h}^{0} \rho(z)dz$$

and $\rho = \rho_0 = 1000$ kg/m^3 in the geostrophic approximation Eq 2.15 is rewritten to

determine the geostrophic velocity from density profiles:

$$
\begin{aligned}
v &= \frac{1}{\rho_0 f}\frac{\delta p}{\delta x} \\
&= \frac{g}{\rho_0 f}\frac{\delta}{\delta x}\int_{z_0}^{z'}\rho(z)dz \\
&= \frac{g}{\rho_0 f}\int_{z_0}^{z'}\frac{\delta\rho(z)}{\delta x}dz
\end{aligned}
\tag{2.16}
$$

Writing Eq. 2.17 as a discrete recursive assignment it becomes:

$$
v_g(z+dz) = v(z) + \frac{g}{\rho_0 f}\frac{d\rho(z)}{dx}dz \tag{2.17}
$$

With z denotes the discrete pressure levels, dz refers to interval of pressure levels $(dz = p(z+dz)-p(z))$ and $d\rho/dx$ referring to the horizontal density gradient between two stations.

2.2.4 Baroclinic transport

To derive the total baroclinic transport full depth geostrophic velocity profiles are needed. The temperature and salinity profiles from the GEM analysis deliver no full depth profiles because of the lookup table limitation to 2000 dbar. It was shown in Figure 2.4 that the sound velocities below 2000 dbar feature no variability at constant latitude. Hence mean CTD profiles at the PIES positions were used to create full depth temperature and salinity profiles.

For each PIES position Figure 2.11 shows the mean profiles of temperature and salinity and its standard deviation below 2000 dbar. The number of CTD profiles used for each mean and standard deviation are listed in Table 2.6. Because of the small standard deviation below 2000 dbar, the assumption of constant temperature and salinity profile below 2000 dbar is used to extend the profiles gained from the lookup table creating full depth profiles.

Calculating geostrophic velocities from the full depth temperature and salinity profiles involves calculating an averaged velocity profile between two sites. A problem that occurs is the different deployment depth of the two stations and the topography in between. Figure 2.12 shows the different deployment depths of the PIES
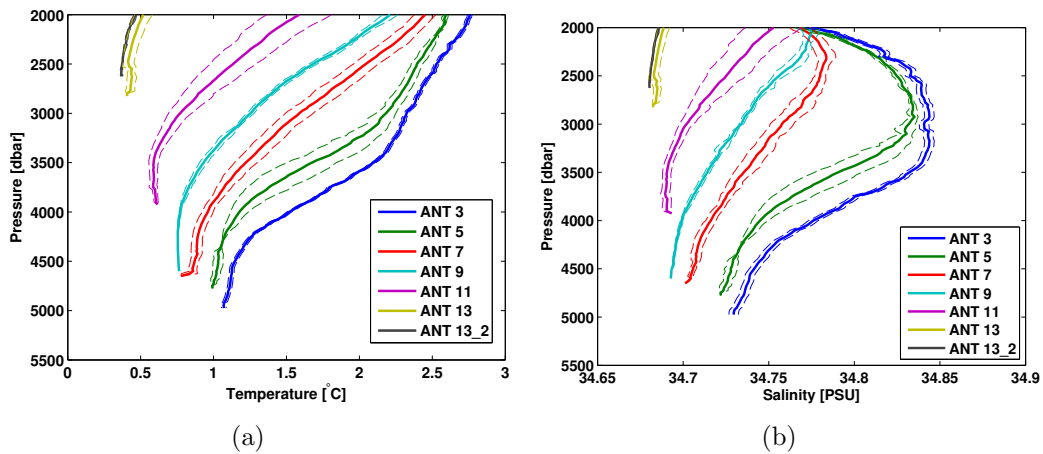
Figure 2.11: Mean full depth profiles below 2000 dbar (solid lines) of temperature and salinity derived from CTD profiles and corresponding standard deviation (dashed lines).

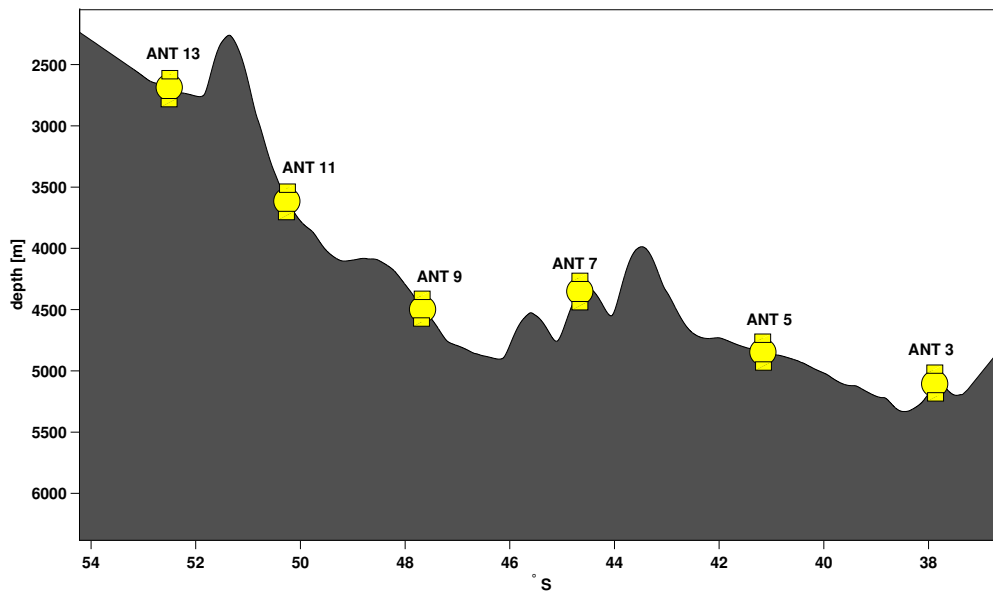and the bottom topography from a five minute terrain base database provided by the matlab function m_tbase.

Figure 2.12: Deployment depth of the pies with bottom topography along the Good Hope section.

Table 2.6: Number of profiles used for calculating the mean and the standard deviation at each PIES position.

PIES	Nr.
ANT 3	3
ANT 5	5
ANT 7	10
ANT 9	13
ANT 11	60
ANT 13	15
ANT 13_2	3

In case of the ACC PIES the pairwise difference of deployment depths vary from 30 m to 1200 m. For the transport calculation the 30 m case is insignificant but the 1200 m causes a significant difference. Furthermore Figure 2.12 shows that in between the PIES there are topographic features like the mountain between ANT 5 and ANT 7 or the trough between ANT 7 and ANT 9. To overcome this problem the common method of bottom triangles (Gerd Rohardt, personnel communication) is used. The method of bottom triangles is mostly used at continental shelfs with a step gradient in topography. The shorter profile is extrapolated for half of the depth distance between the stations by keeping the density difference constant. This method does not resolve the bottom topography in an appropriate way but is the best solution due to the coarse spacing of the PIES.

The baroclinic transport T is further derived as the vertical integral of the geostrophic velocity v_g over depth times the horizontal distance Δx between the two sites (Eq. 2.18). As a common depth level z_{12} the depth of the extrapolated v_g profile is used.

$$T = \Delta x \cdot \int_{z_{12}}^{0} v_g dz \tag{2.18}$$

2.3 Results

2.3.1 Acoustic travel times relative to 2000 dbar

The measured travel times are not directly comparable due to the different deployment depths. ANT 13_2 is the shallowest PIES and hence its travel time is lowest. In Figure 2.13 the travel times are shown referenced to a common level of 2000 dbar. More details are seen in this graph and the single sites can now be compared to each other. Applying the definition of the Subtropical Front (STF), the Subantarctic Front (SAF) and the Polar Front (PF) to the lookup tables of temperature and salinity it was possible to assign an acoustic travel time to the fronts. The fronts are shown in the lookup tables (Figure 2.6) and as horizontal lines in Figure 2.13. Caused by the temperature gradient from North to South a general increase of the travel time is expected and is seen for all three deployment periods (2003-2005, 2005-2008, 2008-2010). The travel time of ANT 3 shows the biggest variance due to the subtropical regime and the presence of Agulhas rings. The variance of the travel time of ANT 5 is clearly decreased compared to ANT 3. In January 2006 an Agulhas ring passes the position of ANT 5 and leads to a drastic change in the travel time. Swart et al. (2008) showed that the Agulhas ring seen at the position ANT 5 is also visible in the AVISO product "Maps of Absolute Dynamic Topography (MADT)". Figure 5d of Swart et al. (2008) shows that the Agulhas ring passes the position of ANT 5 with its center hence the enormous change in travel time is explained by warm and salty water trapped in the interior of the ring.

The travel time time series of ANT 7-2 also shows an increased variance in August 2006. Using a animation of MADT it becomes evident, that this feature comes from the west and propagates to the east. It belongs to the South Atlantic Current (SAC, Strammma and Peterson, 1990) which is the southern branch of the subtropical gyre. The travel times south of ANT 7 do not show such high variability due to the stable regime of the Antarctic Circumpolar Current.
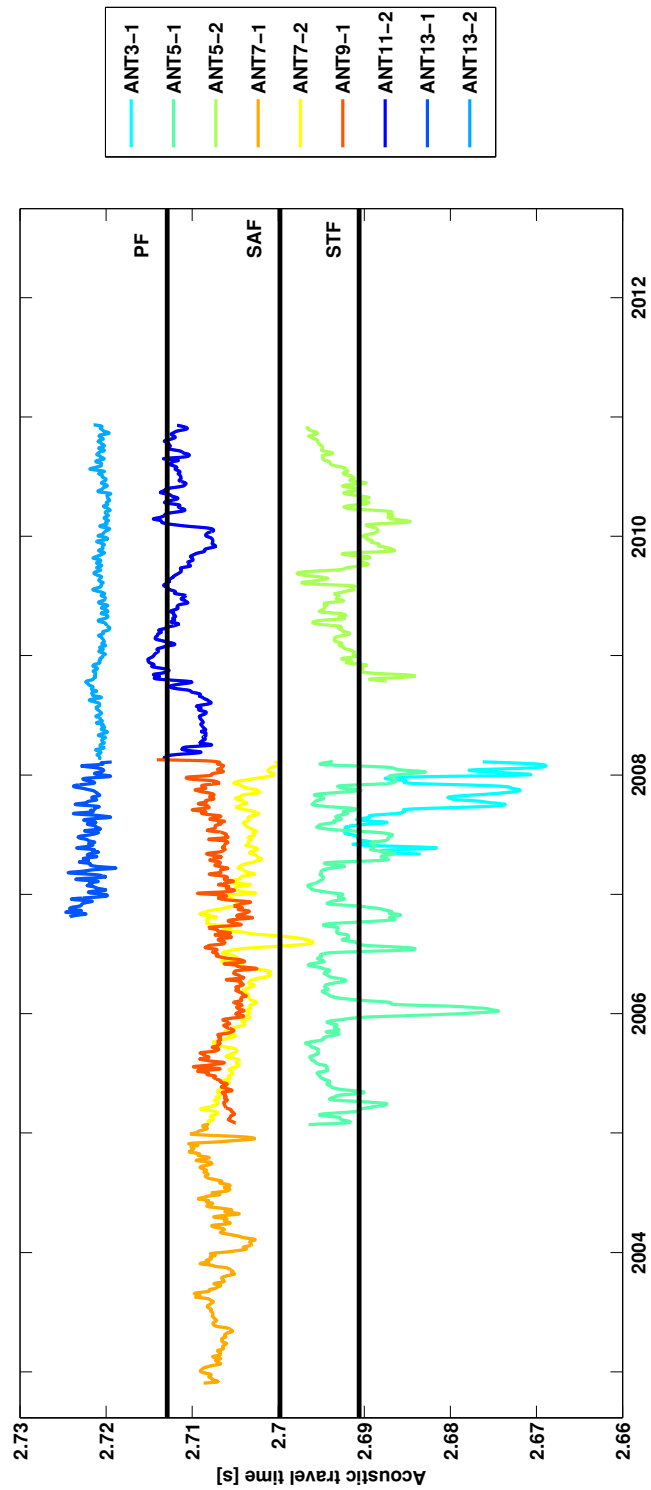
Figure 2.13: Acoustic travel time relative to 2000 dbar for all deployments between 2003 and 2010 with fronts indicated as horizontal lines.
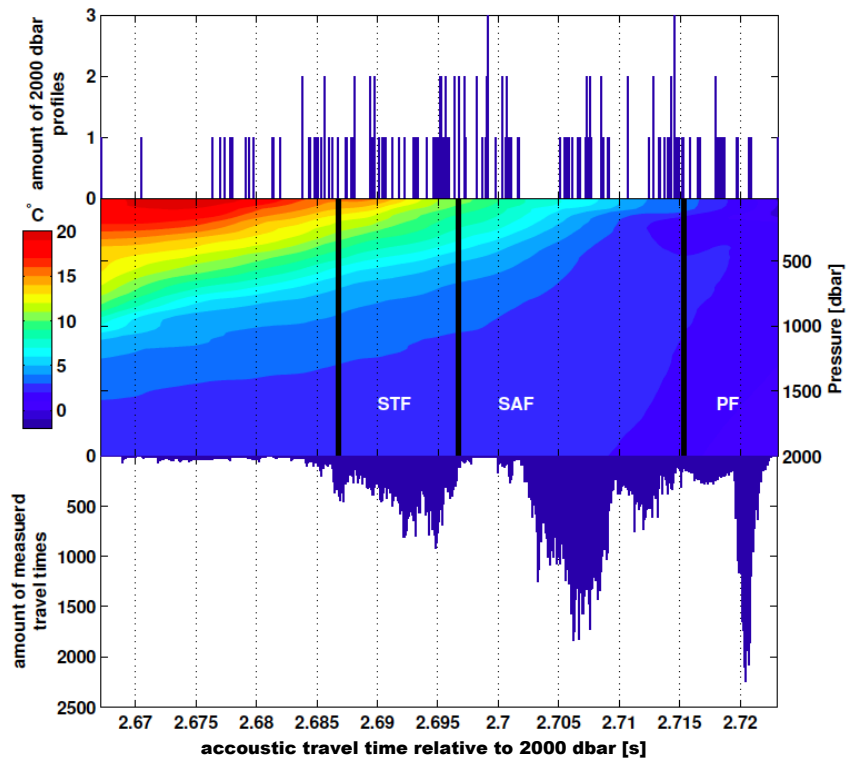
Figure 2.14: Look up table of potential temperature with a histogram of the profiles used to create the look up table on top and a histogram of all measured travel times below.

Figure 2.14 shows the look up table of potential temperature with the histogram of the measured travel times below. On top of the look up table the distribution of profiles used for its creation is plotted. The measured travel times group in three peaks centered at about 2.695 s, 2.707 s and 2.72 s. A fourth minor peak is centered at 2.713 s. The first peak is caused by the PIES ANT 3 and ANT 5, where ANT 5 causes the bulk of data because of the longer deployment and ANT 3 causes the tail with a minor maximum centered at 2.687s. The acoustic travel time of ANT 7 and ANT 9 are so closely together that they can not be distinguished in the distribution. They together cause the peak centered at 2.707 s. The minor peak at 2.713 s is caused by ANT 11 while the largest but narrowest peak at 2.72 s is caused by ANT 13. This diagram also shows that most PIES measurements are at travel times which are well represented through CTD and Argo profiles in the lookup table. The lookup table section with the largest gap of CTD and ARGO

based travel times (above 2.676 s) is only sparsely measured by PIES.

2.3.2 Temperature and salinity time series

Figure 2.15 shows the time series of potential temperature and salinity profiles derived from the acoustic travel times at the position ANT 5. The Agulhas rings described in section 2.3.1 are clearly seen throughout the whole water column as a feature of higher temperature and salinity. The time series derived from the PIES data are unique in resolution and length for this part of the Southern Ocean and provide the basis for further analysis to determine sea surface hight anomalies and transport variations.
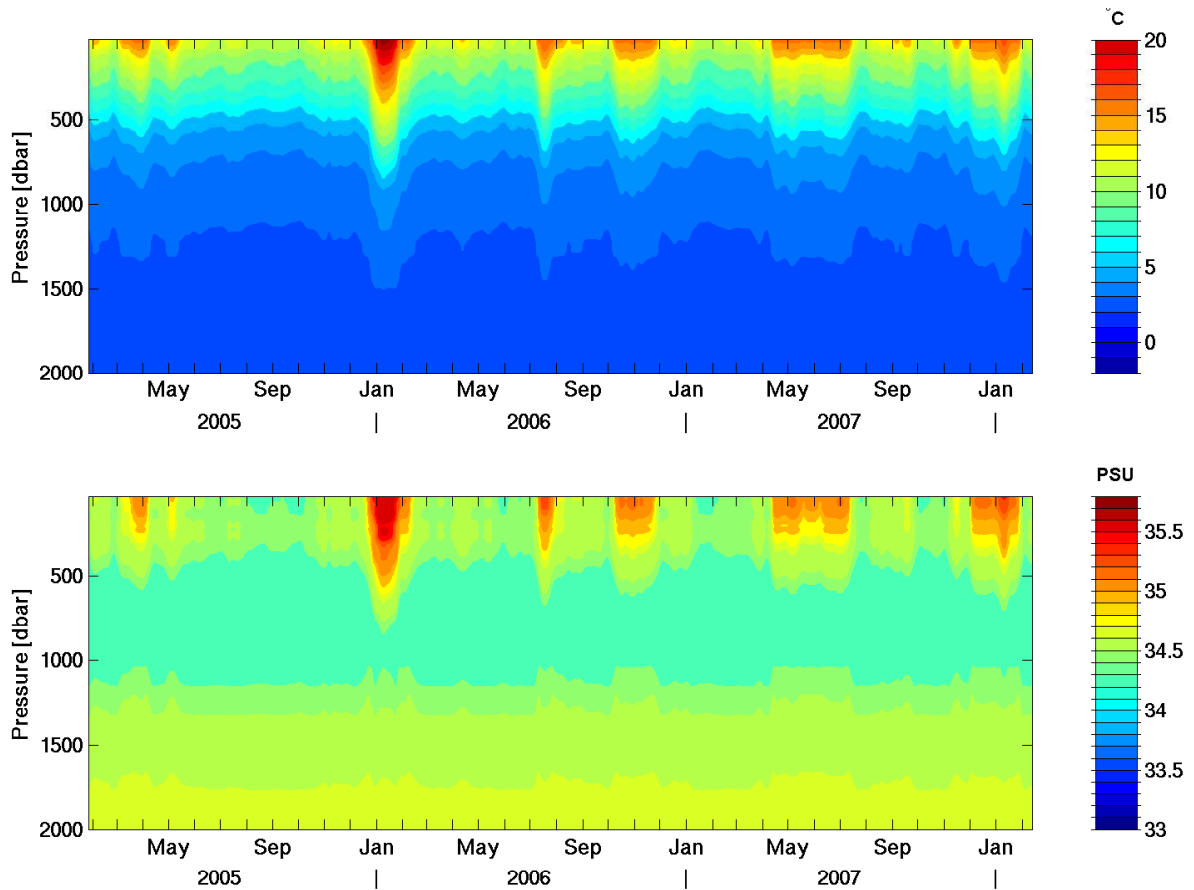

Figure 2.15: Potential temperature (top panel) and salinity (bottom panel) time series at the position ANT 5

The potential temperature and salinity time series of the other ACC PIES are

depicted in appendix B. The temperature and salinity variability decreases from
north to south. Differences are also seen between different deployment periods. For
example the first deployment of ANT 5 (Figure 2.15) shows several transitions of
Agulhas rings while the second deployment (Figure B.2) shows less Agulhas ring
activity and shallower changes in temperature and salinity. This indicates that the
Agulhas rings hit the position ANT 5 only marginally. At the position ANT 7
(Figure B.3 and B.4) a decreasing trend is observed for the second deployment
period (2005-2008). In August 2006 an anomalous warm and salty event happened.
As described in section 2.3.1 this feature is a anticyclonic eddy propagating from
west to east via the South Atlantic Drift. The positions ANT 9 (Figure B.5) and
ANT 11 (Figure B.6) show a seasonal cycle in temperature and salinity. At ANT 9
the seasonal cycle is seen in both temperature and salinity while at ANT 11 it is seen
predominantly in salinity. ANT 13 (Figure B.7 and B.8) show just low variability.
It has to be noted that the same temperature and salinity scale was used to plot
the Figures in appendix B, which might not be suitable to detect small trends
especially at the southern positions were the variability is low. Further analysis of
the temperature and salinity trend of ANT 13 is done in section 2.3.6 in conjunction
with the comparison to the Southern Ocean State Estimate (SOSE).

2.3.3 Baroclinic and barotropic SSH anomalies

Baroclinic and barotropic SSH anomalies are derived using Eq. 2.11. Dhomps et al. (2011) showed the large influence on the baroclinic variability when deepening the reference level from 700 m to 1000 m. To investigate how big this effect is in the Southern Ocean two different reference levels (1000 dbar and 2000 dbar) are used to calculate the baroclinic SSH anomalies. Table 2.7 lists an estimated error budget for the PIES measurements and the conversion into SSH anomalies. The largest uncertainty is caused by the lookup table RMS (see Figure 2.7).
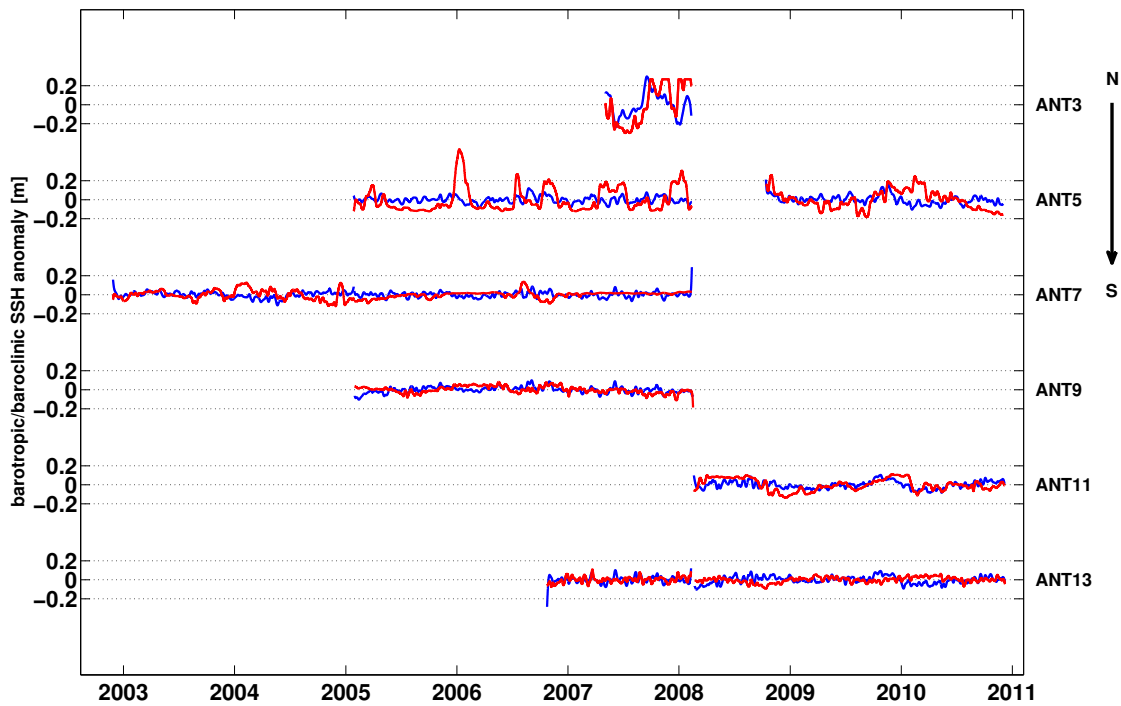

Figure 2.16: Baroclinic (red) and barotropic (blue) sea surface height derived from the PIES

Figure 2.16 shows the baroclinic (red) and barotropic (blue) part of the sea surface height (SSH) anomaly derived from PIES using Eq. 2.10. The baroclinic part is calculated relative to a reference level of 2000 dbar. The variability of the baroclinic

Table 2.7: Error budget for the PIES measurements.

PIES error budget	Measurement uncertainty	Height uncertainty [cm]
IB effect	0.13 ms	0.46
travel time (low pass)	0.08 ms	0.28
sea state	0.05 ms	0.18
lookup table RMS		2,9
pressure uncertainty	0.7 dbar	0.7
pressure drift correction	0.01 dbar	0.01
Total		4.53

part decreases from North to South. It is in the order of 0.2 m or larger for the positions ANT 3 and ANT 5. At the positions ANT 7, ANT 9 and ANT 13 it decreases to 0.03 m with an exception at the position ANT 11 where it is in the order of 0.06 m. The variability of the barotropic part is more or less constant throughout the PIES array expect for ANT 3 where it is almost as high as the baroclinic SSH anomaly.
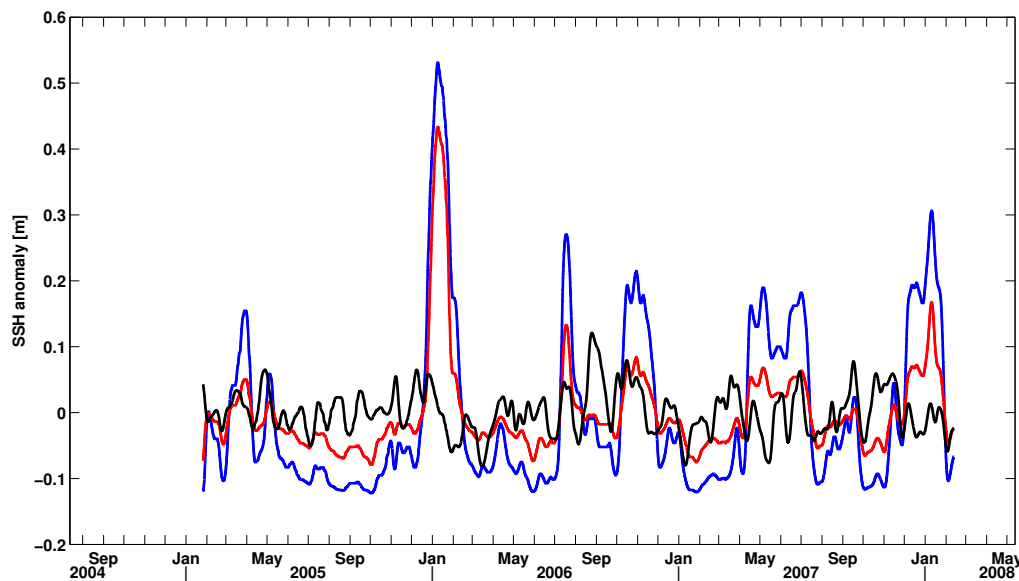

Figure 2.17: SSH anomalies derived from the PIES at the position ANT 5 for the first deployment period. The blue line represents the baroclinic SSH anomaly relative to 2000 dbar, the red line shows the baroclinic SSH anomaly for the shallow reference level of 1000 dbar and the black line represents the barotropic SSH anomaly.

Figure 2.17 shows the influence of the reference level on the variability of the baroclinic component exemplary for ANT 5. The variability of the baroclinic component relative to 1000 dbar is smaller as compared to the 2000 dbar reference level.

Table 2.8: Percent variance captured by the baroclinic (Bc) and the barotropic (Bt) part of the SSH anomaly and the total variance for the 2000 dbar and 1000 dbar reference level.

PIES	Reference level 2000 dbar			Reference level 1000 dbar		
	Bc [%]	Bt [%]	σ^2 [cm^2]	Bc [%]	Bt [%]	σ^2 [cm^2]
ANT 3	72.32	27.67	811	68.95	31.05	690
ANT 5	89.64	10.36	162	70.03	29.97	57
ANT 7	66.86	33.14	23	70.33	29.67	26
ANT 9	52.90	47.10	29	54.98	45.02	31
ANT 11	71.77	28.23	76	76.82	23.17	91
ANT 13	40.00	60.00	19	12.98	87.02	15

Table 2.8 lists the contributions to the total variability of the baroclinic (Bc) and barotropic (Bt) part of the SSH anomalies and the total variability σ^2 derived from PIES . The contributions vary strongly between positions. The contribution of the baroclinic SSH anomaly is smallest at the positions ANT 9 and ANT 13 (both ACC) for both reference levels. The barotropic component does not increase monotonically from north to south. The position ANT 11 shows a barotropic component comparable to the position ANT 5 further north. For all positions except ANT 7 (located in the South Atlantic Drift), the baroclinic component increases with reference depth. The contribution of the baroclinic SSH anomaly is smallest at the positions ANT 9 and ANT 13 (both ACC) for both reference levels.
For the two longest continuous time series at the positions ANT 7 and ANT 13 a continuous wavelet transformation (CWT, Grinsted et al., 2004) was performed to investigate the most prominent time scales of baroclinic and barotropic SSH anomaly.

Figure 2.18 shows the Continuous Wavelet Transformation of the baroclinic (a) and barotropic (b) SSH anomaly at the position ANT 7 using a Morlet wavelet. For the baroclinic part the highest wavelet power is found on semi-annual time scales ($\sim$ 180 days). The pronounced maximum on semi-annual timescales is absent in the year 2005 where the highest significant signal is observed on monthly time scales.
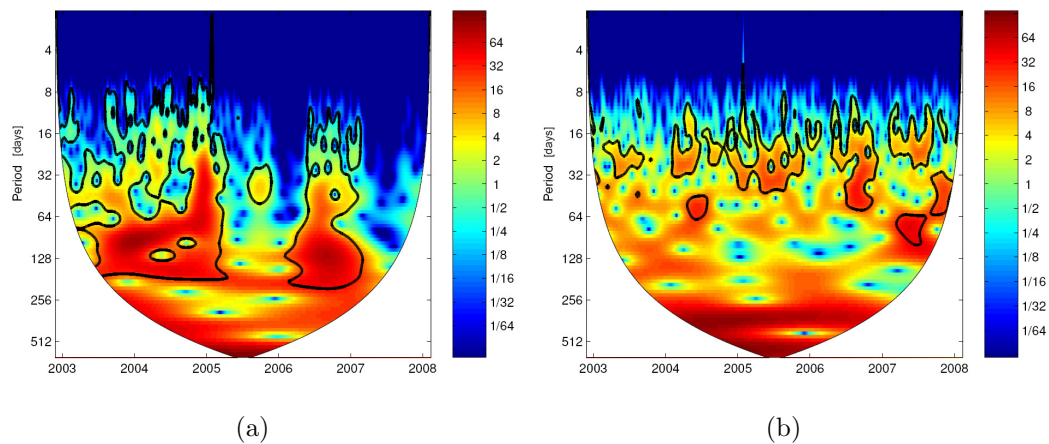
Figure 2.18: Continuous wavelet transformation of (a) the baroclinic and (b) the barotropic SSH anomaly at the position ANT 7. The contours show the power spectrum normalized by the variance. The black contour line indicates the 95% siginificance level.

For the barotropic part of the SSH anomaly significant maxima are on monthly scales ($\sim$ 30 days) but are less pronounced. An exception is found in the years 2004 and 2007 where the highest observed baroclinic signal is found on time scales between 50 and 128 days.

Figure 2.19 shows the CWT of the baroclinic and barotropic signal at the position ANT 13. The highest signal is annual for both parts. Significant signals are also found on weekly to monthly time scales (8-30 days).

Figure 2.20 shows the CWT of the baroclinic SSH anomaly relative to 1000 m at the positions ANT 7 and ANT 13. At the position ANT 7 the change in reference level affects the significance of the signal, yet only slightly it's structure. The signal at periods between 64 and 128 days in the year 2006 is slightly intensified compared to the 2000 dbar reference level (Figure 2.18(a)). Whereas at the position ANT 13 the signal is intensified at weekly to monthly timescales compared to the 2000 dbar reference level (Figure 2.19(a))and the significant signal on annual timescales has vanished in 2007. Further the weekly to monthly signals are less significant from the middle of 2008 until 2010. The results are discussed in section 2.4.
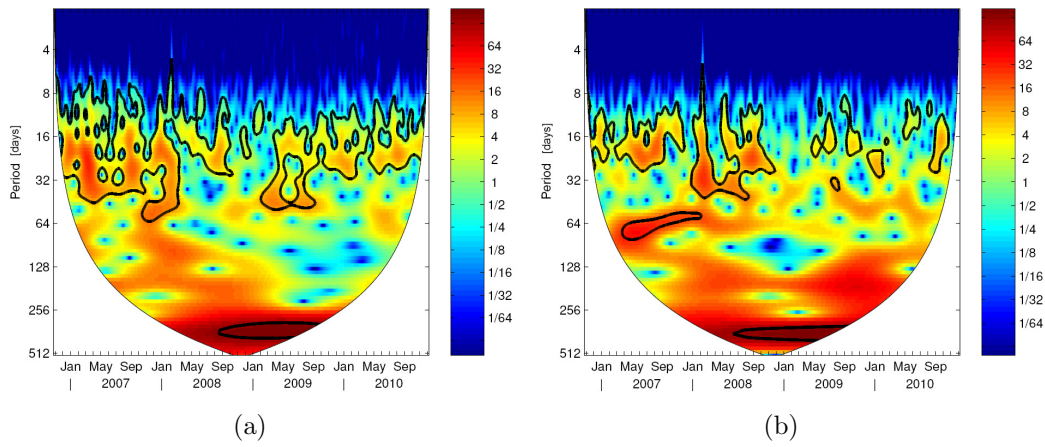
Figure 2.19: Continuous wavelet transformation of (a) the baroclinic and (b) the barotropic SSH anomaly at the position ANT 13. The contours show the power spectrum normalized by the variance. The black contour line indicates the 95% siginificance level.
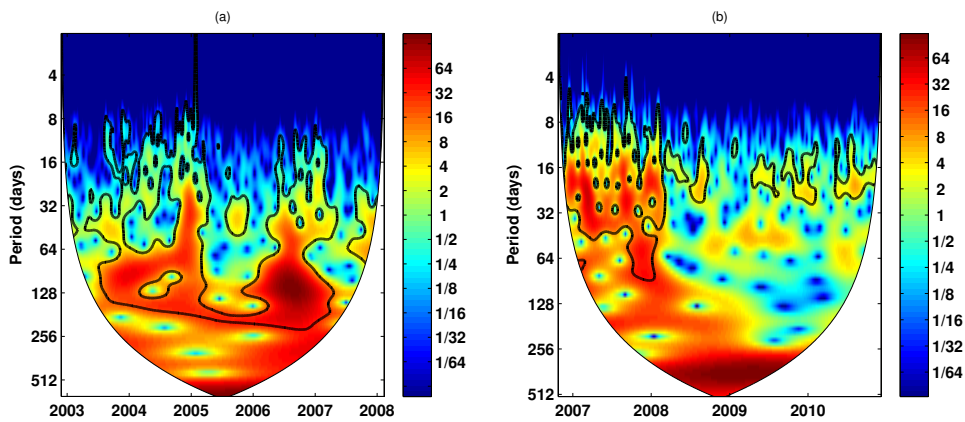
Figure 2.20: Continuous Wavelet Transformation (CWT) of baroclinic SSH anomalies relative to 1000 m at the positions (a) ANT 7 and (b) ANT 13. The contours show the power spectrum normalized by the variance. The black line indicates the 95% signifcance level.

2.3.4 Comparison with satellite altimetry

Figure 2.21 shows the SSH anomalies measured by the satellite altimeters on board Jason-1 and Jason-2 (blue, in the following denoted by Jason 1/2) and the total SSH anomalies η' derived from PIES. The data was downloaded from the OpenADB website (http://openadb.dgfi.badw.de/) provided by the German Geodetic Research Institute (Deutsches Geodätisches Forschungsinstitut, DGFI). The data is available along the satellite track and is provided with all atmospheric corrections (e.g. wet troposphere, inverse barometer effect, ... Schwatke et al., 2010). Furthermore barotropic waves have been removed using the model MOG2D (Carrère and Lyard, 2003).
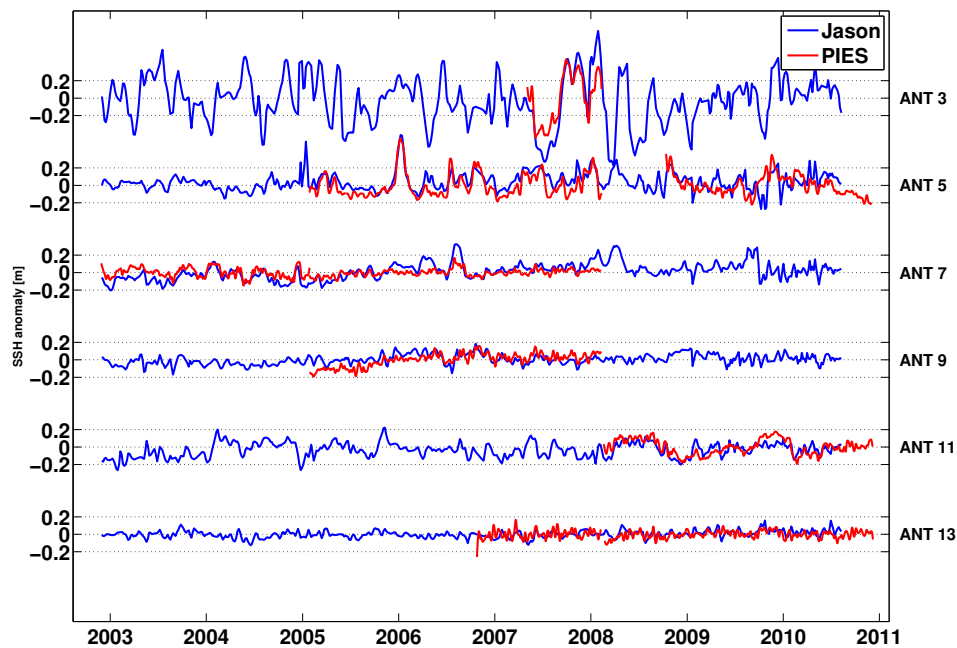
Figure 2.21: Sea surface height (SSH) anomaly for the different PIES positions from PIES data (red curves) and from satellite altimetry (blue curves).

Jason-1 and Jason-2 have a repeat cycle of 10 days, but due to the fact that the PIES had been deployed at cross-over points two measurements are available within the 10 day repeat cycle. The data have been interpolated and resampled at 5-day regular time intervals. The PIES derived SSH anomalies are furthermore compared to

the daily gridded ($1/3°$x $1/3°$) Aviso data produced by Ssalto/Duacs and distributed by Aviso, with support from CNES (http://www.aviso.oceanobs.com/duacs/).

Table 2.9 lists the correlation coefficients of the total (R), the baroclinic (R_{bc}) and the barotropic (R_{bt}) SSH anomalies derived from PIES with total SSH anomalies from satellite altimeters Jason 1/2. Furthermore the regression coefficients for the total and baroclinic SSH anomalies and the RMS error are listed.

Table 2.9: Correlations between PIES derived and altimetric monomission SSH anomalies from Jason 1/2. Correlation coefficients are derived for the total R, the baroclinic relative to 2000 dbar R_{bc} and the barotropic R_{bt} SSH anomalies. The regression coefficient was determined by a linear fit between altimetry and PIES derived SSH anomaly on the one hand for the total SSH anomaly and on the other hand for the baroclinic (bc) SSH anomaly. Furthermore the RMS error between the PIES derived total SSH anomaly and satellite altimetry was calculated.

PIES	R	R_{bc}	R_{bt}	Regression (total)	Regression (bc)	RMS error(cm)
ANT 3	0.92	0.96	0.51	0.58	0.44	22.2
ANT 5	0.68	0.67	0.23	0.77	0.69	9.6
ANT 7	0.59	0.67	0	0.29	0.3	7.7
ANT 9	0.66	0.63	0.41	0.61	0.38	4.7
ANT 11	0.66	0.70	0.38	0.82	0.62	7.0
ANT 13	0.24	0.08	0.22	0.25	0.06	5.6

The highest correlation coefficient between PIES and satellite altimetry is found at ANT 3. This PIES is the northern most one, recording the highest amplitudes. The lowest correlation coefficient (0.24) is found at the southern most position ANT 13. Generally, the correlation coefficient decreases with increasing southern latitude until ANT 9. The following positions ANT 9 and ANT 11 show a correlations of similar magnitude as observed at the position ANT 5.

The correlation coefficient between the SSH anomalies measured by altimetry and the baroclinic SSH anomalies derived from PIES is in some cases (ANT 3, ANT 7 and ANT 11) higher than the correlation between the total SSH anomalies of PIES and altimetry. By contrast, at the southern most position the correlation between altimetry and the baroclinic SSH anomalies is negligible.

The regression coefficient of the total SSH anomalies varies between 0.25 and 0.82. Total regression coefficients are higher than 0.58 except ANT 7 and ANT 13. The

highest value of 0.82 is found at the position ANT 11 which also shows a high cor-
relation coefficient compared to the adjacent positions. The regression coefficient
of the baroclinic SSH anomalies shows in principle the same characteristics as the
regression coefficient of the total SSH anomalies but values are smaller by 0.08 to
0.2. The RMS error decreased from 22.2 cm to 5.6 cm from north to south.

Table 2.10: Correlation and regression coefficient between PIES derived baroclinic
SSH anomalies R_{bc} relative to 1000 dbar and altimetric SSH anomaly
(Jason 1/2).

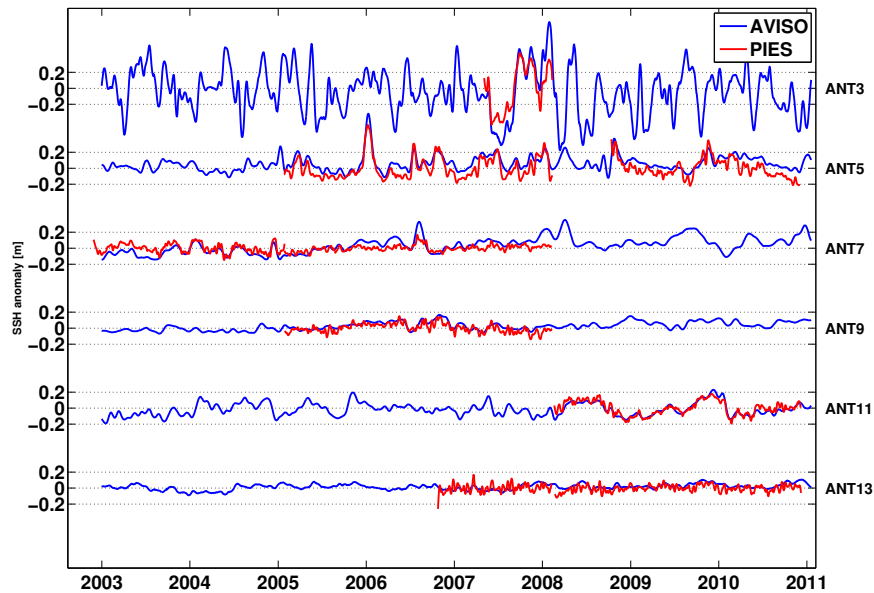| PIES	R_{bc}	Regression (bc)
ANT 3	0.93	0.39
ANT 5	0.69	0.38
ANT 7	0.74	0.36
ANT 9	0.61	0.38
ANT 11	0.69	0.7
ANT 13	0.05	0.02

Figure 2.22: Total SSH anomalies provided by Aviso (blue) and derived from PIES
(red).

Table 2.10 lists the correlation and regression coefficient between the baroclinic SSH anomalies relative to 1000 dbar derived between SSH anomalies from PIES and from Jason 1/2. This table is used for comparison with the study of Dhomps et al. (2011).

Table 2.11 lists the same parameters as Table 2.9 but for the comparison with the daily gridded (1/3°x 1/3°) Aviso product.

Table 2.11: Correlations between PIES derived and gridded Aviso SSH anomaly. Correlation coefficients are derived for the total R, the baroclinic relative to 2000 dbar R_{bc} and the barotropic R_{bt} SSH anomaly. The regression coefficient was determined by a linear fit between altimetry and PIES derived SSH anomalies on the one hand for the total SSH anomalies and on the other hand for the baroclinic (bc) SSH anomalies. Furthermore the RMS error between the PIES derived total SSH anomaly and satellite altimetry was calculated.

PIES	R	R_{bc}	R_{bt}	Regression (total)	Regression (bc)	RMS error(cm)
ANT 3	0.92	0.96	0.52	0.58	0.44	21.7
ANT 5	0.87	0.87	0.24	1.05	0.96	6.2
ANT 7	0.58	0.66	0.00	0.32	0.32	7.2
ANT 9	0.74	0.67	0.51	0.82	0.48	3.8
ANT 11	0.90	0.86	0.63	0.89	0.61	4.1
ANT 13	0.33	0.07	0.34	0.41	0.06	4.8

Except of ANT 3 the correlation and regression coefficients are increased compared to the along-track data from Jason 1/2 while the RMS error decreased. Figure 2.22 shows the total SSH anomalies provided by Aviso and derived from PIES. Compared to the Jason 1/2 product (Figure 2.21) the Aviso product looks much smoother due to the smoothing process. Figure 2.23 shows the comparison of the two data sets (Jason 1/2 and Aviso) depicted as a Taylor Diagram (Taylor, 2001). It is seen that the standard deviation of Aviso and Jason 1/2 at ANT 7 and ANT 5 is twice respectively 1.5 times as high as the standard deviation measured from PIES. This underlay the visual impression of Figure 2.22 which show higher amplitudes of the Aviso data at ANT 3 and ANT 5 compared to the PIES measurements. For all other positions the ratio of standard deviations is close to one or slightly below one. For all positions except ANT 7 and ANT 13 the ratio of RMS error and standard deviation of the PIES measurement is below one.
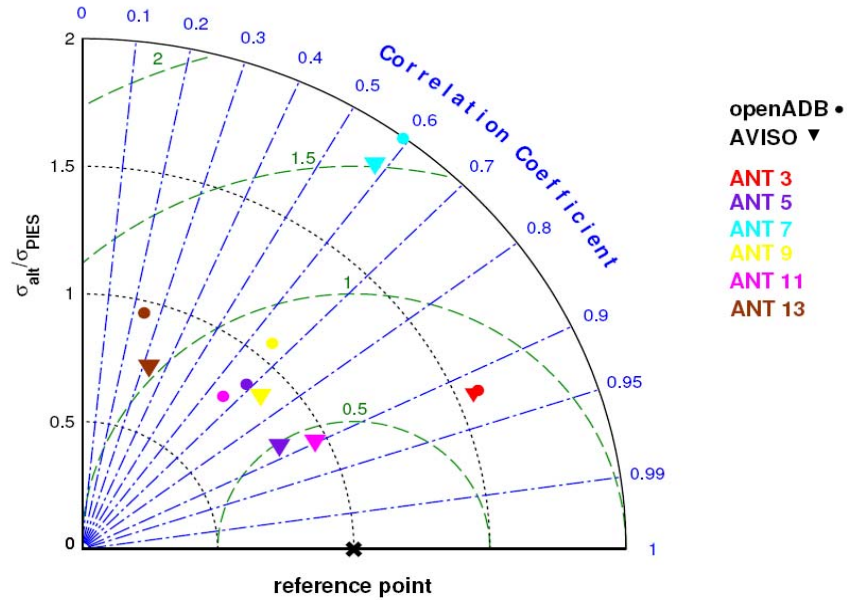
Figure 2.23: Taylor diagram for the comparison of agreement of total SSH anomaly derived from PIES, measured by Jason 1/2 (dots) and the daily gridded SSH anomalies provided by Aviso (triangles). The colors indicate the different positions of the PIES. The green circles indicate the ratio of the RMS error and the standard deviation of the total SSH anomaly derived from PIES. The reference point marks the perfect agreement with PIES observations.

2.3.5 Geostrophic transport

Figure 2.24 shows the geostrophic transports derived between the different PIES positions. The transport between two positions varies between ≈ 20 Sv for ANT 5-7 and ≈ 100 Sv for ANT 9-13. The transport is linear dependent of the distance between the stations and the integral over the density gradient (Eq. 2.18). Because of the different station spacing it is not possible to state between which PIES the most transport occurs. Table 2.12 lists the mean values, standard deviations and error estimate of the geostrophic transports between the individual positions as shown in Figure 2.24. The error estimate is done by propagating the RMS of the lookup table into the transport calculation. This error is interpreted as the uncertainty of the mean ACC transport.
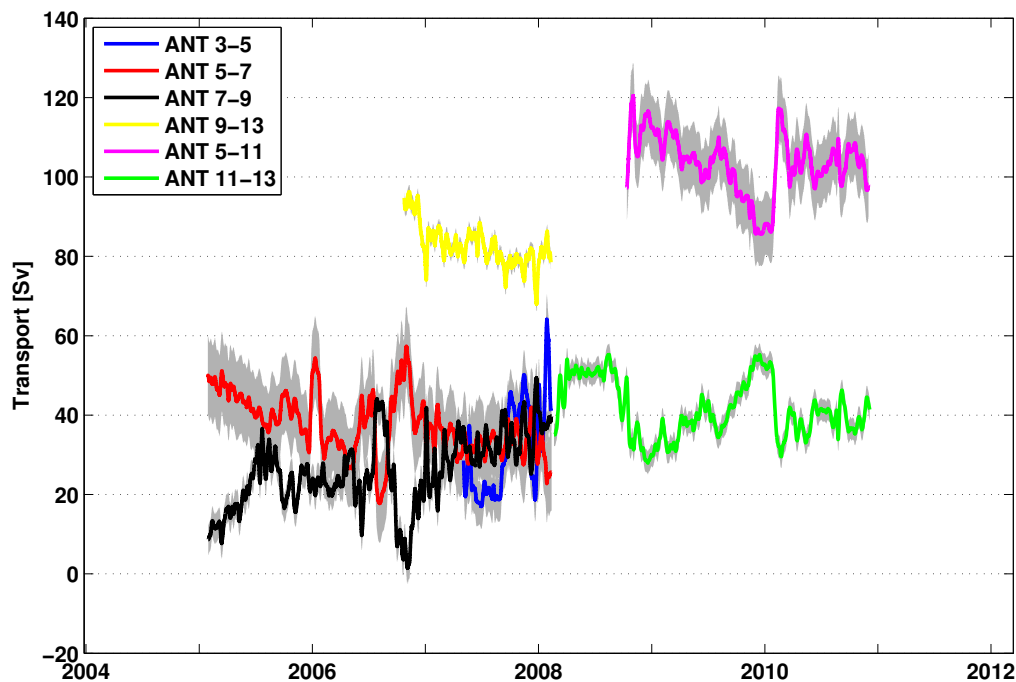

Figure 2.24: Transport between the different PIES positions and with an error estimation (gray shaded area).

The transport of the Antarctic Circumpolar Current (ACC) is defined between the Subtropical Front (STF) and the southern ACC Front. Figure 2.13 shows that

the PIES ANT 5 is closest to the STF but it also covers several Agulhas rings. The
ACC transport is derived as the sum of the transports between ANT 5 - ANT 7,
ANT 7 - ANT 9 and ANT 9 - ANT 13 respectively as sum of the transports between
ANT 5 - ANT 11 and ANT 11 - ANT 13 for the second deployment period.

Table 2.12: Mean, standard deviation (std) and error of geostrophic transport de-
rived between the PIES positions (see Figure 2.24)

transport between position ANT	mean [Sv]	std [Sv]	error [Sv]
3-5	31.6	11.9	5.6
5-7	37.1	7.5	9.9
7-9	25.6	9.0	3.7
9-13	82.7	5.0	1.7
5-11_2	103.4	7.5	8.0
11-13	41.6	7.1	2.8

Figure 2.25 shows the cumulated ACC transports defined between ANT 5 and
ANT 13. It reaches a mean and standard deviation of 147.2±2.4 Sv at the first
deployment period (2007-2008) and a slightly lower mean and standard deviation
of 142.8±1.9 Sv during the second deployment period (2008-2010). The error esti-
mate is derived from the RMS error (see Table 2.12) of the lookup table propagated
through the transport calculation. The error of the mean ACC transport of the first
deployment period is derived as sum over three transport errors (ANT 5-ANT 7,
ANT 7-ANT 9, and ANT 9-ANT 13) and results 15.3 Sv. For the second period only
two errors are summed (ANT 5-ANT 11_2 and ANT 11_2-ANT 13) which result a
slightly lower error of 10.8 Sv for the mean of the ACC transport. The larger error
of the first deployment period is caused by the relatively large error of the transport
between ANT 5 and ANT 7 and the summation of three errors instead of two for
the second deployment period.
For the first deployment period direct CTD measurements are only available for the
positions ANT 7, ANT 9 and ANT 13 and were taken during the cruise ANT XXIV-
3 (Rohardt, 2009a). They are used for transport calculation and are compared to
the PIES derived transport. The CTD derived transport is about 10 Sv higher than
the PIES derived transport. The transport between ANT 7 and ANT 13 has a pos-

itive trend which is compensated by the addition of the transport between ANT 5 and ANT 7 which shows a negative trend. Therefor the cumulated ACC transport shows no long term trend.
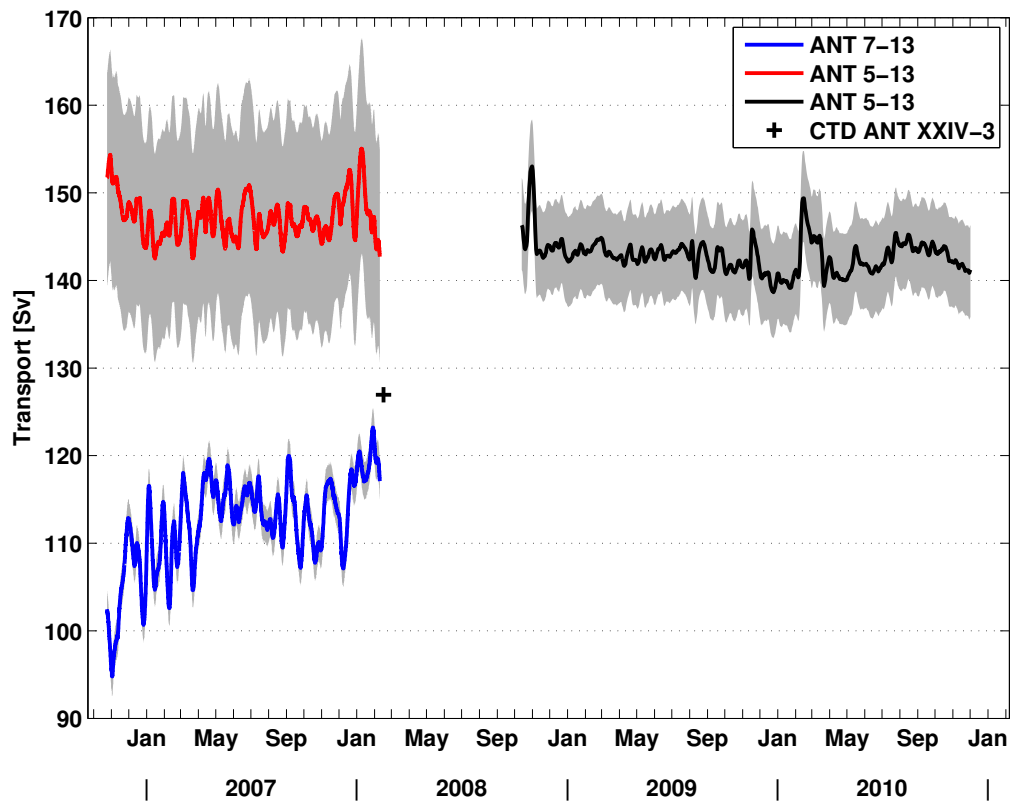

Figure 2.25: Cumulated transport between ANT 7 and ANT 13 (blue) and ANT 5 and ANT 13 (red/black) and the transport derived from CTD cast (black cross) between the positions ANT 7 and ANT 13. The gray shaded area indicates the cumulated error estimates of the transports.

2.3.6 Comparison with the Southern Ocean State Estimate (SOSE)

The Southern Ocean State Estimate (SOSE) is derived from an eddy-permitting general ocean circulation Model based on the $1/6°$ horizontal resolution version of the MITgcm (Massachusetts Institute of Technology global circulation model). Furthermore the ECCO Global Ocean Data Assimilation (ECCO-GODAE) approach was used to include meteorological and oceanographic observations. For further details about the model see Mazloff et al. (2010). For the comparison the iteration 59 of SOSE was used, which can be downloaded from http://sose.ucsd.edu/. The iteration runs from 1 Jan. 2005 to 31 Oct. 2009 with optimization carried out for the years 2005 to 2007. The time period from 1 Jan. 2008 to 31 Oct. 2009 is unconstrained. The potential temperature and salinity data used for direct comparison and the calculation of the acoustic travel time was provided as five day averaged state.
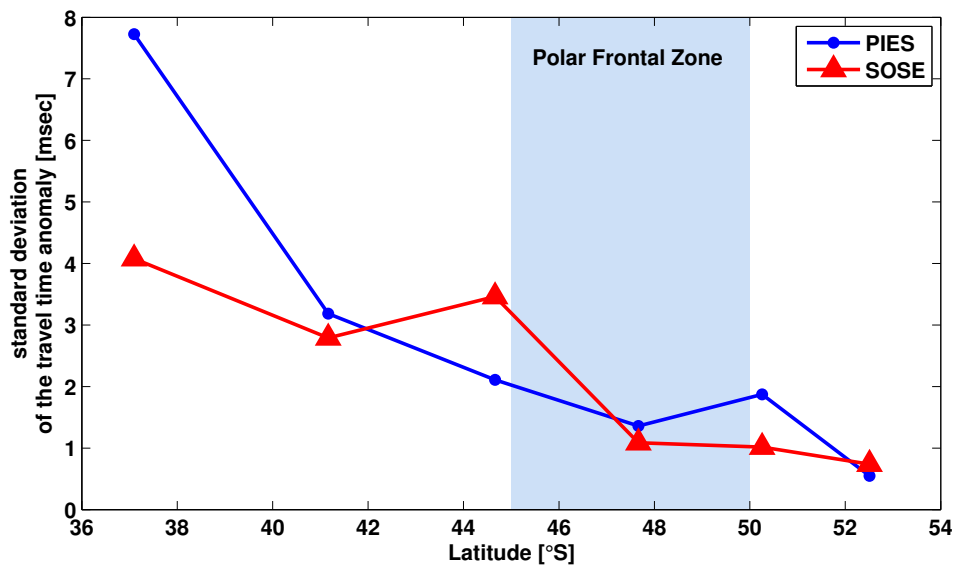

Figure 2.26: Standard deviation of the acoustic travel time anomaly for PIES (blue) and SOSE (red). The Polar Frontal Zone is indicated as blue shaded area.

To get a first impression how good SOSE performs at the Good Hope Line the

standard deviation of the acoustic travel time anomaly was calculated. The acoustic travel time is an integral quantity and represents the density structure of the water column, which is directly measured by the PIES. Figure 2.26 shows the standard deviation of the acoustic travel time for PIES and SOSE calculated over the same time period. The blue shaded area in Figure 2.26 indicates the mean position of the Polar Frontal Zone which is defined between the Subantarctic (SAF) and the Polar Front (PF). Following Lutjeharms (1985) the mean position of the SAF is at about 45°S and the PF is at about 50°S.

SOSE gets the overall structure very well although it underestimates the variability in the Agulhas region, which is not surprising because of the high eddy activity in this region. In the Polar Frontal Zone SOSE overestimates the variability at the SAF and underestimates it at the PF. This was seen in a similar way by Chereskin et al. (2012) in Drake Passage.

Figure 2.27 and 2.28 show the difference between SOSE and the PIES derived potential temperature and salinity. At the position ANT 3 and ANT 5 it is obvious that SOSE does not represent the passing of Agulhas rings correctly. Hence the difference in potential temperature and salinity is positive at these locations. At the position ANT 7 the differences are mostly negative and coincide with the presence of cold core eddies transported with the South Atlantic Drift. The positions further south show less variable differences. Layered differences are seen at position ANT 13.
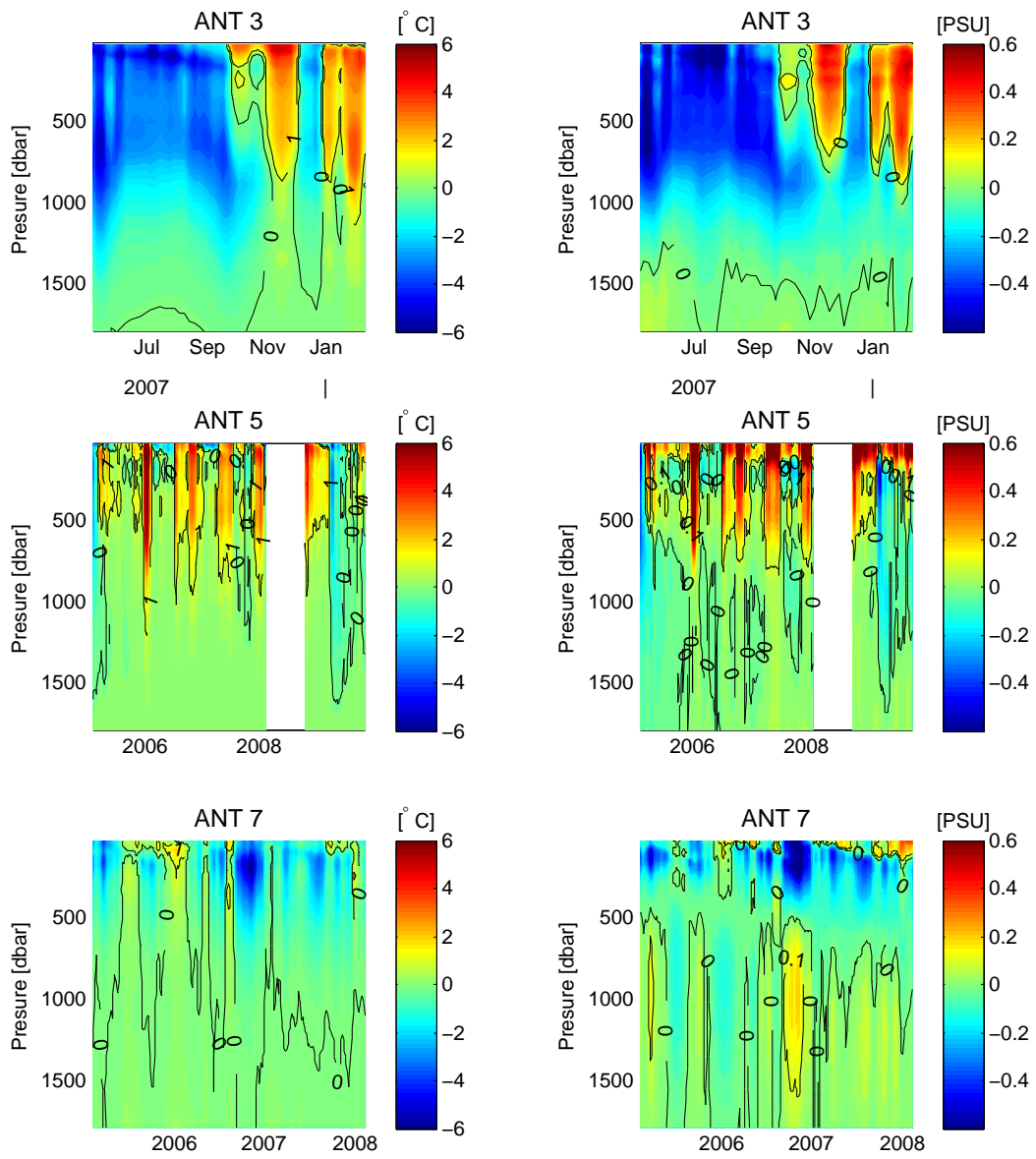
Figure 2.27: Difference between the PIES derived potential temperature and salinity field and SOSE at the PIES positions.
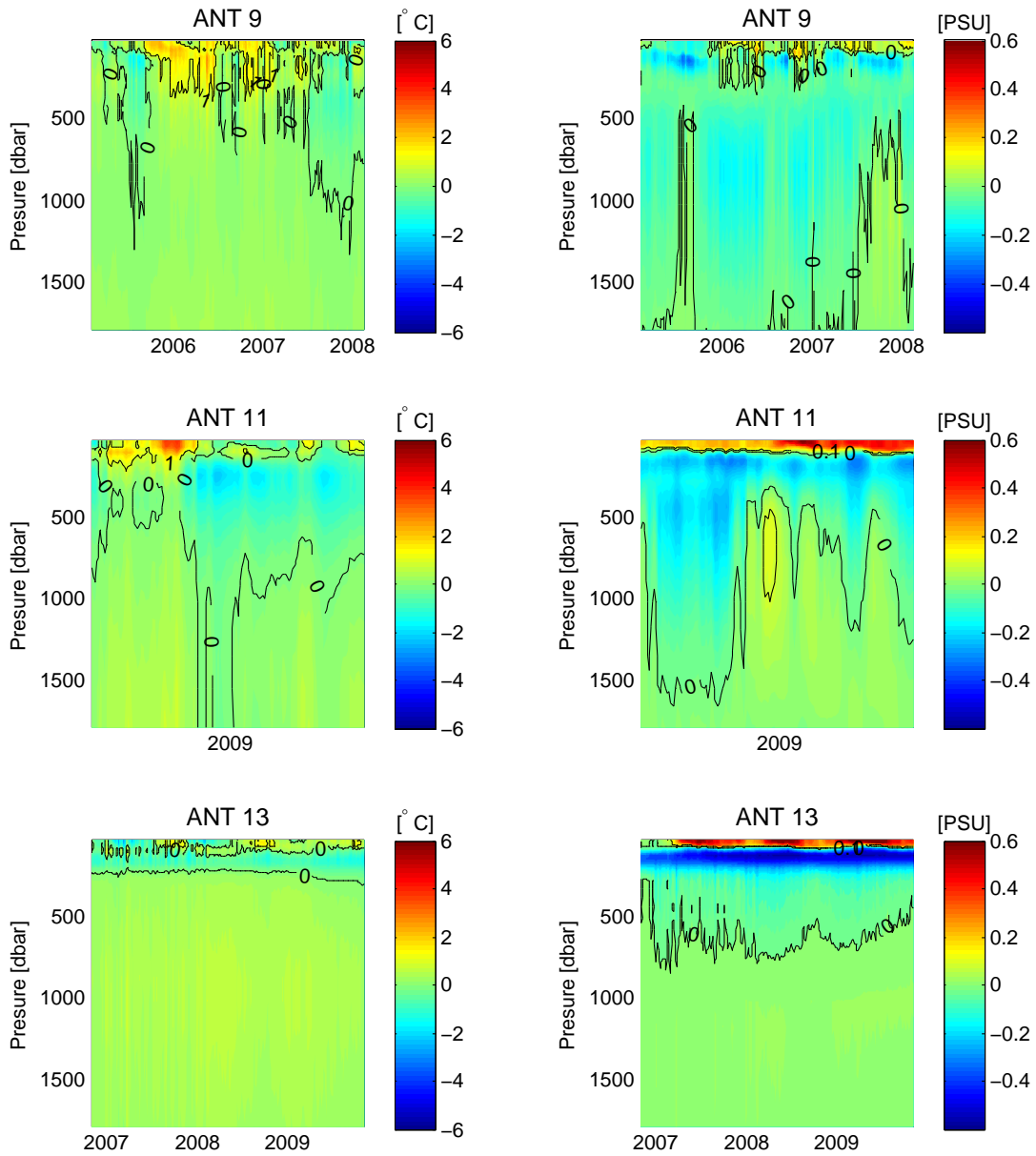
Figure 2.28: Difference between the PIES derived potential temperature and salinity field and SOSE at the PIES positions.
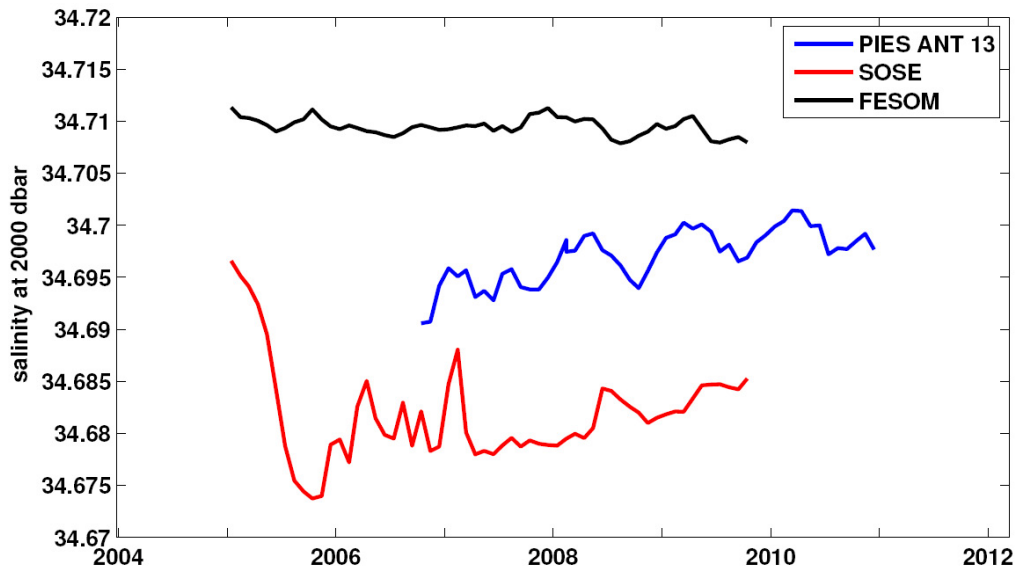
Figure 2.29: Salinity at the position ANT 13 in at a pressure of 2000 dbar from the
            PIES (blue), SOSE (red) and the Finite Element Sea Ice Ocean Model
            (FESOM).

Figure 2.29 shows the monthly salinity at the 2000 dbar level for the PIES ANT 13,
SOSE and the Finite Element Sea Ice Ocean Model (Timmermann et al., 2009,
FESOM). ANT 13 and SOSE show a salinification trend of 0.0001 PSU/month
while the trend is absent in FESOM. The SOSE run seams to need the first half of
the year 2005 to adjust to the optimization before it shows a trend as measured at
ANT 13. Furthmore the salinity time series of ANT 13 shows a seasonal cycle wich
is consistent with the seasonal cycle of the PF (Dong et al., 2006). This seasonal
cycle is not observed in the SOSE results but in the FESOM results. FESOM has
a weak seasonal cycle between 2008 and 2009 which is coherent with the observed
seasonal cycle.

The increase in temperature and salinity is consistent with a southward shift of the
PF (Figure 2.30).

Figure 2.30: Position of the STF (blue), SAF (red) and the PF (red) crossing the Good Hope line derived from SOSE.

The latitudes (along the Good Hope line) of the three major fronts in Figure 2.30 are derived from the SOSE temperature and salinity field using the criteria of Orsi et al. (1994) and Park et al. (1993). For the years 2005 to 2007 the position of the PF front has a mean Latitude of 50.84°S with a standard deviation of 0.44°. During this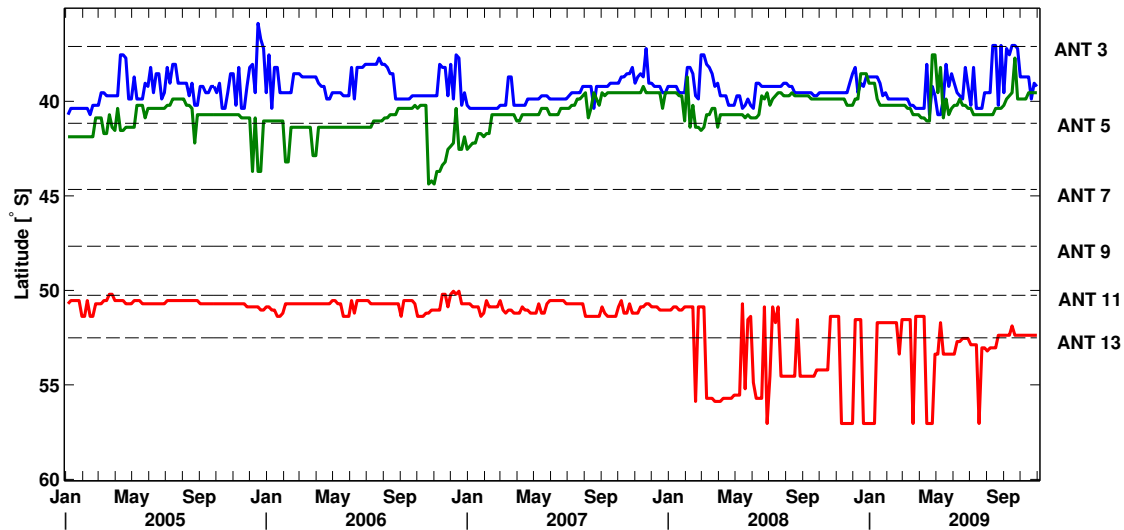 years the run was optimized by the assimilation of in-situ data such as CTD or satellite altimetry. A small trend (-0.15°/year) is visible for the PF position during the period of optimization (2005-2007). The run without optimization (2008-2009) shows a much more variable position of the PF which is centered farther south. This seems to be a model error which is not so pronounced for the other two fronts. The STF has its mean position at 39.27 °S with a standard deviation of 0.85°. The SAF has a even higher standard deviation (1.02°) and is centered at 40.92°S. Until 2008 the two fronts (STF and SAF) are clearly separated which is not the case for the years 2008 and 2009. In summary the optimized run from 2005 to 2007 looks reasonable with regard of the front positions. Without optimization the front positions are not reasonable especially the large variability of the PF is unrealistic. The SOSE data was provided by Matthew Mazloff and is continuously improved by him. All unrealistic features were reported to Matthew and will be considered and hopefully improved in the upcoming versions.

Looking at the spatial distribution of salinity and potential density relative to 2000 dbar (Figure 2.31) a southward shift of the low saline and dense water became obvious. This shift is seen between between 10°W and the prime meridian.

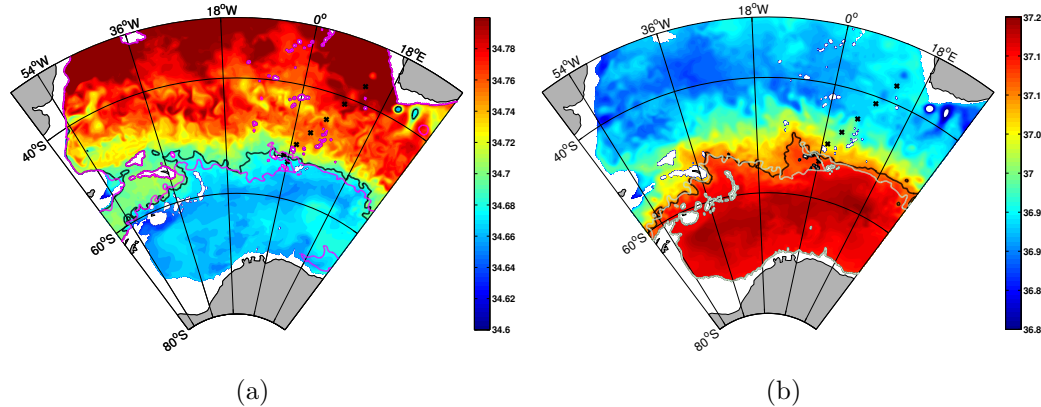(a)   (b)

Figure 2.31: The contours in (a) show the salinity distribution at 2048 dbar in January 2005 where the black the 34.69 isohaline in January 2005 is the black contour line and the same isohaline in October 2009 is depicted as magenta contour line. The contours in (b) show the potential density (σ_2) distribution at the same depth in January 2005. The black contour line is the 37.11 isopycnal in January 2005 while the magenta contour line shows the same isopycnal in October 2009.

The atmospheric circulation is dominated by the Antarctic Oscillation (AAO) which is the leading mode (first EOF) of the surface pressure field between mid and high latitudes (Gong and Wang, 1999). Because of it's zonal symmetry or 'annular' structure the AAO is often called Southern Annular Mode (SAM) (Thompson and Wallace, 1999). The index to characterize the SAM is derived as the zonal mean difference between the sea level pressure at 40°S and 65°S. The SAM index used for the following investigations was derived by Nan and Li (2003). Correlating the monthly mean salinity profiles of SOSE at the position ANT 13 (October 2005 till October 2009) with the monthly SAM index (Figure 2.32 blue line) shows negative correlations (-0.27) in the upper 100 dbar. Below 100 dbar the correlation rises to 0.24 at 177 dbar before it gets again negative until 1000 dbar. At 1000 dbar it gets positive again and reaches a maximum of 0.18 at 2000 dbar.

To investigate if the observed trend in deep salinity is connected to the SAM the

trend is removed from the salinity time series. Thereafter the correlation with the SAM index, which still contains a trend is derived again (Figure 2.32 red line). It can be seen that the correlation below 1000 dbar is significantly decreased compared to the salinity profiles with trend in deep salinity.
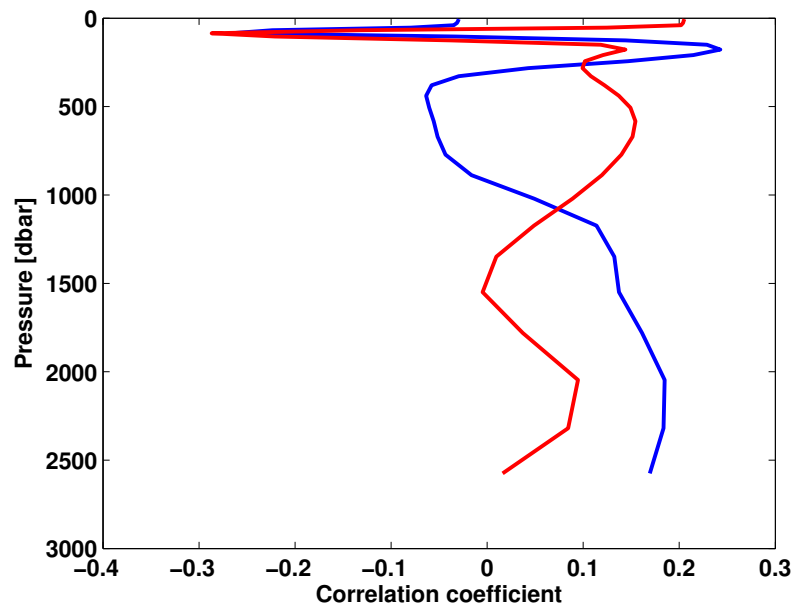

Figure 2.32: Correlation coefficient between the SAM index and the salinity profiles from SOSE (October 2005 till October 2009) are derived on the one hand with the trend seen in deep salinity (blue) and on the other hand with detrended salinity profiles (red).

2.4 Discussion

2.4.1 SSH anomalies and their comparison with satellite altimetry

The PIES array across the ACC enabled us to investigate the baroclinic and barotropic
contributions of the total SSH anomalies (Table 2.8). Furthermore, a direct compari-
son with altimetry was performed to investigate if the addition of the barotropic com-
ponent significantly increases the correlation between PIES's derived SSH anomalies
and altimetry. The comparison was done for two different altimetry data sets on
the one hand for the along-track data of Jason 1/2 received from the OpenADB
data base (Table 2.9)and on the other hand for the daily gridded (1/3°x1/3°) Aviso
product (Table 2.11).
Baker-Yeboah et al. (2009) ascertain that the barotropic component accounts for
20% of the total SSH variability while during extreme events this contribution
reaches 47%. In contrast this study found barotropic components of up to 60%
farther south in the ACC. The increase of the barotropic component is observed
south of the position ANT 7 and is only interrupted at the position ANT 11. This
might be due to the fact that the ACC is organised in jets along the two major fronts
(Polar Front [PF] and Subantarctic Front [SAF], e.g. Sokolov and Rintoul (2006)).
The fronts are characterized by step-like density gradients (Orsi et al., 1994). Hence
high baroclinic signals are expected across the fronts. Applying the frontal criteria
of Orsi et al. (1994) to the lookup table it is possible to assign a travel time to the
individual fronts (black lines Figure 2.6). Using these travel time criteria it becomes
obvious that the PIES ANT 11 is in the vicinity of the Polar Front (PF) which
explains the high baroclinic component at this position. In between the fronts the
regime is highly barotropic.
The reference level used to calculate the baroclinic SSH anomalies has a big influence
on the assignment of the contribution of baroclinic and barotropic SSH anomalies,
especially in regions of low stratification (Dhomps et al., 2011) such as the regions
between the ACC fronts. Dhomps et al. (2011) used a reference level of 1000 dbar
whereas this study used 2000 dbar. Except of ANT 7 the baroclinic component
increases with deepening the reference level (Table 2.8) which means that baroclinic

variability is missing when using the shallower reference level. The strongest impact is seen at the position ANT 13 were the baroclinic component decreases from 40% to 13%. A decrease of similar magnitude is observed at the position ANT 5 indicating that the passing Agulhas rings responsible for most of the baroclinic variability have a pronounced deep baroclinic component. Furthermore the correlation coefficient between PIES derived and altimetric total SSH anomalies are slightly increased by 0.1 using the deeper reference level. By contrast, the regression coefficient of the baroclinic component is significantly improved (up to 0.33) at some positions by deepening the reference level. This suggests that mainly the amplitude of the SSH anomalies is affected by a deeper reference level. An exception of this general tendency is found at the position ANT 7, where the correlation and regression coefficients at the shallower reference level are higher. ANT 7 is in the vicinity of the South Atlantic Drift which is a region of cross frontal mixing of Subantarctic and Antarctic Intermediate Water (AAIW) with subtropical waters (Boebel et al., 2003). This mixing process is probably the reason for the poorly captured variance of the salinity lookup table below 600 m as noticed in section 2.2.1.2. Hence the decrease of the correlation and regression coefficient by deepening the reference level is caused by the inability of the lookup table to represent the mixing process between AAIW and adjacent water masses like (e.g. NADW). This conclusion is supported by a comparison of independent CTD data (not used for the lookup table) which shows the largest salinity differences below 600 dbar between 42° and 44°S whereas the temperature difference is very small. Generally, the correlation coefficients found between PIES derived baroclinic SSH anomalies (relative to 1000 dbar, Table 2.10) and Jason 1/2 observations are in the same order as found by Dhomps et al. (2011) but with lower regression coefficients except of the position ANT 11.

At the northern edge of the ACC (ANT 7), semi-annual baroclinic variations were the most prominent signals in CWT analysis, while monthly variations are also barotropic (see Figure 2.18). The CWT at position ANT 13 (Figure 2.19) shows the most prominent signal on annual and monthly time scales. The results of the CWT analysis are consistent with the findings of Vinogradova et al. (2007) who investigated the relation between SSH and bottom pressure using the MIT general circulation model. The time series are too short to investigate inter annual variability, a problem which might be overcome in the future by extending the time series with new data. The CWT showed that the significant time scales of baroclinic and

barotropic SSH anomalies vary with time and space. Hence the partitioning of baro-
clinic and barotropic SSH anomalies also changes with time and space

The correlation coefficient of the total SSH anomalies observed by PIES vs. Altime-
try decreases from north to south from 0.92 to only 0.24 for the Jason 1/2 product
from OpenADB (Table 2.9). This trend is interrupted at the positions ANT 9 and
ANT 11. The position ANT 11 shows a high baroclinic component compared to
the adjacent positions (Table 2.8) and is close to the SAF (see Figure 2.2 and Fig-
ure 2.13). Interestingly the correlation of the baroclinic part is higher than the
correlation with the total SSH anomalies at four positions out of six (Table 2.9).
This is unexpected because the satellite altimeter measures the total SSH anoma-
lies, and hence the correlation of the total SSH anomalies should be higher than the
correlation with only the baroclinic part (see Baker-Yeboah et al., 2009). It pos-
sibly indicates a more fundamental problem and could be caused by uncertainties
in the correction of altimeter data and the small amplitude of the signal south of
the Subantarctic Front which is close to the uncertainty of the method presented
here (4.53 cm, Table 2.7). That the correction of satellite altimetry plays a major
role can be seen when computing the correlation coefficients between along-track
Aviso data (not shown) and PIES. These correlations are higher compared to the
correlations with OpenADB but also lower than the correlations with the gridded
Aviso product (compare Table 2.9 with Table 2.11).

Oceanic tide corrections are applied to both satellite altimetry and ocean bottom
pressure in the same way but different filtering methods are applied to remove
barotropic waves. For processing the PIES data a 100 hour low pass filter is used to
remove barotropic waves whereas for the Jason 1/2 data the MOG2D model (Carrère
and Lyard, 2003) was used. This probably causes differences in the barotropic com-
ponents which are essential in the ACC region. Aliasing effects might be another
reason for the poor correlation coefficient in the ACC region because variability is
reduced by smoothing and filtering the data as reported by Byrne and McClean
(2008).

Figure 2.23 indicates that the PIES derived SSH anomaly is in better agreement
with the smoothed Avsio product than the along-track product from OpenADB.
The correlation coefficients range from 0.33 to 0.92 and are higher than 0.6 at all
positions except ANT 13. In contrast in four (ANT 5,9,11 and 13) out of six cases
the Aviso product misses variability compared to the PIES derived SSH anomalies

(see Figure 2.23). The gridded product correlates better with the PIES measurements than the Jason 1/2 product and has a lower the RMS errors. This might be caused by the uncertainties of the altimetry measurements which are close to the amplitude of the signal in this region. The uncertainty of the satellite signal depends on many factors e.g. instrument errors or background model errors. The formal accuracy is below 1 cm in the open ocean but might be much larger in the polar regions (personnel communication Roman Savcenko). Gridding the data smooths up variability but also errors which otherwise lead to smaller correlation coefficients. Gridded Aviso data shows better agreement with the PIES because of small scale variability which is hard to distinguish from noise in the Southern Ocean. Hence gridded Aviso SSH anomalies seem to be more suitable for assimilation approaches in the Southern Ocean because models are also not able to reproduce the small scale variability correctly.

Our results show that the barotropic SSH component plays an important role in the Southern Ocean. But the contribution of the barotropic part is not monotonously increasing from north to south. It is interrupted by regions of low barotropic variability associated with the oceanic fronts. Hence the partitioning into baroclinic and barotropic SSH anomalies varies in time and space. This should be taken into account when assimilating SSH anomalies into ocean models. Unfortunately the position and movement of oceanic fronts are not well captured in ocean models (e.g. ORCA2 Ferry et al., 2007), hence this should be improved first before deriving the partitioning of the SSH anomalies as done by Ferry et al. (2007).

2.4.2 Baroclinic ACC transport

There have been several attempts to measure the baroclinic ACC transport. The most obvious place for this is to measure the transport across Drake Passage because the ACC has to pass this bottleneck. At all other places the determination of the ACC boundaries becomes a problem, which has to be solved. The ACC transport is determined by hydrographic sections while the variability is estimated from the repetition of these sections. This method causes the problem that variability might be missed through the coarse time spacing and seasonal variability can not be fully assessed because there are only a few expeditions in austral winter available.
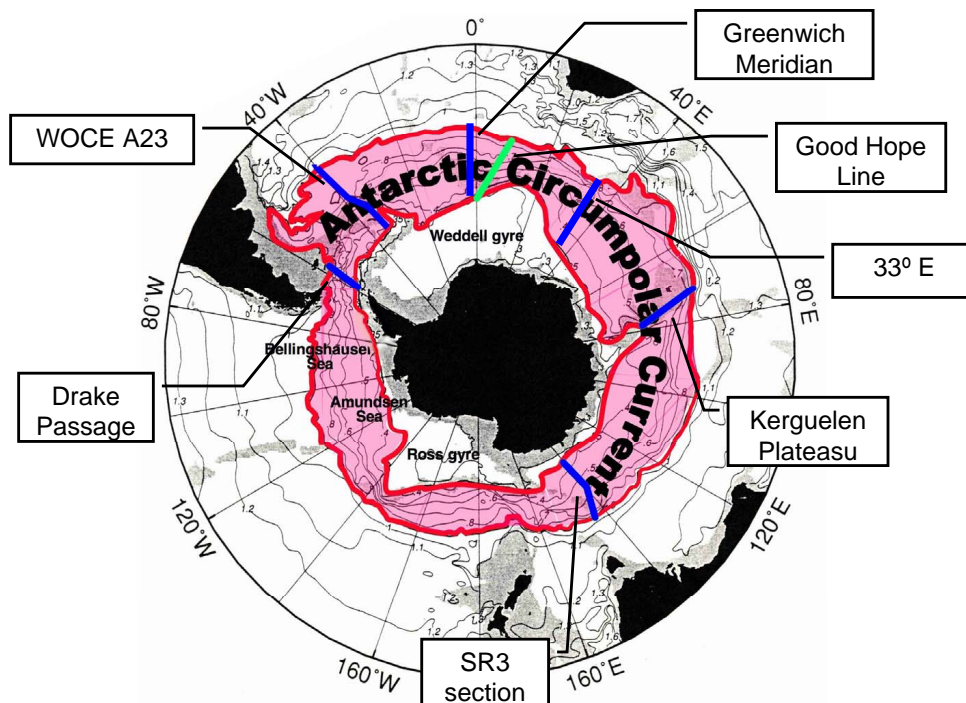

Figure 2.33: Sections across the ACC at which the geostrophic transport was measured. Values are listed in Table 2.13

Table 2.13 lists some results of baroclinic ACC transport measured around the globe across the sections shown in Figure 2.33. A direct comparison is possible with the estimate of Gladyshev et al. (2008), who also took observations along the Good Hope line. Gladyshev et al. (2008) derived a transport which is slightly

Table 2.13: Baroclinic ACC transport estimates determined at different cross section.

Section	Baroclinic Transport [Sv]	Reference
Drake Passage	124±15	Whitworth III et al. (1982)
Drake Passage	136±7.8	Cunningham et al. (2003)
SR3	141.7	Heywood and King (2002)
Greenwich Meridian	162	Whitworth III and Nolin Jr. (1987)
Good Hope	136	Gladyshev et al. (2008)
33°E	138	Read and Pollard (1993)
Kerguelen Plateau	147-152	Park et al. (2009)
SR3	147±10	Rintoul and Sokolov (2001)

lower (136 Sv) compared to the PIES derived transport (147-142 Sv). Regarding the uncertainties of the GEM method (10-15 Sv) the results compare well. The difference might be due to numerous reasons. First of all the PIES are moored devices and can not be shifted according to the frontal positions. Hence the definition used to calculate the ACC transport (between STF and PF) is transformed into a rigid spatial definition (between ANT 5 and ANT 13). The size of this error is hard to estimate. But due to the fact that the two fronts which are associated with the major ACC transport (SAF and PF) are always located within the PIES array (ANT 5-ANT 13), it can be assumed that most of the transport and transport variability is captured by this method. Another error arises from the lookup table uncertainties which are quantified as errors in Table 2.12. Furthermore the method of using bottom triangles causes some error because a triangle is often not an appropriate simplification of rough bottom topography. As the error introduced by the constant PIES positions the error related to the bottom triangles is hard to quantify, but is assumed to be small due to the small temperature and salinity variability at those depths. In contrast to the other two error sources the error from bottom triangles is also known for CTD derived transports. Most studies (e.g. Read and Pollard, 1993; Cunningham et al., 2003; Heywood and King, 2002) calculate the baroclinic transport relative to the deepest common level of a station pair which is appropriate regarding finer station spacing (30-60 sm) used during the CTD surveys. The distance between the PIES is about 10 times larger (200-400 sm) than the normal CTD station spacing and hence using the deepest common level between two PIES as reference level would cause larger errors than using the bottom triangle

method.

Swart et al. (2008) also used the GEM method to derive baroclinic ACC transport above 2500 dbar from satellite altimetry across the Good Hope line. They calculated an ACC transport of 84.7 ± 3.0 Sv. The variability of 3 Sv is comparable to the variability derived in this study (2.4/1.9 Sv). Swart et al. (2008) as well as this study find no significant trend in the ACC transport across the Good Hope line.

2.4.3 Comparison with SOSE

The Southern Ocean State Estimate is an approach to optimize an eddy permitting model in the Southern Ocean. Acoustic travel time is a depth integrated property which represents the temperature and salinity structure. The acoustic travel time is directly measured by PIES and can be easily derived from SOSE, hence it is a good starting point for a general comparison of the model assessment. The comparison between the standard deviation of the acoustic travel time anomalies measured by PIES and derived from SOSE shows a good overall agreement. The standard deviation is underestimated by SOSE at the northern most position due to the fact that SOSE is only eddy permitting and not eddy resolving. An eddy permitting model has a resolution in the order of the Rossby radius but does not have enough resolution to investigate the eddies. Hence the Agulhas rings passing this position are not well captured and reduce the standard deviation of SOSE. The standard deviation of the SAF is overestimated while it is underestimated at the PF. The ACC variability is dominated by large meandering fronts and high eddy activity. SOSE was not attempted to fit to individual eddies and hence the misfit especially with sea surface height from satellite altimetry is largest in this region (≈ 30 cm). This might be an explanation of the large discrepancy between the SOSE derived and the PIES observed of the standard deviations of the acoustic travel times anomalies.

The major differences in temperature and salinity occur during eddy events. The position with the highest difference in the anomaly of the standard deviation of the acoustic travel time is position ANT 7. At this position the temperature and salinity differences are mostly negative especially in the upper 500 dbar. The structure of the differences is highly variable and deep reaching, which suggests that the eddy field at this position is not well captured.

At the southern most position a positive trend in salinity is found in the PIES obser-

vations, which is well represented by SOSE. A comparison with the non assimilating model FESOM shows no such trend suggesting that the assimilation improves the model substantially. But SOSE does not capture the seasonal cycle seen in the observed salinity. FESOM does capture the seasonal cycle in the years 2008 and 2009 but with lower amplitude. The trend in salinity might be caused by a frontal shift. Böning et al. (2008b) observed a warming and salinification at the southern flank of the ACC. They explain this trend with a strengthening of the westerlies and a southward shift of the mean position of the ACC. The strengthening of the westerlies is represented by a positive trend in the SAM index. Thompson et al. (1999a) analyzed a 30 year time series of SAM indices and found a significant (exceeding the 90% confidence level) linear trend for the months January, March, April, May, October and December. The largest trend was found in May. Furthermore Böning et al. (2008b) found a trend in salinity and temperature by analysing the data from the Argo float network and historical CTD data which is correlated with the SAM. The correlation between salinity derived from SOSE at the position ANT 13 and the SAM index is low (0.2) and decreases significantly when the trend is removed. This suggests that the trend is due to a trend in SAM. The time series is not long enough to investigate if the trend occurs mainly in the summer months.

2.5 Conclusions

In conclusion the PIES are a very helpful tool to investigate baroclinic and barotropic motion in the ocean. In regions were a unique relation between temperature/salinity profiles is found PIES provide a comparably cheap way to obtain longterm proxies for temperature and salinity. With the help of the bottom pressure sensor it is possible to derive total SSH anomalies and investigate their composition of baroclinic and barotropic SSH anomalies. This improves the understanding of the composition of the total SSH anomaly. Especially in the ACC region this knowledge could lead to improved assimilation schemes for SSH anomaly and hence improve the ocean models, which have substantial problems in this region.

Furthermore the PIES can be used to monitor the baroclinic ACC transport. They allow a long term survey of the mean transport and it's variability. These results can be further used to investigate trends and changes in the variability. The transport derived in this study shows no significant trend or changes in variability. The mean ACC transport compares well with historical transports observed around Antarctica.

The Southern Ocean State Estimate is a promising attempt to model the Southern Ocean. The comparison with PIES observations shows a good overall agreement especially regarding the trend in salinity. A correlation with the Southern Annular Mode Index suggests a relation between the salinity trend and the SAM. Climate models suggest that the positive trend observed in the SAM index is due to anthropogenic climate change. Hence the salinity trend could also be due to climate change and SOSE seems to be a good tool to investigate the impact of climate change in the Southern Ocean.

3 Improving a joint inversion of GRACE, GPS and modeled OBP by using Bottom Pressure Recorders (BPRs)

3.1 Introduction

This chapter focus on another possible application of the PIES. Their bottom pressure measurements are used together with other bottom pressure recorders (BPR) to quantify the mass budget of the ocean. The ocean circulations is the major source of mass redistribution and spatial variability. Changes in the total ocean mass occur due to changes and seasonal cycles in the river runoff, precipitation/evaporation or the ice sheets. In total these changes are called hydrological cycle and an accurate knowledge of the ocean mass budget is essential for it's quantification. Furthermore the global ocean mass budget is important for our understanding of the sea level change. Ocean mass variations appear on many different temporal and spatial scales which exceed the possibilities of just one instrument. The seasonal cycle of the ocean mass budget is well observed by space-geodetic observations such as time-variable gravity (Gravity Recovery And Climate Experiment, GRACE)or altimetry. Chambers et al. (2004) found a seasonal variability of 6-8mm equivalent water height peaking in September-October and interannual variability. To investigate other time scales (shorter or longer than annual) of ocean mass variations the shortcomings of geodetic tools have to be overcome. To tackle this problem and to improve the understanding of ocean mass variations data derived from three different measurement systems were combined in a joint inversion by Rietbroek et al. (2012). Rietbroek

et al. (2012) use a weekly solution of gravity changes from the Gravity Recovery
and Climate Experiment (GRACE), modeled ocean bottom pressure (OBP) from
the Finite Element Sea Ice Ocean Model (FESOM) and large scale deformation
patterns measured by a network of Global Positioning System (GPS) stations to
derive changes in OBP and hence ocean mass variations. For the three data sets
a joint least square inversion was performed to determine weekly solutions of mass
anomalies. The inversion is derived globally hence it resolves signals over land and
ocean. The solution over land is determined by GRACE and GPS while the solution
over the ocean is further influenced by the ocean model (FESOM). Correlating the
results of the inversion with in-situ OBP measured by bottom pressure recorders
(BPRs) like e.g. PIES showed mean correlation coefficients of 0.4 (see Figure 3.1(a).
Rietbroek et al. (2012)). The inversion is performed in a spectral domain up to
degree and order 30. This results in a spatial resolution of about 500 km depending
on latitude. Furthermore the seven parameters (translation vector C, scale factor
μ and rotation matrix R) of an Helmert transformation(Eq. 3.1) are estimated.
The Helmert transformation is a transformation of coordinated commonly used in
Geodesy for distortion-free conversion between two reference frames (initial vector
X and transformed vector X_T). They are estimated to reveal inconsistencies in the
GPS network.

$$X_T = C + \mu \cdot R \cdot X \tag{3.1}$$

The inversion of Rietbroek et al. (2012) additionally estimates the global mean
ocean mass variability which is used to calculate a bias term to correct the FESOM
model (Brunnabend et al., 2011). The bias is the difference between the global
mean ocean mass variability derived by the inversion and by FESOM. The study of
Brunnabend et al. (2011) showed an improvement in all model results using the bias
term to scale the fresh water input. The scaling improved the consistency between
FESOM, GRACE and GPS displacements.
The aim of this study is to investigate the possibility of a further improvement of the
inversion by adding in-situ measurements obtained from the global OBP database
by Macrander et al. (2010).

3.2 Method

3.2.1 Inversion

The solution of a linear equation system such as Eq. 3.2 is called an inversion.

$$A \cdot \vec{x} = \vec{b} \tag{3.2}$$

A is called design matrix, which linearly propagates the solution vector $\vec{x}$ into a spatial domain. $\vec{b}$ is the vector containing the observations. The inversion combines observations of different kind which have to be weighted according to their importance. The weight is generally given by the inverse of the covariance matrix C of the observations. After weighting Eq. 3.3 follows with N being the normal matrix and $\vec{d}$ represents the normalized observations.

$$\underbrace{(A^T C^{-1} A)}_{N} \cdot \vec{x} \qquad\qquad = \underbrace{A^T C^{-1} \cdot \vec{b}}_{\vec{d}} \tag{3.3}$$

$$N \qquad \cdot \vec{x} \qquad\qquad = \qquad \vec{d}$$

The linearity of Eq. 3.3 allows to expand the existing system (denoted with index R) of Rietbroek et al. (2012) by adding a normal-matrix N_{BPR} and a weighted observation vector $\vec{d}_{BPR}$ for the BPRs (Eq.3.4)

$$(N_R + N_{BPR}) \cdot \vec{x} = \vec{d}_R + \vec{d}_{BPR} \tag{3.4}$$

To solve Eq. 3.4 the following coast function F is minimized (Eq. 3.5) in a least square sense.

$$F = [(N_R + N_{BPR}) \cdot \vec{x} - (\vec{d}_R + \vec{d}_{BPR})]^T \cdot [(N_R + N_{BPR}) \cdot \vec{x} - (\vec{d}_R + \vec{d}_{BPR})] \tag{3.5}$$

To create the BPR normal matrix, a design matrix A_{BPR} and a covariance matrix C_{BPR} is needed. The design matrix is generated from associated Legendre functions (Eq. 3.6) evaluated at the BPR positions (3.7).

$$Y_{nm} = \begin{cases} m \geq 0 & : & P_{nm}(\cos\theta)\cos m\lambda \\ m < 0 & : & P_{nm}(\cos\theta)\sin m\lambda \end{cases} \tag{3.6}$$

The design matrix A_{BPR} is here developed until degree and order 30 to be compatible with the normal matrix of Rietbroek et al. (2012) (Eq. 3.7).

$$A_{BPR} = \begin{bmatrix} Y_{0,0}(\theta_1,\lambda_1) & \cdots & Y_{30,30}(\theta_1,\lambda_1) \\ \vdots & \ddots & \vdots \\ Y_{0,0}(\theta_k,\lambda_k) & \cdots & Y_{30,30}(\theta_k,\lambda_k) \end{bmatrix} \tag{3.7}$$

The amount of BPR data per week is denoted by k and changes with time. Hence a design matrix is constructed for each GPS week individually.

Building the covariance matrix C is not straightforward because of the different length of the BPR time series and different deployment times. In a mathematical sense a covariance matrix can only be derived for coherent time series. Hence there is no obvious mathematical covariance matrix C for this problem. The following section (3.2.2) describes how a covariance matrix for the BPRs can be designed.

3.2.2 Covariance Matrix and Scaling Factor

The BPR data are not consistent in time and space and hence a covariance matrix in the mathematical sense does not exist. To overcome this problem the covariance matrix used in the inversion is chosen as a diagonal matrix of the variances. The magnitude of the variances strongly depends on the region of BPR deployments. The smallest variance observed in the data set is 0.08 mm while the largest is 13 mm. To account for the error of the measurement a constant of 1 mm was added to each diagonal element. The "covariance matrix" C designed for the inversion hence becomes:

$$C = \begin{bmatrix} var(pres_1) + 1mm & \cdots & 0 \\ \vdots & \ddots & \vdots \\ 0 & \cdots & var(pres_l) + 1mm \end{bmatrix} \tag{3.8}$$

The correlation of the inversion result using this approach with the BPRs is shown in Figure 3.1(b). The difference to the correlations shown in Figure 3.1(a) is almost everywhere positive (some points in the KESS array are not) and lies between 0%

and 5%. This small increase in correlation is clearly below the expectations and indicates that the covariance matrix does not provide an appropriate weight for the inversion. Increasing the weight by scaling the inverse covariance matrix with a factor of 10 (Figure 3.1(c)) or 100 (Figure 3.1(d)) cleary increases the correlation up to a mean of 83% in the case of hundretfold weight.
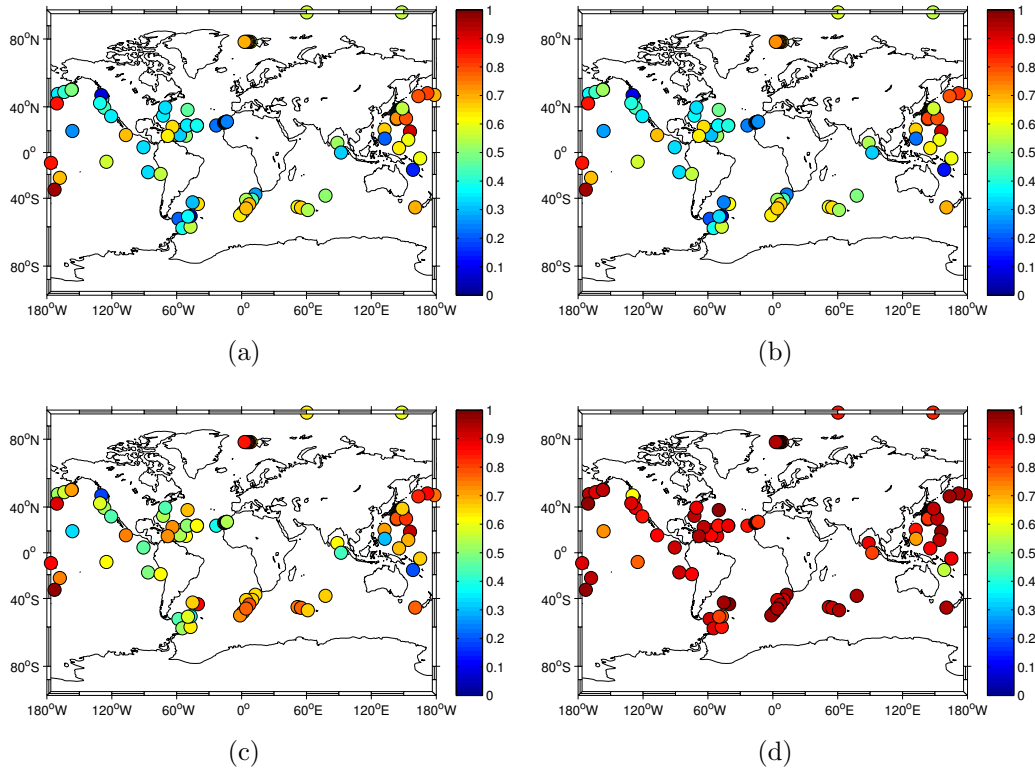

Figure 3.1: Correlation with in-situ ocean bottom pressure (OBP), (a) for the inversion of Rietbroek et al. (2012), (b) inversion with all BPRs included and covariance matrix C (Eq. 3.8), (c) inversion with all BPRs included and covariance matrix $0.1 \cdot C$ and (d) inversion with all BPRs included and covariance matrix $0.01 \cdot C$

It is obvious that including in-situ ocean bottom pressure from BPRs into the inversion increases the correlation with the BPRs. The magnitude of increase depends on the weight put on the normal equations of the BPRs (Figure 3.1). The weight is determined by the inverse of the covariance matrix C (see Eq.3.3). To tune

the inversion with in-situ OBP in a way that the correlation with in-situ OBP is
increased in most of all places the inverse covariance matrix C^{-1} is now multiplied
with a scaling factor α.
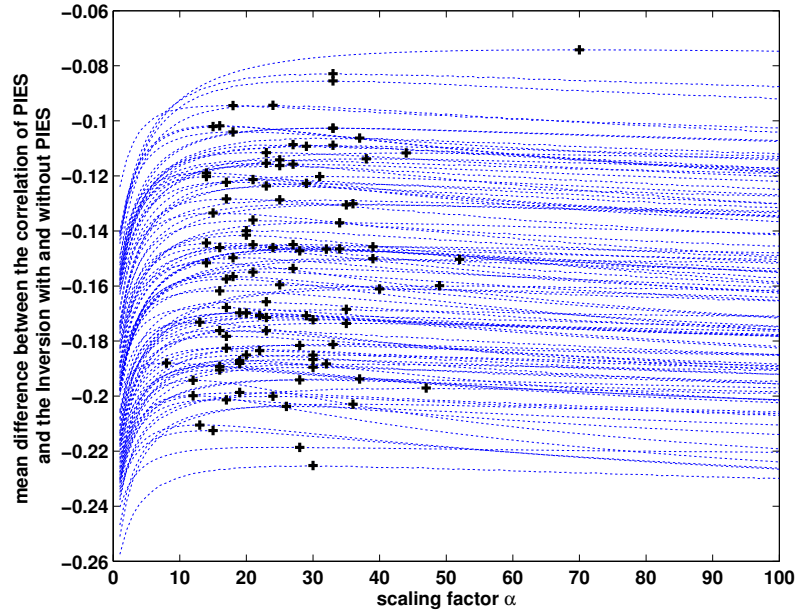
Figure 3.2: Mean difference of the correlations with and without BPRs included into
            the inversion for different scaling factors α and randomly chosen subsets
            of OBP included in the inversion. The black crosses mark the maximum
            of the differences.

To find the appropriate scaling factor a test was designed as follows. From the
full BPR dataset including 127 time series a sub set of 63 was randomly taken and
included in the inversion while the remaining 64 BPRs are used for validation. The
inversion was performed with a scaling factor α from 1 to 100 for 100 different ran-
dom test data sets and correlated against the BPRs not included. To figure out if
the inversion with BPR does better than the inversion without BPRs the correlation
of the run without the BPRs has been subtracted from the correlations of the vali-
dation datasets. Figure 3.2 shows the mean difference between the inversions with
and without BPR data included against different scaling factors α and Figure 3.3
shows a histogram of the maximum differences for the different scaling factors.

Figure 3.3 shows that the maximum differences of correlations with and with-
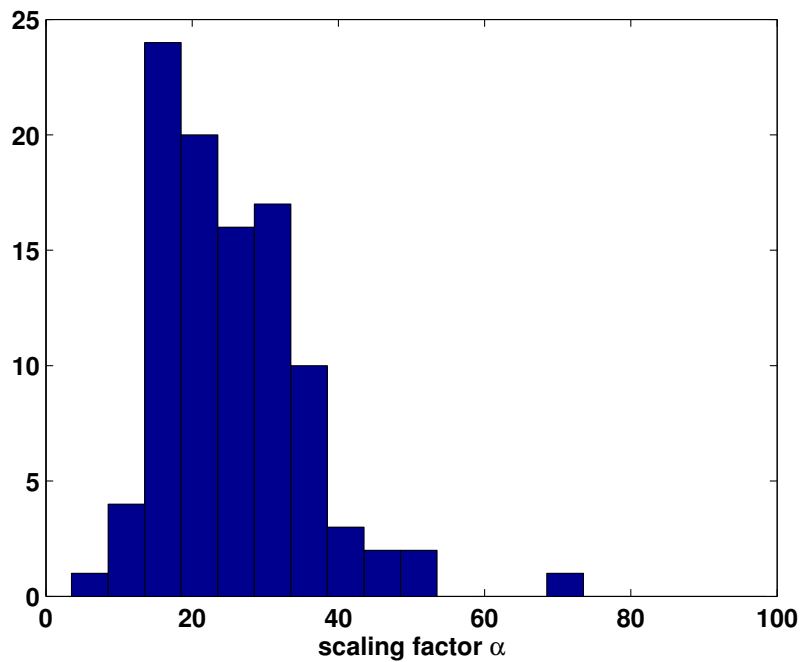out BPRs are reached at a scaling factor between 15 and 40. The median of the

Figure 3.3: Histogram of the maximum differences shown in Figure 3.2 regarding the scaling factor α.

histogram is at a scaling factor of 24. The correlations of the validation datasets for the scaling factor $\alpha = 24$ varies strongly (see Figure 3.10). Some of them are even zero or negative. Excluding the BPRs with low or negative correlation from the analysis does not change the median of scaling factors for the maximum of the mean correlation differences. Hence for all further investigations the scaling factor $\alpha = 24$ is used.

3.3 Data

The in-situ OBP data measured by BPRs were obtained from the AWI database
of Macrander et al. (2010). Figure 3.4 shows the global distribution of the in-situ
measurements and indicates the different arrays like the Meridional Overturning
Variability Experiment (MOVE) or the Antarctic array (AWI_ANT) also used in
chapter 2.
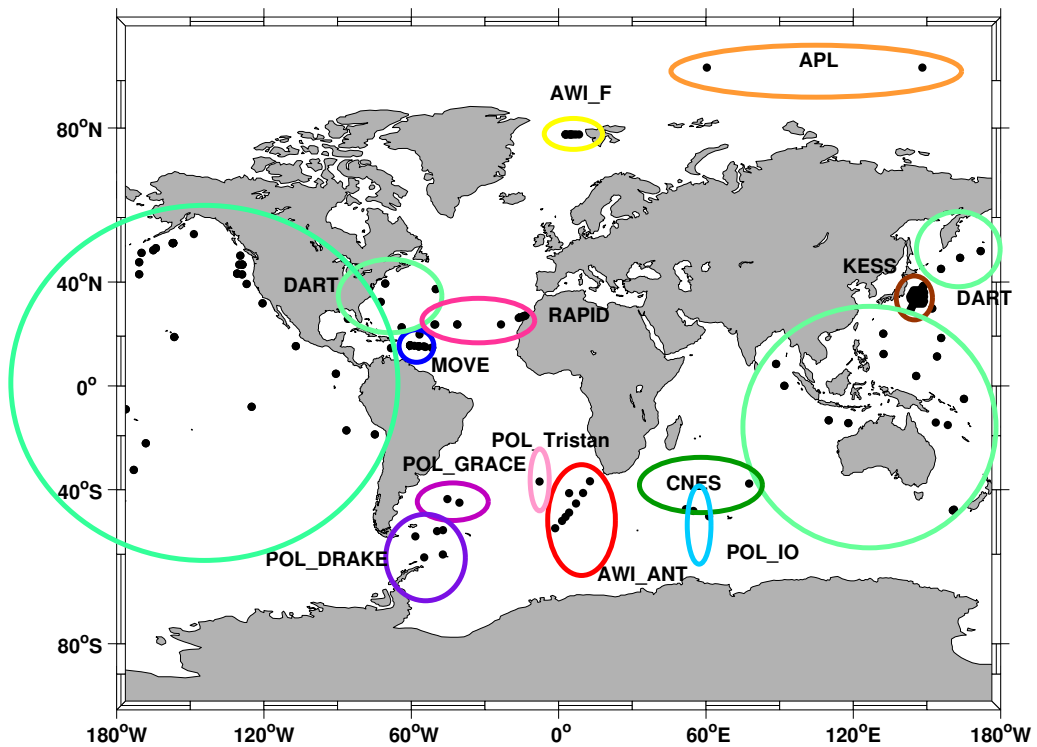
Figure 3.4: Spatial distribution of in-situ OBP data. The circles indicates the ar-
            ray/project the data belongs to.

The inversion of Rietbroek et al. (2012) results in a global solution between the
GPS weeks 1200 and 1511 and is just interrupted between 1220-1223 and 1253-1255
because of a lack of GRACE data. The in-situ measurements do not cover a similar

spatiotemporal resolution, their spatial distribution varies with time. The histogram in Figure 3.5 shows the amount of BPRs which are available for each gps week.
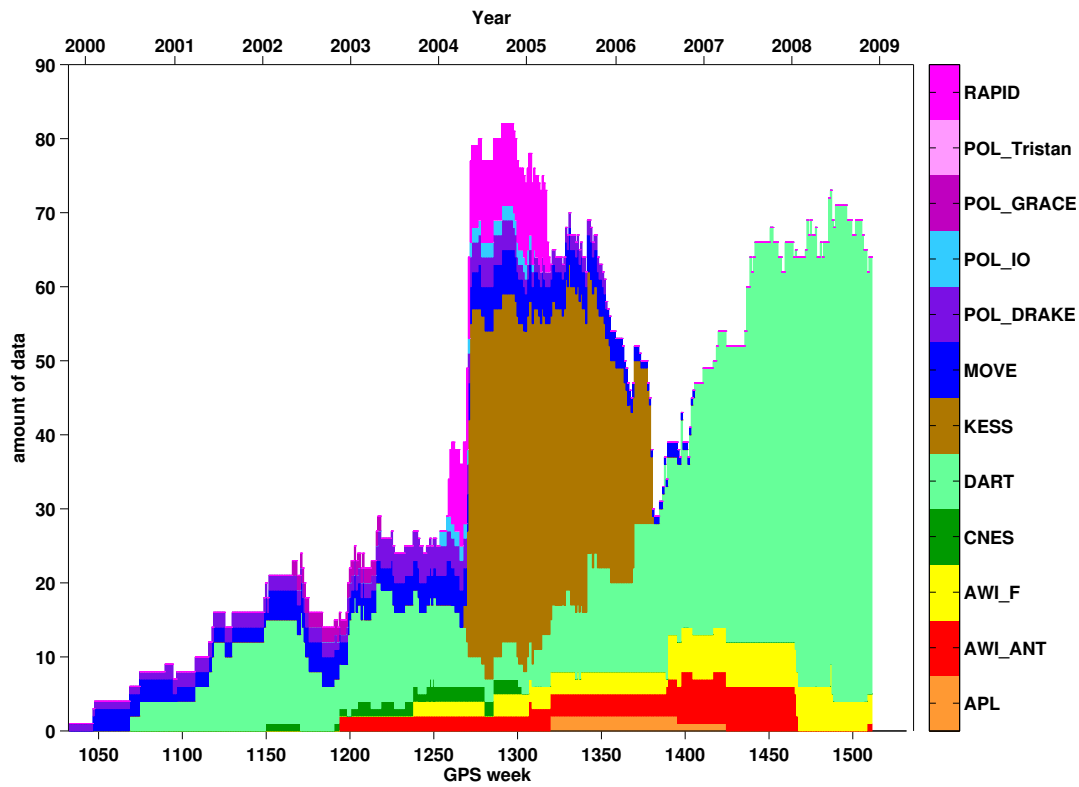
Figure 3.5: Histogram of the available BPRs per gps week.

It should be noted that there are arrays such as KESS or AWI_F were the distance between the BPRs is small and partly below the resolution of the inversion. This might artificially increase the weight of this arrays in the inversion.

3.4 Results

3.4.1 Changes in the spectral domain

Figure 3.6(a) shows the standard deviation of the spherical harmonic coefficients of the inversion with all BPRs included in the inversion. The highest standard deviations are observed between degree 13 and 21.
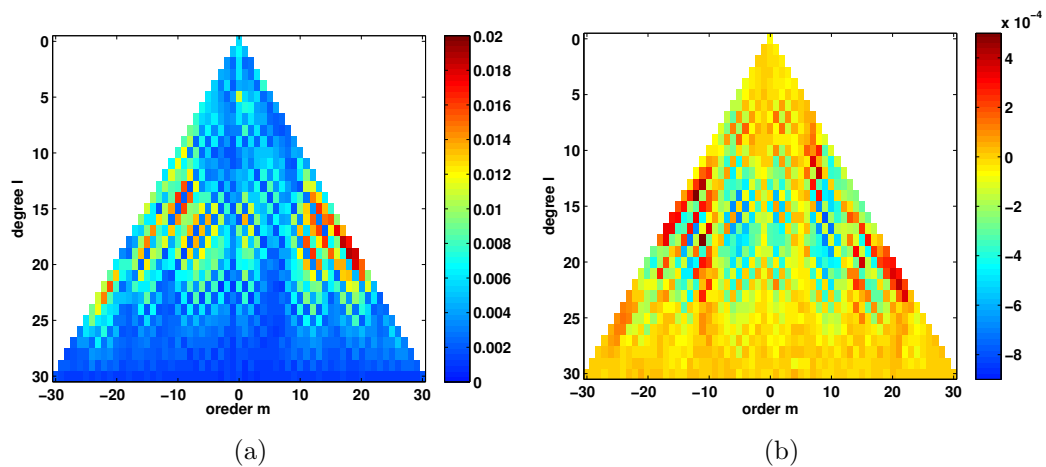
Figure 3.6: (a) shows a Triangle plot of the standard deviation of the spherical harmonic coefficients of the inversion with BPRs. (b) shows a Triangle plot of the difference between the standard deviation of the spherical harmonic coefficients of the inversion with and without BPRs.

Figure 3.6(b) shows the difference between the standard deviation of the spherical harmonic coefficients of the inversion with and without BPRs included. The largest differences occur between degree 7 and 23 and orders of 10 to 30 which means that the changes in the spatial domain are mostly local.

3.4.2 Correlation of the inversion with in-situ measurements

The inversion with BPRs shows high correlations with the BPRs at most positions. This result is expected because the BPR are included as additional information in the inversion. The highest correlations are observed in the central Pacific Ocean, Fram Strait and the Southern Ocean. Whereas the lowest correlations are found at the Californian coast and the Philippine Sea (Figure 3.8).
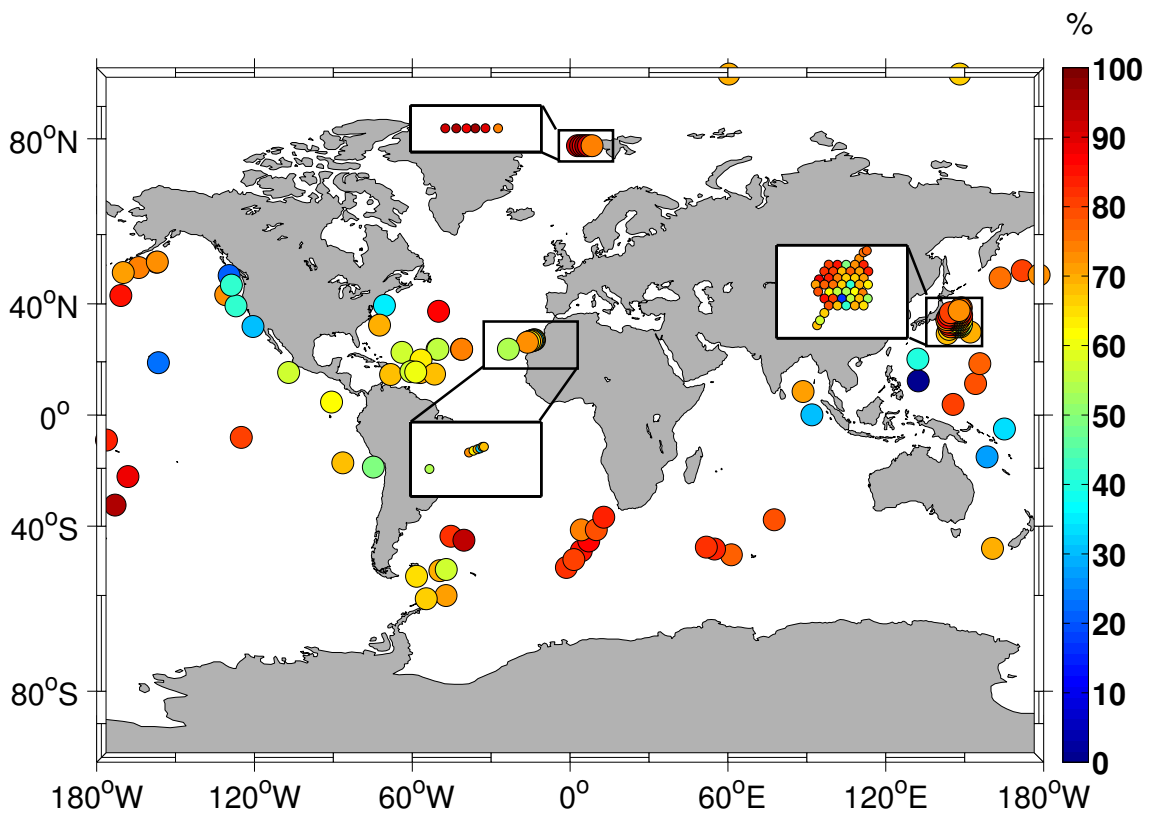

Figure 3.7: Correlations between the BPRs and the inversion with all BPRs included.
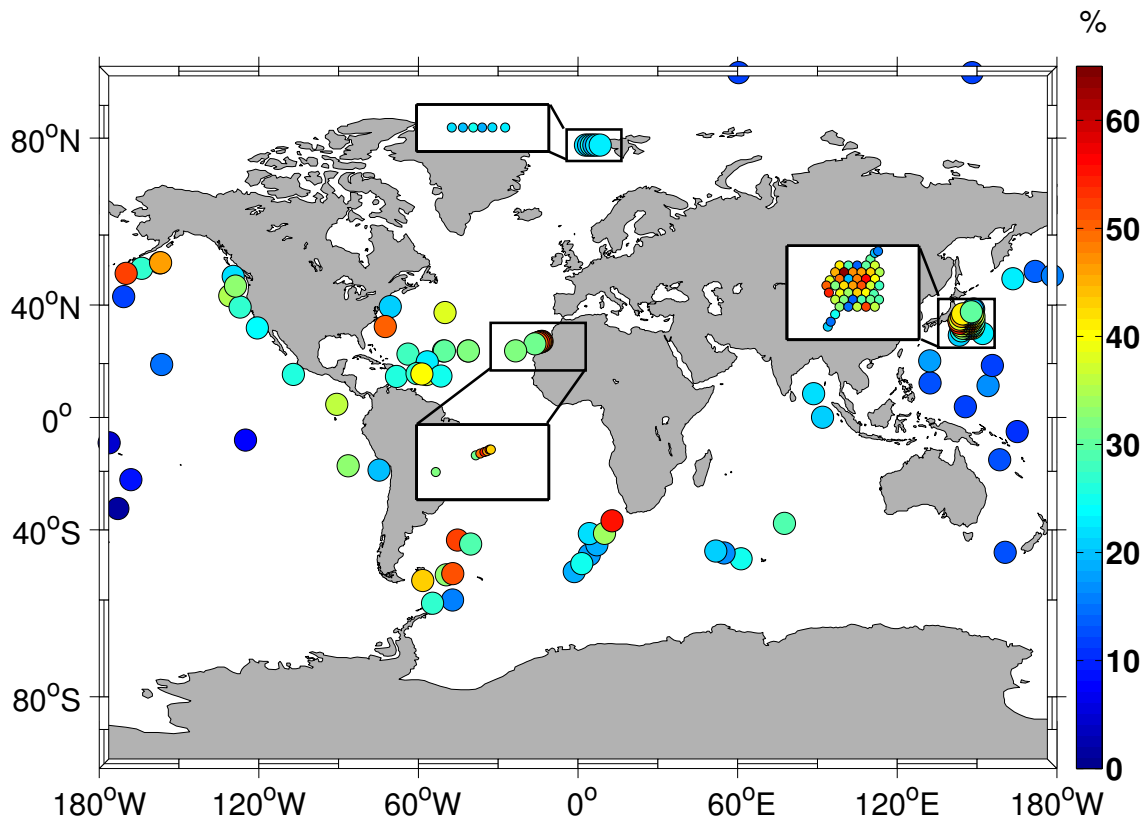
Figure 3.8: Difference between the correlations of the BPRs with the inversion of
Rietbroek et al. (2012) and the inversion with all BPRs included.

Including the BPRs into the inversion improves the correlation between 1% and
63% and on average 30% (Figure 3.8). The change in correlation is not evenly
disributed over the different BPR. The smallest increase is observed in the central
Pacific Ocean, a region where the correlations have been high before including the
BPR into the inversion. The increase in correlation depends on the correlation
of the inversion without BPR (Figure 3.9). The correlation coefficient between the
inversion without BPRs included and the increase of the correlation is anticorrelated
with a correlation coefficient of -0.57. This means that the BPRs which had already
been well correlated are systematicly less improved compared to the BPRs with low
correlatiopns.
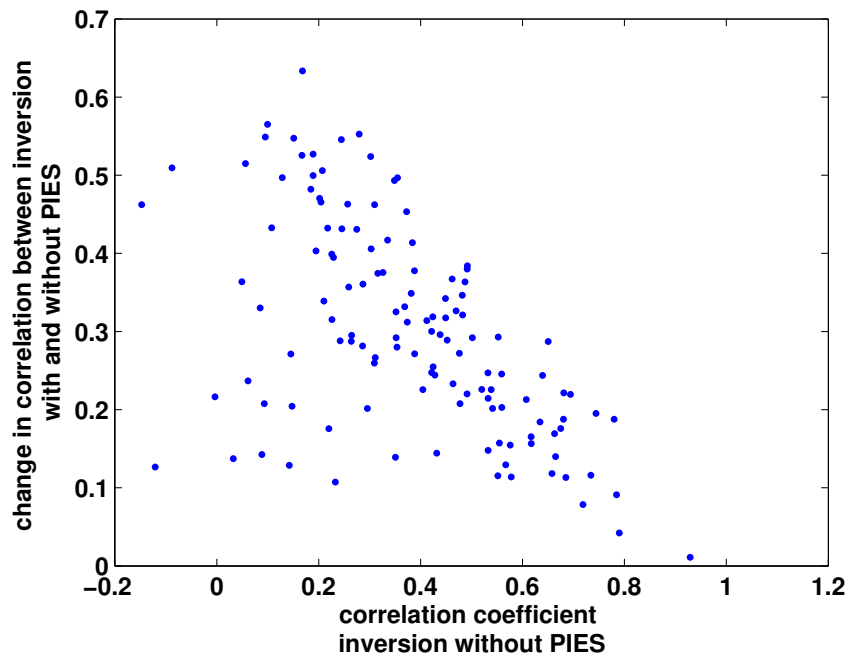
Figure 3.9: Change in correlation vs. correlation of the inversion without BPRs.

3.4.3 Different subsets of in-situ OBP and their influence on the correlation with BPR

The randomly chosen subsets of the scaling factor test were used to investigate the influence of different subsets onto the correlation with BPRs. Half (63 out of 127) of the BPR positions were included into the inversion and the other half was used for validation. The correlations show a wide spread of up to 10% at some positions.
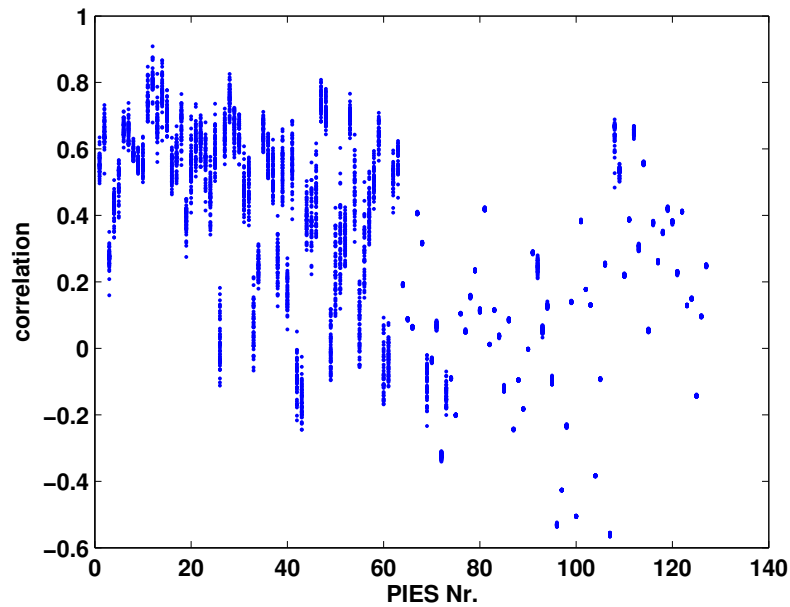
Figure 3.10: Correlations of the validation data sets and the inversion with different randomly chosen subset of BPR positions. Half of the BPRs were included and the other half was used for validation.

Figure 3.10 shows the correlation at the single BPR positions denoted by numbers (see Appendix C) for the hundred randomly chosen test cases.

3.4.4 Standard deviation and change of variance of the Inversion with BPR

Figure 3.11 (be aware of the nonlinear color scale) shows the standard deviation of the inversion over time. The inversion is performed globally hence also results mass variations over land, which are due to hydrological cycle. Because the BPRs are placed in the ocean their inclusion into the inversion should have no effect on the standard deviation over land. The highest standard deviation is seen in the Amazon basin. Generally the standard deviations over land are higher than over the ocean and coincide with places showing a strong hydrological cycle. Their are no unrealistic peaks over land indicating that the inclusion of the BPRs influence this part of the solution.

The highest signals over the ocean are found in the Arctic (0.06-0.07 m) and the ACC (0.04-0.05 m).
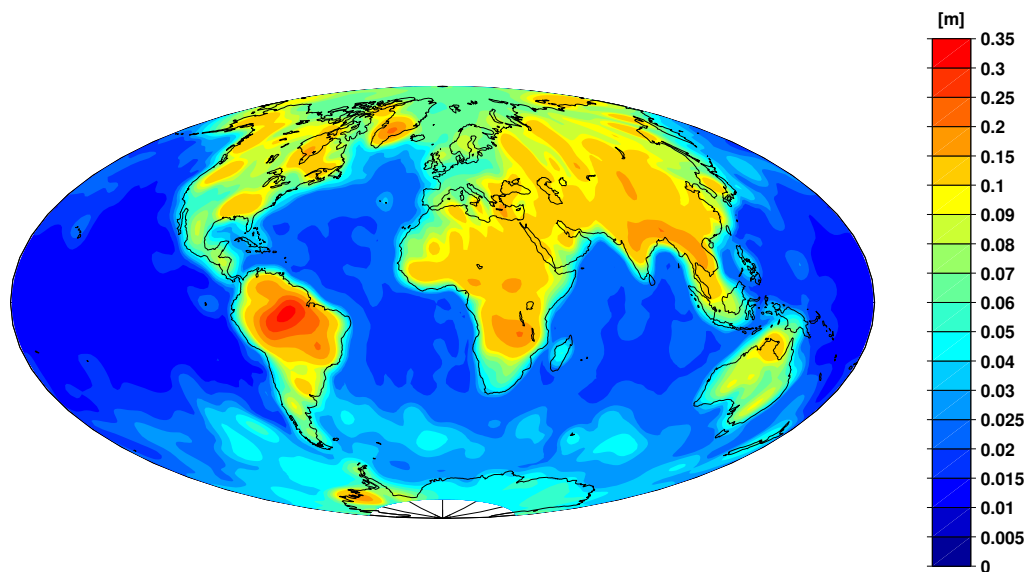
Figure 3.11: Standard deviation of the inversion with BPRs included. An nonlinear color scale is used to make the small scale features in the ocean visible.

To investigate the changes caused by including the BPRs into the inversion the variance difference is normalized by the variance of the inversion of Rietbroek et al.

(2012) (Eq. 3.9).

$$p = \frac{var(\text{Inversion of Rietbroek et al. (2012)}) - var(\text{Inversion with BPR})}{var(\text{Inversion of Rietbroek et al. (2012)})} \quad (3.9)$$
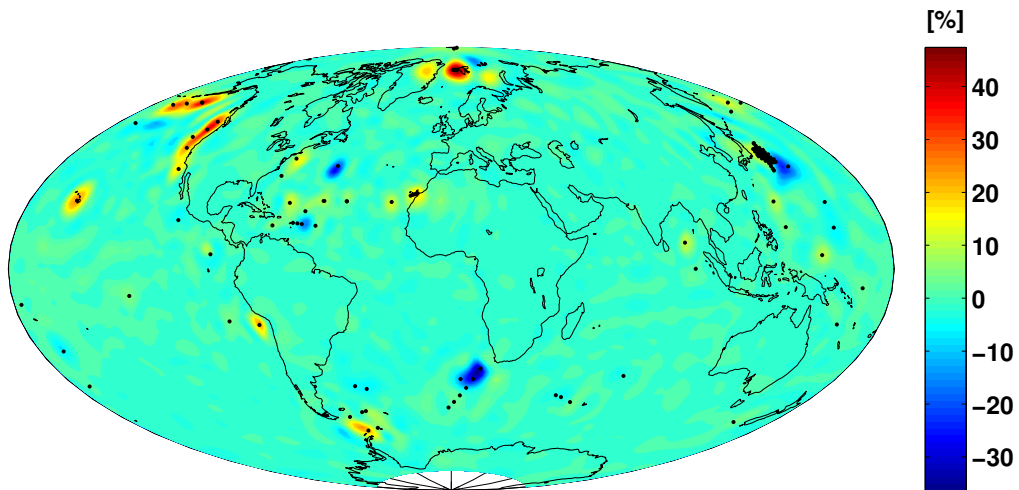

Figure 3.12: Change of variance of the inversion with BPRs included, in percent of the variance of the inversion of Rietbroek et al. (2012). The black dots indicate the positions of the BPRs.

The changes in variance appear locally around the BPR positions. Their strength varies between -36 and 49%. The change is positive at the coasts of North and South America and Africa, in Fram Strait, Drake Passage and Hawaii. Negative changes are observed south of Africa in the North Atlantic and the Kess array region.

3.4.5 Global ocean mean mass anomalies and geocenter motion

The global ocean mean mass anomalies derived from the inversion of Rietbroek et al. (2012) was used in the study of Brunnabend et al. (2011) to improve the modeled mass budget. The global ocean mean mass anomalies are derived excluding areas shallower than 600 m and the Mediterranean Sea.

In Figure 3.13 the global ocean mean mass anomalies are depicted for the inversion with (red) and without (blue) BPRs included in the inversion. Adding the BPRs to the inversion does not visibly change the global ocean mean mass anomalies.
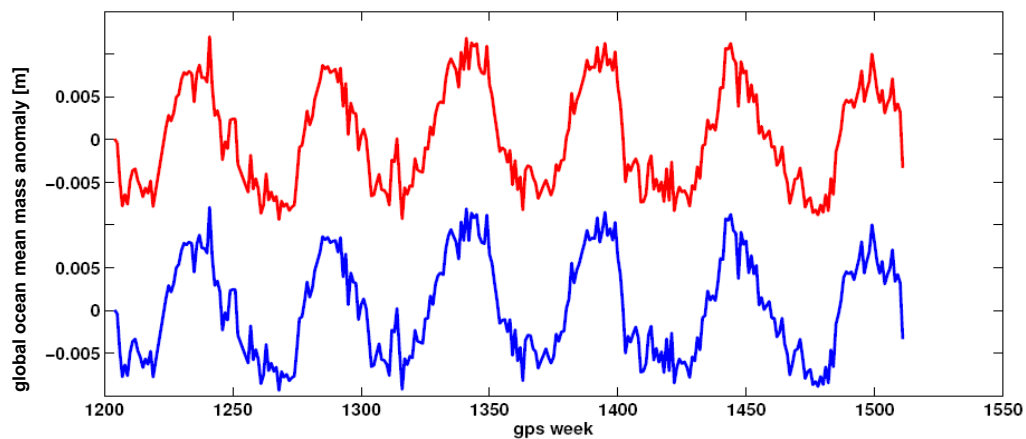
Figure 3.13: Global ocean mean mass anomaly of the inversion without BPRs (blue) and the inversion with BPRs (red)

Figure 3.14 shows the differences between the two global ocean mean mass anomalies which are in the order of 0.1 mm.
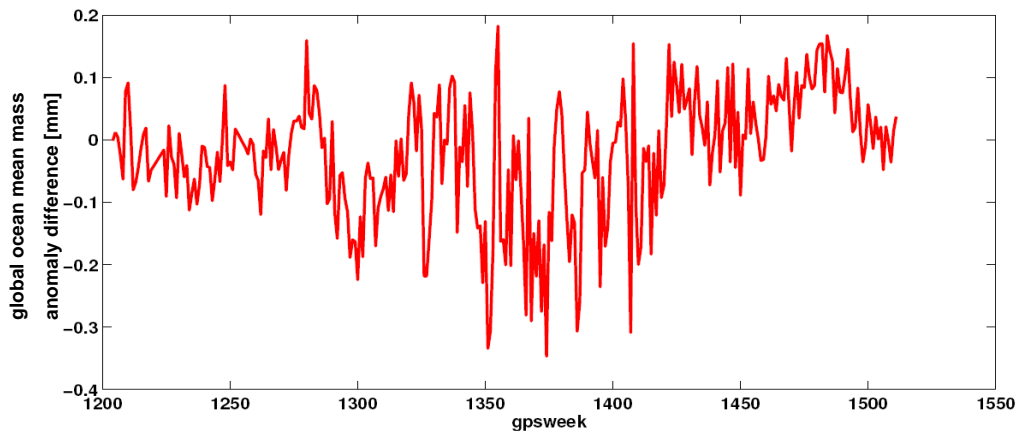
Figure 3.14: Difference between the global ocean mean mass anomaly of Rietbroek
          et al. (2012) and the inversion with BPRs.

The differences between the degree 1 coefficients of the in version with BPRs
included and the inversion of Rietbroek et al. (2012) are shown in Figure 3.15 and is
in the order of 0.1-0.3 mm while the signal of this degree is in the order of 1 cm. The
geocenter motion, which is a quantity of major interest to the geodetic community,
is represented by the variation of the degree 1 (Heiskanen and Moritz, 1967)
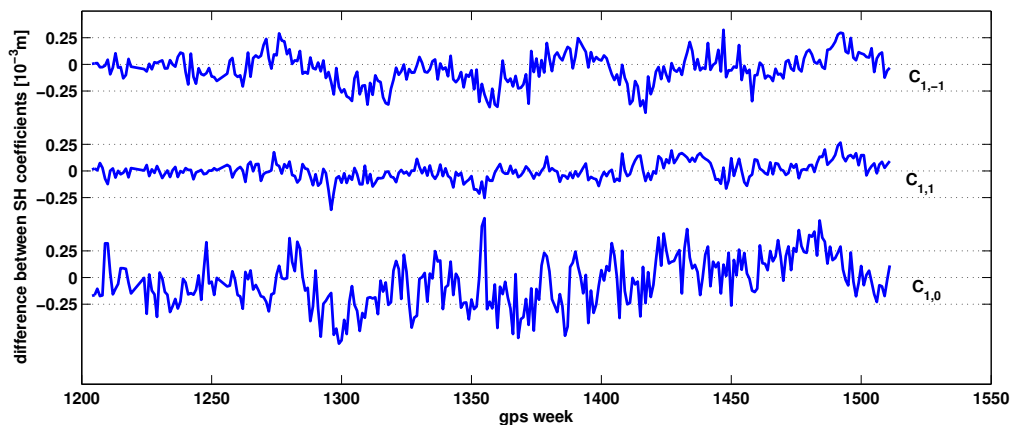
Figure 3.15: Difference between SH Coefficients of degree 1 from the inversion of
          Rietbroek et al. (2012) and the inversion with BPRs.

3.5 Discussion

Rietbroek et al. (2012) designed an inversion of 3 different data sets (GRACE, GPS, and modeled OBP) to investigate the geocenter motion and the ocean mass changes. This inversion was validated against in-situ OBP data measured by BPRs obtained from the database of Macrander et al. (2010). The intention of this study was to improve the inversion of Rietbroek et al. (2012) by including the in-situ measurements into the inversion. As for the original inversion, weighting the observations was a difficult issue. The mathematical correct weighting matrix is the inverse of the covariance matrix, which does not exist in the case of the BPRs due to their inhomogeneous distribution in time. For this reason the diagonal matrix of variances was used as weighting matrix instead of the covariance matrix. This causes the problem of underestimating the weight of the BPR by neglecting their relationship and results only in small changes of the inversion and hence the correlation coefficients with the included BPRs (see Figure 3.1(b)). To overcome this problem a scaling factor α was introduced and determined by a statistical test scenario. This scaling factor has no physical meaning and hence can hardly be proven to be correct for any other dataset than the one used. All other weighting matrices of data sets used in the inversion are also scaled in some way (personnel communication R. Rietbroek). The determined scaling factor ($\alpha = 24$) leads to higher correlations between the inversion and the included BPRs influencing the inversion only locally (Figure 3.12). A local change was expected because the BPR are not globally distributed and their number changes from week to week.

Including only half of the BPRs into the inversion however increases the correlation of the inversion with the BPRs not included. The amount of increase is highly variable due to choice of BPRs included into the inversion. This can be explained by the local influence on the inversion of the included BPRs. Böning et al. (2008a) showed patterns of coherent ocean bottom pressure variability, which are used to improve the GRACE solution. The patterns of coherent ocean bottom pressure variability imply that a whole array can be improved by including only one BPR into the inversion.

Figure 3.16 shows the correlations between the individual BPRs which are in some cases quite high. For example the RAPID array (BPR Nr. 117-127) shows correla-
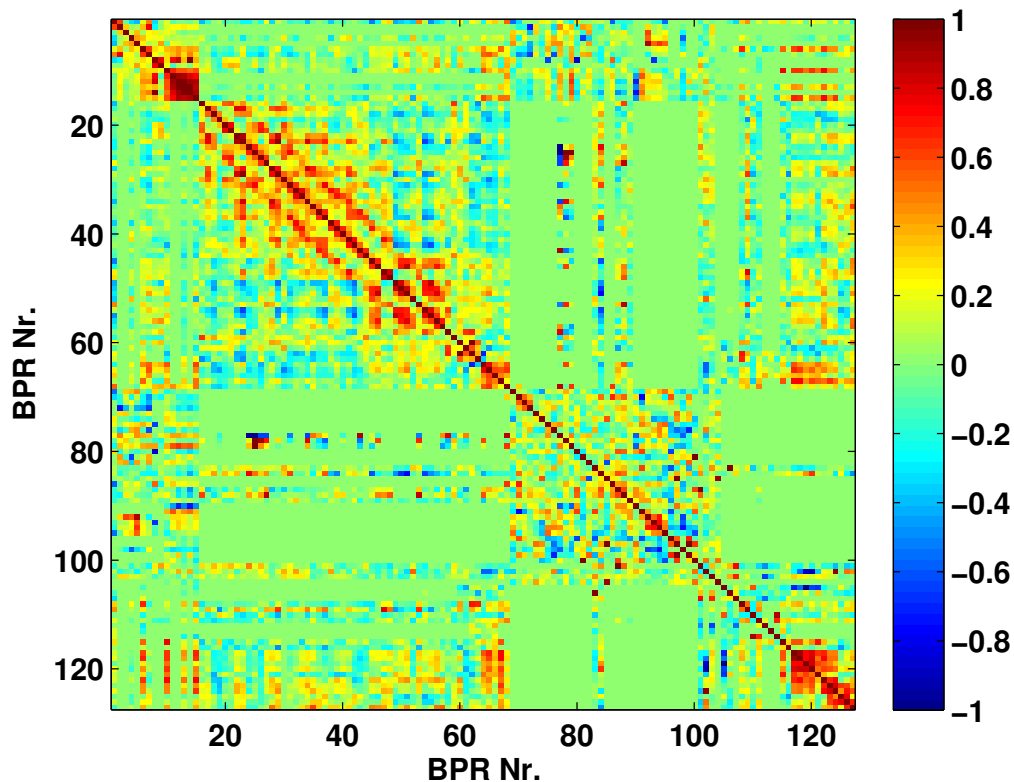
Figure 3.16: Correlation between the BPRs.

tions higher than 0.6 at most places. Hence it can be expected that including not all of them into the inversion will increase the correlation with the excluded ones as well. The same will hold true for other arrays for example the AWI Fram Strait array or the KESS array.

The inversion was designed to address properties like global mean ocean mass anomalies used to improve the ocean model FESOM (Brunnabend et al., 2011) and the geocenter motion (Rietbroek et al., 2012). This study investigates the possibility of improving the inversion and hence the global mean ocean mass variability and geocenter motion. Neither the global mean ocean mass variability nor the geocenter motion (see Figure 3.13-3.15) are significantly influenced by the addition of BPRs to the inversion. This may have different reasons. On the one hand BPR measurements are point measurements within coherent ocean bottom pressure patterns but these patterns are not taken into account for the inversion. The normal equation

translates the point measurements into the spectral domain without regard to more global patterns. On the other hand the BPR sites are not evenly distributed over the globe. Their amount and distribution change from week to week. The difference between the global mean ocean mass variability derived from the inversions with and without BPRs shows less variability for the GPS week 1200 to 1270 a period where only about 25 BPRs had been active. After the week 1270 the KESS array was in place and the DART array increases it's number of measurements and so does the difference between the global mean ocean mass variabilities. This indicates that a larger amount of BPRs might have a larger influence on the inversion.

Another more fundamental problem is the difference in signal amplitude over land and ocean. The amplitude of the hydrological cycle over land is one order of magnitude larger than the largest amplitudes found in the ocean (see the standard deviation in Figure 3.11). Because of these differences in signal magnitude the inversion is not very sensitive against small local changes in the ocean. The global properties (global mean ocean mass anomalies and geocenter motion) are dominated by the signal of the hydrological cycle and not by small scale ocean signals.

3.6 Conclusions

In conclusion it is possible to include in-situ measurements of ocean bottom pressure into the inversion. The changes are only small and local and do not influence global parameters like global ocean mean mass variability or geocenter motion. A larger amount of data might have a larger influence on the inversion. Such a data set of BPRs should be equally distributed over the global ocean, but is not available at the moment or in the near future. A more promising way to improve the inversion would be to improve the ocean model which is one of the three major parts of the inversion. Another promising way to improve the inversion would be to improve the GRACE processing.

Appendix

A List of Acronyms

AAO	Antarctic Oscillation
AABW	Antarctic Bottom Water
AAIW	Antarctic Intermediate Water
ACC	Antarctic Circumpolar Current
AVISO	Archiving, Validation and Interpretation of Satellite Oceanographic data
AWI	Alfred Wegener Institute
BPR	Bottom Pressure Recorder
CDW	Circumpolar Deep Water
CNES	Centre National d'Etudes Spatiales
CPIES	Current and Pressure Recording Inverted Echo Sounder
CTD	Conductivity Temperature Depth
CWT	Continuous Wavelet Transformation
DART	Deep-ocean Assessment and Reporting of Tsunamis
DGFI	Deutsches Geodätischen Forschungsinstitut
ECCO	Estimating the Circulation & Climate of the Ocean
EOF	Empirical Orthogonal Function
FESOM	Finite Element Sea ice Ocean Model
GEM	Gravest Empirical Mode
GODAE	Global Ocean Data Assimilation Experiment
GPS	Global Positioning System
GRACE	Gravity Recovery and Climate Experiment
GSO	Graduate School of Oceanography
IB	Inverse Barometer
IES	Inverted Echo Sounder

KESS	Kuroshio Extension System Study
MADT	Maps of Absolute Dynamic Topography
MITgcm	Massachusetts Institute of Technology General Circulation Model
MODE	Mid-Ocean Dynamic Experiment
MOVE	Meridional Overturning Experiment
NADW	North Atlantic Deep Water
NIDW	North Indian Deep Water
OBP	Ocean Bottom Pressure
OpenADB	Open Altimeter Data Base
PF	Polar Front
PIES	Pressure Inverted Echo Sounder
RMS	Root Mean Square
RSW	Red Sea Water
SACCF	Southern ACC Front
SAF	Subantarctic Front
SASW	Subantarctic Surface Water
SH	Spherical Harmonics
SICW	South Indian Central Water
SLA	Sea Level Anomaly
SOSE	Southern Ocean State Estimate
SSH	Sea Surface Height
STF	Subtropical Front
STSW	Subtropical Surface Water
URI	University of Rhode Island

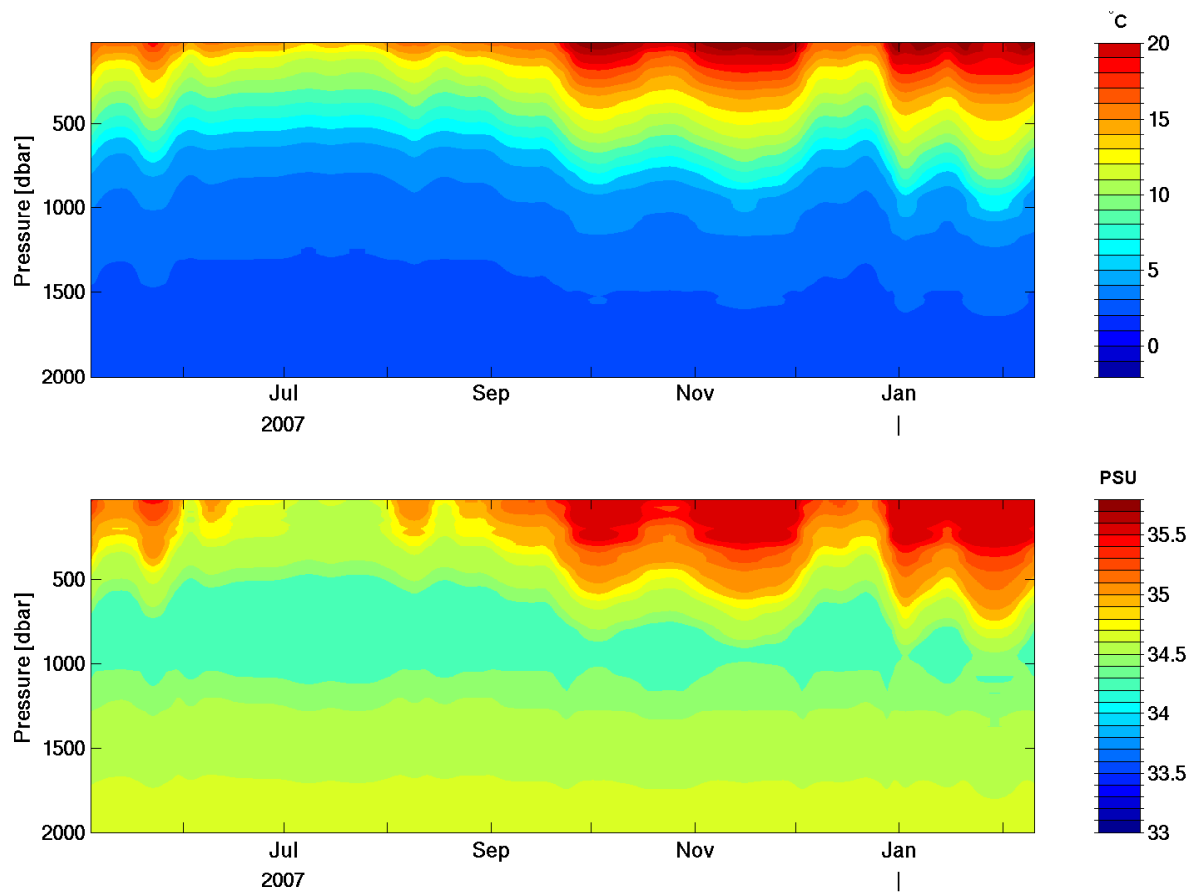# B Potential temperature and salinity time series of the ACC PIES

Figure B.1: Potential temperature (top panel) and salinity (bottom panel) time se-
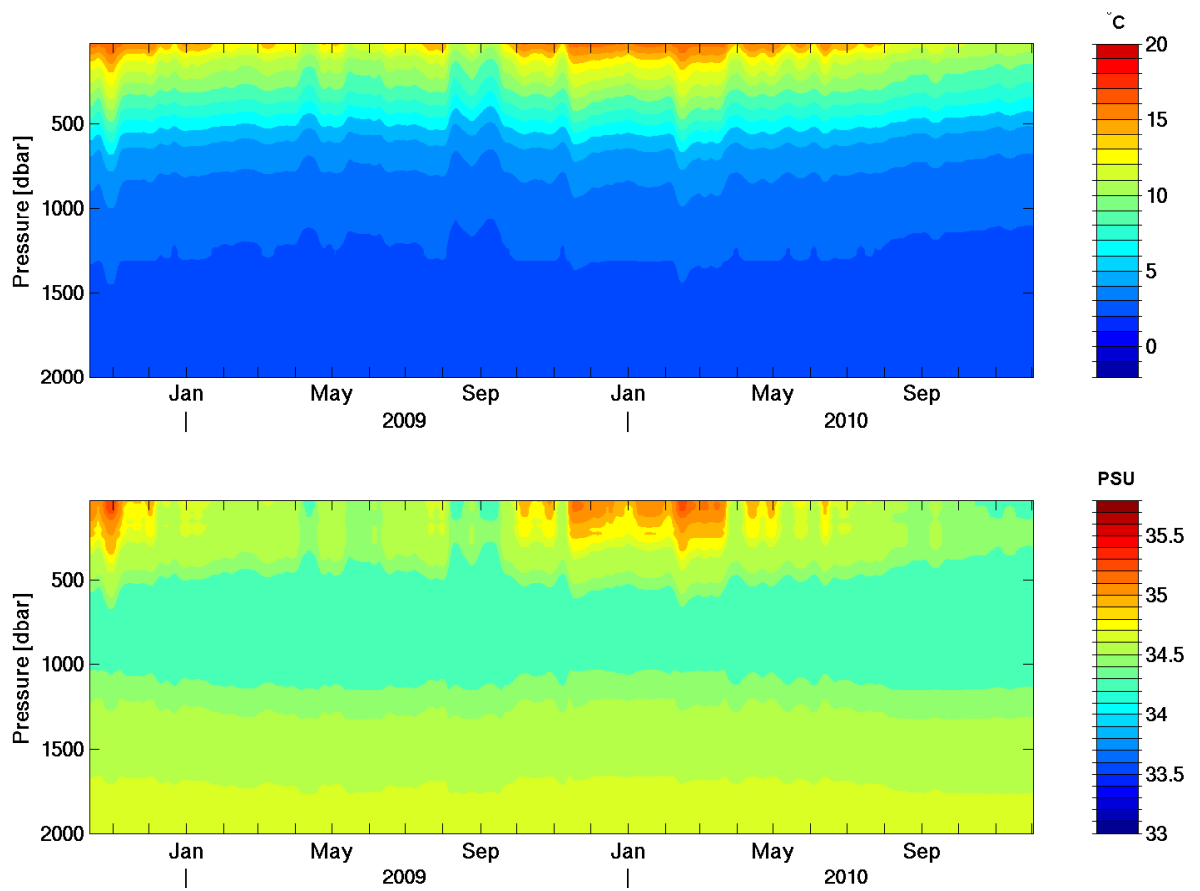ries at the position ANT 3

Figure B.2: Potential temperature (top panel) and Salinity (bottom panel) time
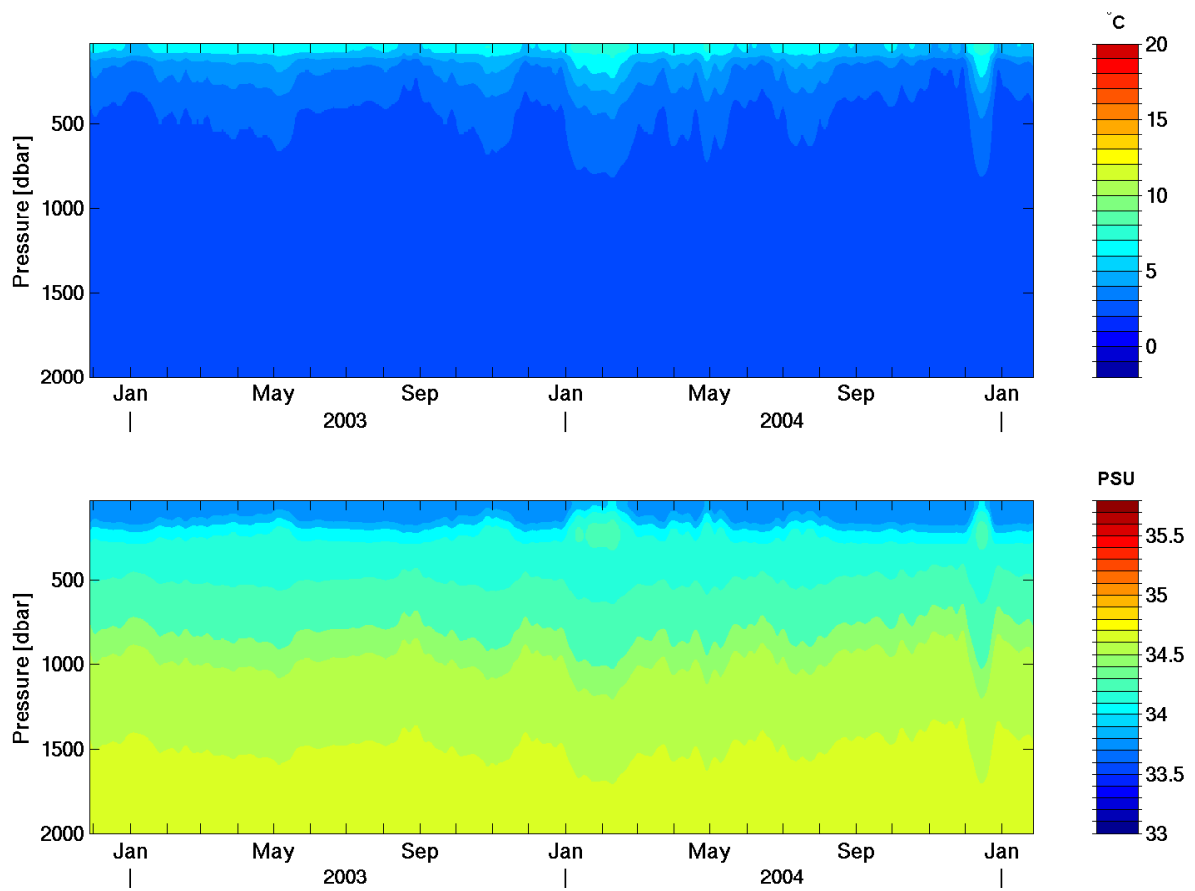series at the position ANT 5-2

Figure B.3: Potential temperature (top panel) and salinity (bottom panel) time series at the position ANT 7
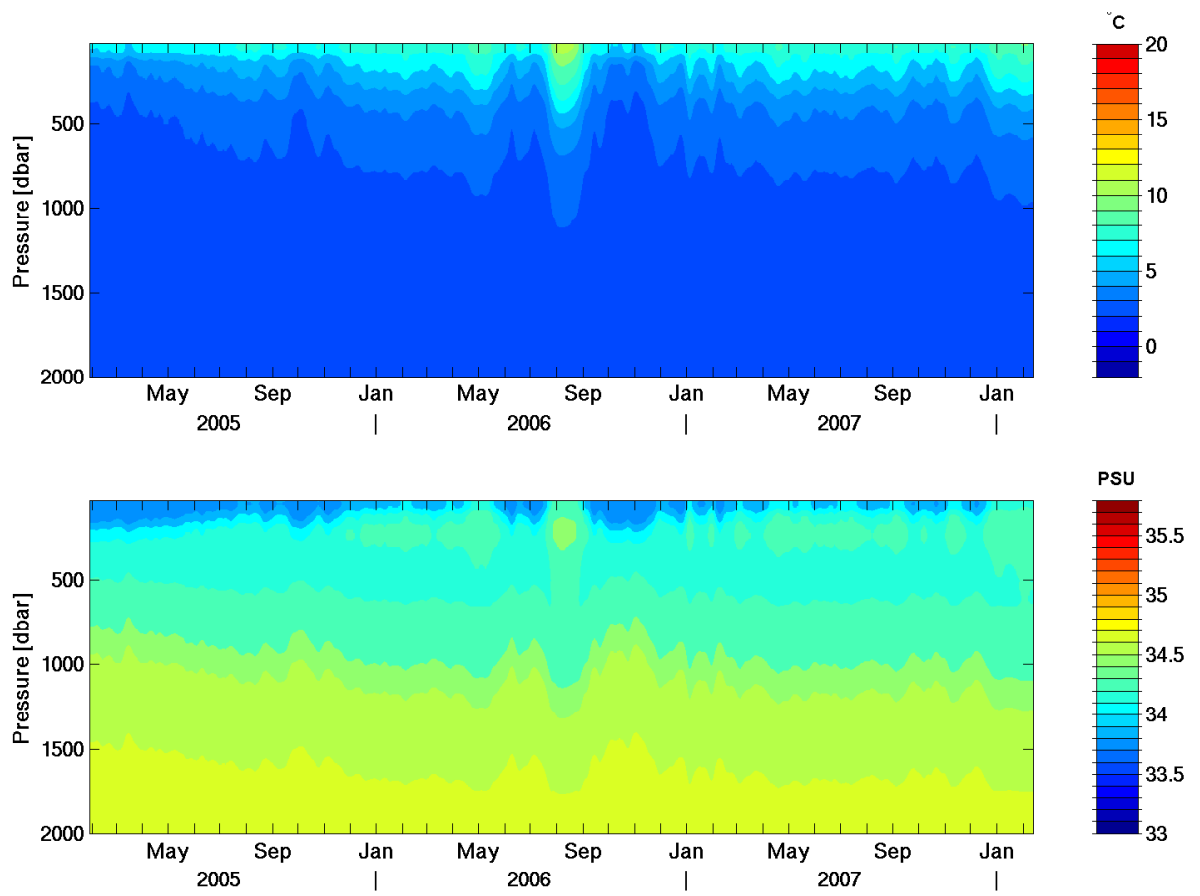
Figure B.4: Potential temperature (top panel) and salinity (bottom panel) time series at the position ANT 7
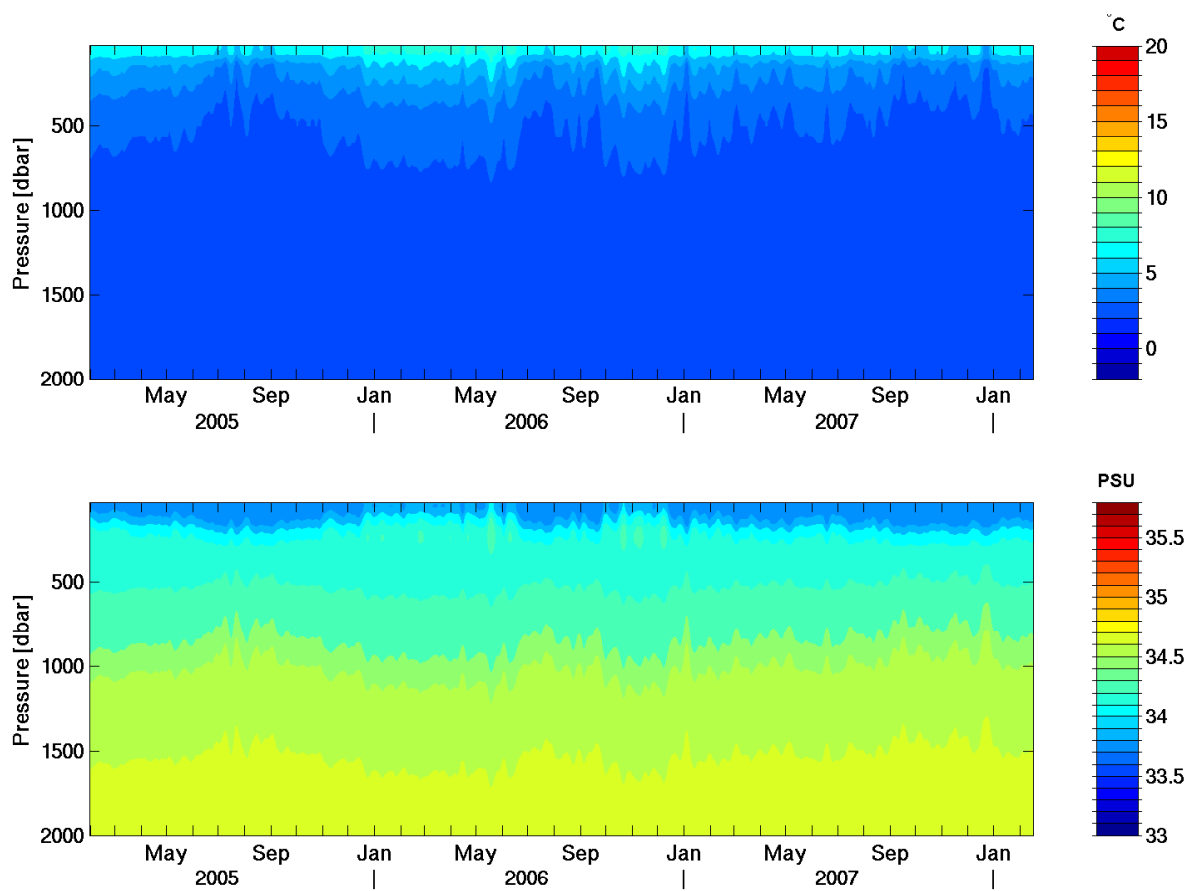
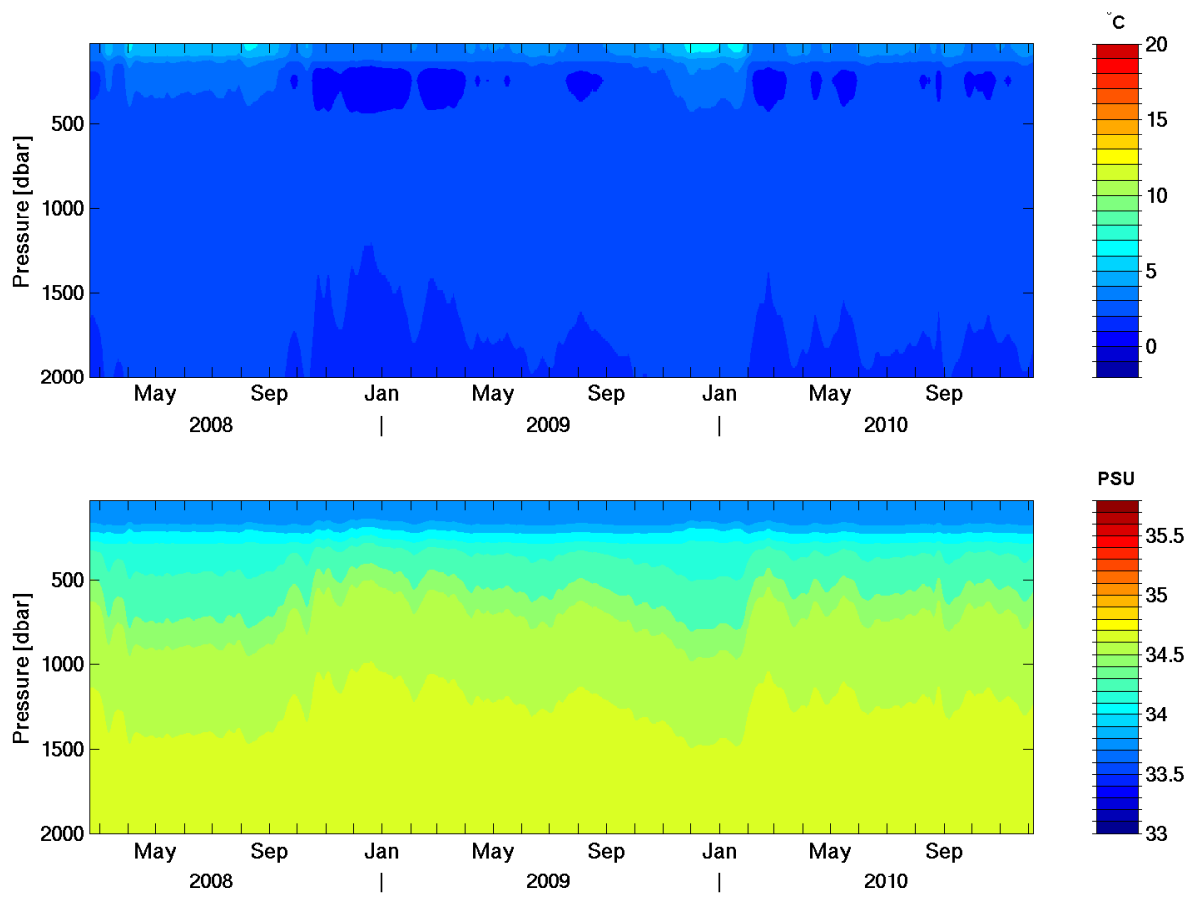Figure B.5: Potential temperature (top panel) and salinity (bottom panel) time series at the position ANT 9

Figure B.6: Potential temperature (top panel) and salinity (bottom panel) time series at the position ANT 11
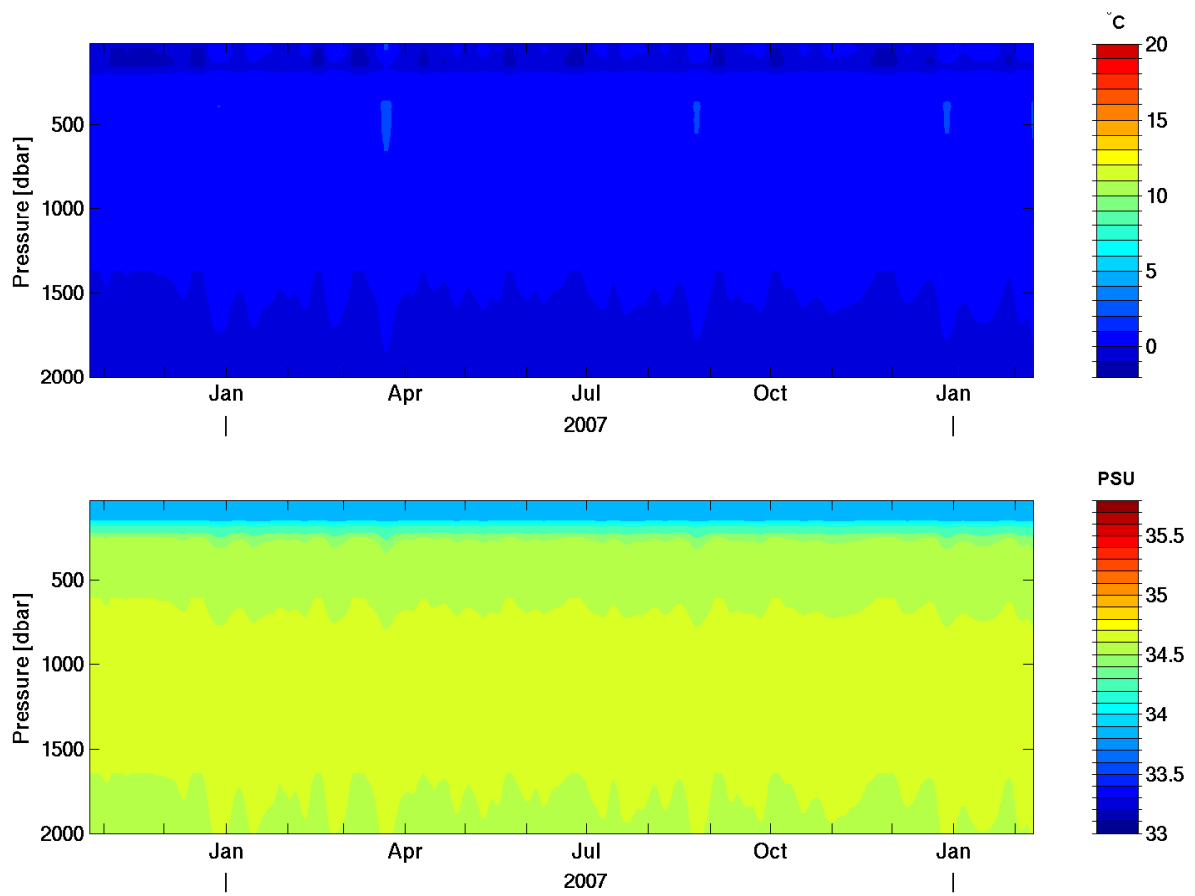
Figure B.7: Potential temperature (top panel) and salinity (bottom panel) time series at the position ANT 13
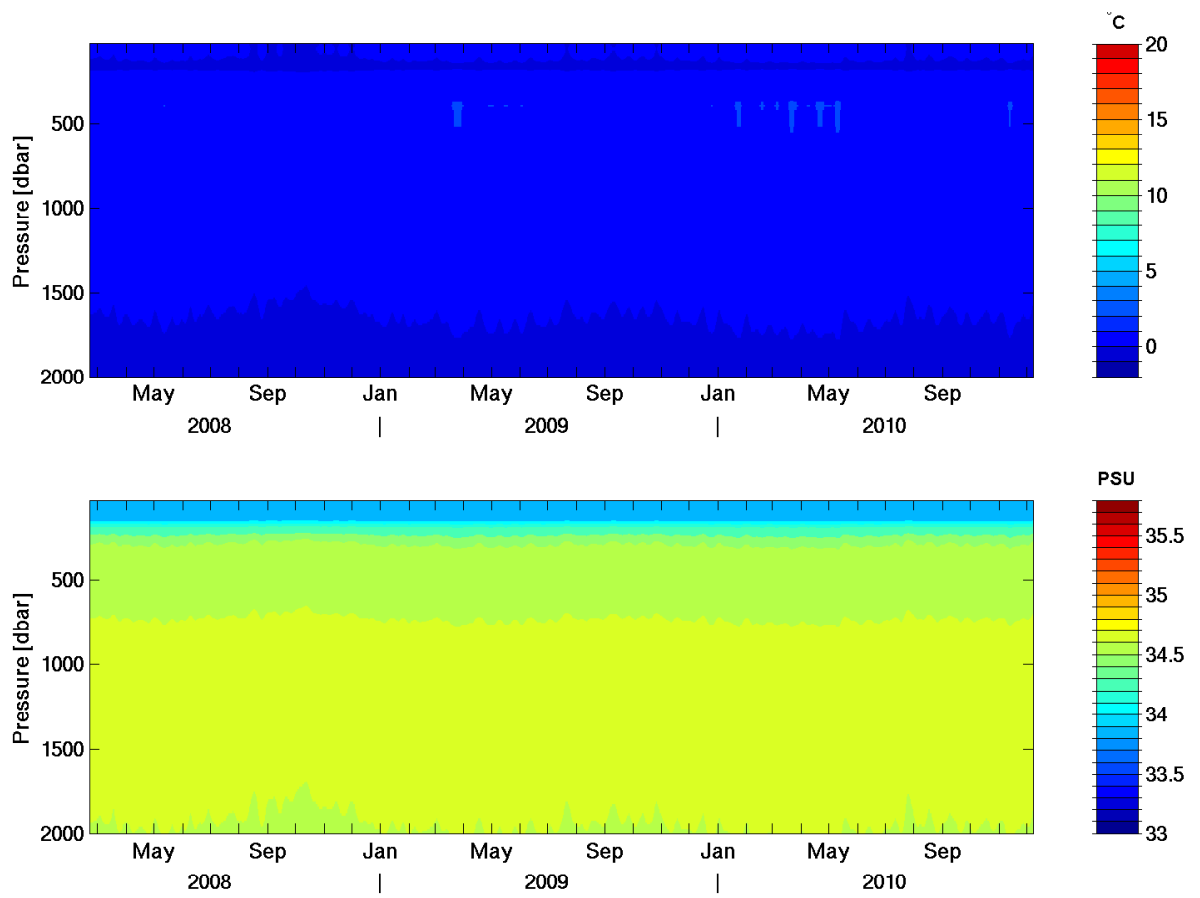
Figure B.8: Potential temperature (top panel) and salinity (bottom panel) time series at the position ANT 13-2

C Positions of the BPRs from the global database

BPR Nr.	BPR name	Latitude	Longitude
1	AWI_ANT11	-50.2502	1.4167
2	AWI_ANT13a	-52.507	-1.4007
3	AWI_ANT3	-37.0927	12.7693
4	AWI_ANT5	-41.134	9.9438
5	AWI_ANT537	-41.1828	4.2582
6	AWI_ANT7	-44.6625	7.0838
7	AWI_ANT9	-47.656	4.2617
8	APL_ABPR_1	89.2543	60.3597
9	APL_ABPR_3	89.2475	148.1257
10	AWI_F2	78.8338	8.3318
11	AWI_F4	78.8385	7.0048
12	AWI_F5	78.8337	5.9473
13	AWI_F6	78.8322	5.0145
14	AWI_F7	78.833	3.9457
15	AWI_F8	78.8312	2.7932
16	KESS_A2	37.81	147.87
17	KESS_B1	37.11	144.57
18	KESS_B2	37.1	145.51
19	KESS_B3	37.1	146.46
20	KESS_B4	37.1	147.4
21	KESS_B5	37.1	148.35
22	KESS_C1	36.35	144.09
23	KESS_C2	36.35	145.05
24	KESS_C3	36.35	145.99
25	KESS_C4	36.35	146.92
26	KESS_C5	36.35	147.89
27	KESS_C6	36.35	148.85
28	KESS_D1	35.43	143.52
29	KESS_D2	35.59	144.57
30	KESS_D3	35.59	145.53

31	KESS_D4	35.59	146.45
32	KESS_D5	35.59	147.4
33	KESS_D6	35.59	148.36
34	KESS_E1	34.83	143.16
35	KESS_E2	34.83	144.1
36	KESS_E3	34.83	145.04
37	KESS_E4	34.83	145.99
38	KESS_E5	34.82	146.93
39	KESS_E6	34.82	147.88
40	KESS_E7	34.83	148.82
41	KESS_F1	34.01	143.43
42	KESS_F2	33.92	144.62
43	KESS_F3	34.01	145.5
44	KESS_F4	34.01	146.47
45	KESS_F5	34.01	147.4
46	KESS_F6	33.85	148.24
47	KESS_G1	33.19	144.11
48	KESS_G2	33.19	145.03
49	KESS_G3	33.19	145.99
50	KESS_G4	33.19	146.94
51	KESS_G5	33.19	147.87
52	KESS_G6	33.19	148.79
53	KESS_H2	32.37	144.57
54	KESS_H3	32.37	145.51
55	KESS_H4	32.37	146.46
56	KESS_H5	32.37	147.4
57	KESS_H6	32.37	148.35
58	KESS_I1	31.49	144.09
59	KESS_N1	38.51	148.34
60	KESS_S1	30.02	143.31
61	KESS_S2	30.61	143.62
62	CNES_AMS	-37.9033	77.58
63	CNES_CRO	-46.5467	51.7883
64	MOVE_M2.5	16.1667	-58.7167

65	MOVE_M3	16.34	-60.505
66	MOVE_M1	15.4502	-51.5265
67	MOVE_M6	20.5918	-56.6797
68	MOVE_M2	15.9867	-56.95
69	DART_21413	30.55	152.118
70	DART_21414	48.938	178.281
71	DART_21415	50.183	171.849
72	DART_21416	48.044	163.488
73	DART_21418	38.711	148.694
74	DART_23401	8.905	88.54
75	DART_32411	4.923	-90.685
76	DART_32412	-17.975	-86.392
77	DART_41421	23.399	-63.901
78	DART_41424	32.928	-72.47
79	DART_42407	15.256	-68.246
80	DART_43412	16.034	-107.001
81	DART_44401	37.562	-50
82	DART_44402	39.487	-70.594
83	DART_46403	52.636	-156.932
84	DART_46404	45.859	-128.778
85	DART_46408	49.626	-169.871
86	DART_46411	39.331	-127.013
87	DART_46412	32.457	-120.561
88	DART_46419	48.762	-129.617
89	DART_51407	19.649	-156.516
90	DART_51425	-9.493	-176.245
91	DART_51426	-22.993	-168.098
92	DART_52401	19.286	155.766
93	DART_52402	11.883	154.116
94	DART_52403	4.033	145.597
95	DART_52404	20.949	132.223
96	DART_52405	12.881	132.333
97	DART_52406	-5.332	165.081
98	DART_53401	0.05	91.899

99	DART_55012	-15.8	158.5
100	DART_55015	-46.922	160.562
101	DART_46405	42.903	-130.909
102	DART_32401	-19.547	-74.813
103	DART_46402	51.069	-164.011
104	DART_54401	-33.005	-172.985
105	DART_d125	-8.4887	-125.014
106	DART_d157	52.5907	-157.164
107	DART_d171	42.6368	-170.7977
108	POL_IO1	-47.1167	54.9008
109	POL_IO2	-48.8317	61.2797
110	POL_ND2	-54.9432	-58.3568
111	POL_SD2	-60.8505	-54.7133
112	POL_GRACE-2	-44.42	-40.3698
113	POL_GRACE-3	-43.1983	-45.3017
114	POL_MYRTLE	-60.0497	-47.17
115	POL_SHAGEX1	-53.081	-47.102
116	POL_SHAGEX2	-53.3868	-49.5303
117	RAPID_MAR1	24.4913	-50.2603
118	RAPID_MAR2	24.476	-50.5703
119	RAPID_MAR3	24.4998	-41.2153
120	RAPID_MAR4	24.5018	-41.3012
121	RAPID_EB1	24.5238	-23.4488
122	RAPID_EB3	26.9962	-16.2307
123	RAPID_EBH1	27.276	-15.4167
124	RAPID_EBH2	27.488	-14.6847
125	RAPID_EBH3	27.6223	-14.2053
126	RAPID_EBH4	27.8322	-13.7887
127	RAPID_EBH5	27.8567	-13.5207

References

Arntz WE and Rohardt G: Continuous thermosalinograph oceanography along PO-LARSTERN cruise track ANT-XXI/2, Alfred Wegener Institute for Polar and Marine Research, Bremerhaven, doi:10.1594/PANGAEA.666228, 2007.

Baker-Yeboah S, Watts DR, and Deidre AB: Measurements of Sea Surface Height Variability in the Eastern South Atlantic from Pressure Sensor-Equipped Inverted Echo Sounders: Baroclinic and Barotropic Components. Journal of Atmospheric and Oceanic Technology, Vol. 26, pp. 2593–2609, 2009.

Böning C, Timmermann R, Macrander A, and Schröter J: A pattern-filtering method for the determination of ocean bottom pressure anomalies from GRACE solutions. Geophysical Research Letters, Vol. 35, doi:10.1029/2008GL034974, 2008a.

Böning CW, Dispert A, Visbeck M, Rintoul SR, and Schwarzkopf FU: The response of the Antarctic Circumpolar Current to recent climate change. Nature Geoscience, Vol. 1, doi:10.1038/ngeo362, 2008b.

Boebel O, Lutjeharms J, Schmid C, Zenk W, Rossby T, and Barron C: The Cape Cauldron: a regime of turbulent inter-ocean exchange. Deep Sea Research II, Vol. 50, pp. 57–86, 2003.

Book JW, Wimbush M, Imawaki S, Ichikawa H, Uchida H, and Kinoshita H: Kuroshio temporal and spatial variations south of Japan determined from inverted. Journal of Geophysical Research, Vol. 107(C9), doi:10.1029/2001JC000795, 2001.

Brunnabend S-E, Rietbroek R, Timmermann R, Schröter J, and Kusche J: Improving mass redistribution estimates by modeling ocean bottom pressure uncertainties. Journal of Geophysical Research, Vol. 116, 2011.

Byrne DA and McClean JL: Sea level anomaly signals in the Agulhas Current region. Geophysical Research Letters, Vol. 35, pp. L113 601, doi:10.1029/2008GL034087, 2008.

Carrère L and Lyard F: Modeling the barotropic response of the global ocean to atmospheric wind and pressure forcing - comparisons with observations. Geophysical Research Letters, Vol. 30(6), pp. 1275, doi:10.1029/2002GL016473, 2003.

Chambers D, Wahr J, and Nerem R: Preliminary observations of global ocean mass variations from GRACE. Geophysical Research Letters, Vol. 31 (13), 2004.

Chereskin T, Mazloff M, Millar J, and Firing Y: A Comparison of the Recent Observations in Drake Passage to the Southern Ocean Sate Estimate. Ocean Science Conference, Salt Lake City, http://www.cdrake.org/publications/os2012_tkc.pdf, 2012.

Cunningham SA, Alderson SG, and King BA: Transport and variability of the Antarctic Circumpolar Current in Drake Passage. Journal of Geophysical Research, Vol. 108, NO. C5, pp. 8084, doi:10.1029/2001JC001147, 2003.

Darbyshire M: The surface waters near the coast of South Africa. Deep Sea Research, Vol. 13, pp. 57–81, 1966.

Deacon GER: The hydrology of the Southern Ocean. Discovery Reports, Vol. 15, pp. 1–124, 1937.

Dhomps AL, Guinehut S, Traon PYL, and Larnicol G: A global comparison of Argo and satellite altimetry observations. Ocean Science, Vol. 7, pp. 175–183, 2011.

Dong S, Springtall J, and Gille ST: Location of the Antarctic Polar Front from AMSR-E Satellite Sea Surface Temperature Measurements. Journal of Physical Oceanography, Vol. 36, 2006.

Fahrbach E: Physical oceanography during POLARSTERN cruise ANT-XI/2, Alfred Wegener Institute for Polar and Marine Research, Bremerhaven, doi:10.1594/PANGAEA.735279, 2010.

Fahrbach E and Rohardt G: Continuous thermosalinograph oceanography along POLARSTERN cruise track ANT-XV/4, Alfred Wegener Institute for Polar and Marine Research, Bremerhaven, doi:10.1594/PANGAEA.666196, 2007a.

Fahrbach E and Rohardt G: Continuous thermosalinograph oceanography along POLARSTERN cruise track ANT-XVI/2, Alfred Wegener Institute for Polar and Marine Research, Bremerhaven, doi:10.1594/PANGAEA.666202, 2007b.

Ferry NE, Rémy E, Brasseur P, and Maes C: Mercator global ocean operational analysis system: Assessment and validation of an 11-year reanalysis. Journal of Marine System, Vol. 65, pp. 540–560, 2007.

Fofonoff P and Millard Jr. RC: Algorithms for computation of fundamental properties of seawater. Unesco Technical Paper in Marine Science, Vol. 44, 1983.

Fukumori I and Wunsch C: Efficient representation of the North Atlantic hydrographic and chemical distributions. Progress in Oceanography, Vol. 27, pp. 111–195, 1991.

Fütterer DK and Rohardt G: Continuous thermosalinograph oceanography along POLARSTERN cruise track ANT-XVIII/3, Alfred Wegener Institute for Polar and Marine Research, Bremerhaven, doi:10.1594/PANGAEA.666214, 2007.

Fütterer DK and Rohardt G: Continuous thermosalinograph oceanography along POLARSTERN cruise track ANT-XX/2, Alfred Wegener Institute for Polar and Marine Research, Bremerhaven, doi:10.1594/PANGAEA.666218, 2007a.

García MA, Bladé I, Cruzado A, Velásquez Z, García H, Puigdefábregas J, and Sospedra J: Observed variability of water properties and transports on the World Ocean Circulation Experiment SR1b section across the Antarctic Circumpolar Current. Journal of Geophysical Research, Vol. 107(C10), doi:10.1029/2000JC000277, 2002.

Gladyshev S, Arhan M, Sokov A, and Speich S: A hydrographic section from South Africa to the southern limit of the Antarctic Circumpolar Current at the Greenwich meridian. Deep-Sea Research I, Vol. 55, pp. 1284–1303, 2008.

Gong D and Wang S: Definition of Antarctic oscillation index. Geophysical Research Letters, Vol. 26 (4), 1999.

Grinsted A, Moore JC, and Jevrejeva S: Application of the cross wavelet transform and wavelet coherence to geophysical time series. Nonlinear Processes in Geophysics, Vol. 11, pp. 561–566, 2004.

Heiskanen WA and Moritz H: Physical Geodesy, W H Freeman, San Francisco, 1967.

Heywood K and King BA: Water masses and baroclinic transport in the South Atlantic and Southern oceans. Journal of Marine Research, Vol. 60, pp. 639–676, 2002.

Kennelly M, Tracey K, and Watts DR: Inverted Echo Sounder Data Processing Manual. GSO Techical Report, Vol. No.2007-02, www.po.gso.uri.edu/dynamics/publications/tech_rpts, 2007.

Klatt O, Fahrbach E, Hoppema M, and Rohardt G: The transport of the Weddell Gyre across the Prime Meridian. Deep-Sea Research II, Vol. 52, pp. 513–528, doi:10.1016/j.dsr2.2004.12.015, 2005.

Lutjeharms JRE: Location of the frontal syste between Africa and Antarctica: some preliminary results. Deep-Sea Research, Vol. 32 No 12, pp. 1499–1509, 1985.

Lynn RJ and Reid JL: Characteristics and circulation of deep and abyssal waters. Deep-Sea Research, Vol. 15, pp. 577–598, 1968.

Macrander A, Böning C, Boebel O, and Schröter J: Validation of GRACE Gravity Fields by In-Situ Data of Ocean Bottom Pressure. in: System Earth via Geodetic-Geophysical Space Techniques, edited by Flechtner FM, Gruber T, Güntner A, Mandea M, Rothacher M, Schöne T, Wickert J, Stroink L, Mosbrugger V, and Wefer G, Advanced Technologies in Earth Sciences, pp. 169–185, Springer Berlin Heidelberg, URL http://dx.doi.org/10.1007/978-3-642-10228-8_14, 2010.

Mazloff MR, Heimbach P, and Wunsch C: An Eddy-Permitting Southern Ocean State Estimate. Journal of Physical Oceanography, Vol. 40, pp. 880–898, 2010.

Meinen CS and Watts DR: Vertical structure and transport on a transect across the North Atlantic Current near 42°N: Time series and mean. Journal of Geophysical Research, Vol. 105, NO. C9, pp. 21.869–21.891, 2000.

Nan S and Li J: The relationship between the summer precipitation in the Yangtze River valley and the boreal spring Southern Hemisphere annular mode. Geophysical Research Letters, Vol. 30(24), doi:10.1029/2003GL018381, 2003.

Orsi AH, Nowlin Jr. WD, and Whitworth III T: On the circulation and stratification of the Weddell Gyre. Deep Sea Research, Vol. 40, pp. 169–203, 1993.

Orsi AH, Whitworth III T, and Nolin Jr. WD: On the meridional extend and fronts of the Antarctic Circumpolar Current. Deep-Sea Research I, Vol. 42, pp. 641–673, 1994.

Orsi AH, Whitworth III T, and Nowlin Jr. WD: On the meridional extent and fronts of the Antarctic Circumpolar Current. Deep Sea Research I, pp. 641–673, 1995.

Park YH, Gambéroni L, and Charriaud E: Frontal structure, water masses and circulation in the Crozet Basin. Journal of Geophysical Research, Vol. 98, pp. 12.361–12.385, 1993.

Park YH, Vivier F, Roquet F, and Kestenare E: Direct observations of the ACC transport across the Kerguelen Plateau. Geophysical Research Letters, Vol. 36, pp. L18 603, doi:10.1029/2009GL039617, 2009.

Peterson RG and Whitworth III T: The Subantarctic and Polar Fronts in Relation to Deep Water Masses Through the Southwestern Atlantic. Journal of Geophysical Research, Vol. 94 (C8), pp. 10.817–10.838, doi:10.1029/JC094iC08p10817, 1989.

Read JF and Pollard RT: Structure and Transport of the Antarctic Circumpolar Current and the Agulhas Return Current at 40°E. Journal of Geophysical Research, Vol. 98, NO. C7, pp. 12.281–12.295, 1993.

Reinsch CH: Smoothing by Spline Functions. Numerische Mathematik, Vol. 10, pp. 177–183, 1967.

Rietbroek R, Fritsche M, Brunnabend S-E, Daras I, Kusche J, Schröter J, Flechtner F, and Dietrich R: Global surface mass from a new combination of GRACE, modelled OBP and reprocessed GPS data. Journal of Geodynamics, Vol. 59-60, 2012.

Rintoul S and Sokolov S: Baroclinic transport variability of the Antarctic Circumpolar Current south of Australia (WOCE repeat section SR3). Journal of Geophysical Research, Vol. 106, NO. C2, pp. 2815–2832, 2001.

Rohardt G: Continuous thermosalinograph oceanography along POLARSTERN cruise track ANT-XXIII/7, Alfred Wegener Institute for Polar and Marine Research, Bremerhaven, doi:10.1594/PANGAEA.727458, 2009.

Rohardt G: Continuous thermosalinograph oceanography along POLARSTERN cruise track ANT-XXIV/3, Alfred Wegener Institute for Polar and Marine Research, Bremerhaven, doi:10.1594/PANGAEA.727465, 2009a.

Rossby T: On monitoring depth variations of the main thermocline acoustically. Journal of Geophysical Research, Vol. 74, pp. 5542–5546, 1969.

Savcenko R and Bosch W: EOT08a - Empirical ocean tide model from multi-mission satellite altimetry, Deutsches Geodätisches Forschungsinstitut, München, ftp.dgfi.badw.de/pub/EOT08a/doc/EOT08a.pdf, 2008.

Schwatke C, Bosch W, Savcenko R, and Dettmering D: OpenADB An open database for multi-mission altimetry, EGU Geophysical research abstract, 2010.

Sokolov S and Rintoul SR: Multiple Jets of the Antarctic Circumpolar Current South of Australia. Journal of Physical Oceanography, Vol. 37, pp. 1394–1412, 2006.

Spindler M and Rohardt G: Continuous thermosalinograph oceanography along POLARSTERN cruise track ANT-XXII/2, Alfred Wegener Institute for Polar and Marine Research, Bremerhaven, doi:10.1594/PANGAEA.666236, 2007.

Strammma L and Peterson RG: The South Atlantic Current. Journal of Physical Oceanography, Vol. 20, pp. 846–859, 1990.

Sverdrup UH, Johnson MW, and Flemming RH: The Oceans: Their Physics, Chemistry and General Biology, New York: Prentice-Hall, 1942.

Swart S, Speich S, Ansorg IJ, Goni GJ, Gladyshev S, and Lutjeharms JRE: Transport and variability of the Antarctic Circumpolar Current south of Africa. Journal of Geophysical Research, C09014, Vol. 113, doi:10.1029/2007JC004223, 2008.

Taylor KE: Summarizing multiple aspects of model performance in a single diagram. Journal of Geophysical Research, Vol. 106(D7), pp. 7183–7192, doi: 10.1029/2000JD900719, 2001.

Thompson DWJ and Wallace JM: Annular Mode in the Extratropical Circulation. Part I: Month-to-Month Variability. Journal of Climate, Vol. 13, 1999.

Thompson DWJ, Wallace JM, and Hegerl GC: Annular Mode in the Extratropical Circulation. Part II: Trends. Journal of Climate, Vol. 13, 1999a.

Timmermann R, Danilov S, Schröter J, Böning C, Sidorenko D, and Rollenhagen K: Ocean circulation and sea ice distribution in a finite element global sea ice-ocean model. Ocean Modelling, Vol. 27, no. 3-4, pp. 114–129, 2009.

Vinogradova NT, Ponte RM, and Stammer D: Relation between sea level and bottom pressure and the vertical dependence of oceanic variability. Geophysical Researche Letters, Vol. 34, pp. L03 608, doi:10.1029/2006GL028588, 2007.

Watts DR and Rossby T: Measuring Dynamic Heights with Inverted Echo Sounders: Results from MODE. Journal of Physical Oceanography, Vol. 7, pp. 345–358, 1977.

Watts DR, Quian X, and Tracey KL: Mapping Abyssal Current and Pressure Fields under the Meandering Gulf Stream. Journal of Atmospheric and Oceanic Technology, Vol. 18, pp. 1052–1067, 2000a.

Watts DR, Sun C, and Rintoul S: A Two-Dimensional Gravest Empirical Moder Determined from Hydrographic Observations in the Subantarctic Front. Journal of Physical Oceanography, Vol. 31, pp. 2186–2209, 2000b.

Whitworth III T and Nolin Jr. WD: Water masses and currents of the Southern Ocean at the Greenwich Meridian. Journal of Geophysical Research, Vol. 92, pp. 6462–6476, 1987.

Whitworth III T, Nolin Jr. WD, and Worley SJ: The Net Transport of the Antarctic Circumpolar Current through Drake Passage. Journal of Physical Oceanography, Vol. 12, pp. 960–971, 1982.

WOCE Hydrographic Programme: Physical oceanography during METEOR cruise M11/5 on section A12, Alfred Wegener Institute for Polar and Marine Research, Bremerhaven, doi:10.1594/PANGAEA.742625, 2002.

WOCE Hydrographic Programme: Physical oceanography during POLARSTERN cruise ANT-X/4 on section A12, Alfred Wegener Institute for Polar and Marine Research, Bremerhaven, doi:10.1594/PANGAEA.738488, 2002a.

Acknowledgment

Curriculum vitae

Personal Informations

name:	Madlen Gebler
address:	Richtweg 14
	28195 Bremen, Germany
e-mail:	madlen.gebler@loop.de
born at/in:	10.08.1985 Gera, Germany
nationality:	German

Education
Study

Sep. 2009 - Feb. 2013	Phd thesis, Alfred Wegener Institute
	section Climate Dynamic
	"Detection and analyisis of oceanic motion using
	Pressure Inverted Echo Sounder (PIES)"
Aug. 2009:	degree in physics ("Diplom Physiker")
	Diploma thesis, Department of Oceanography
	University of Bremen
	"Westward flow of Weddell Sea bottom water
	trough Drake Passage"
Oct. 2004 - Aug. 2009	University of Bremen
	Study of Physics

School

2000 - 2004	Carl-Zeiss-Gymnasium Jena
	special school for mathematic and natural sciences
	leaving certificate Abitur (final grade 1,6)

Expeditions

21.March-09.April 2009	FS Polarstern ANT XXV-4
	function: CFC and Helium sampling
	Department of Oceanography University of Bremen
22.Juli-18.August 2008	FS Maria S. Merian MSM09/1
	Tfunction: CTD-Watch
	Department of Oceanography University of Bremen
06.February-16.April 2008	FS Polarstern ANT XXIV-3
	function: CFC and Helium sampling
	Department of Oceanography University of Bremen
24.October-11.November 2007	RV Pelagia PE278
	function: CTD-Watch and CFC sampling
	Department of Oceanography University of Bremen
04.April-07.Mai 2007	FS Maria S. Merian MSM05/1
	function: CTD-Watch
	Department of Oceanography University of Bremen